MULTIMODAL QUANTUM SENSING WITH SOLID-STATE SPINS IN DIAMOND

A DISSERTATION SUBMITTED TO
THE DEPARTMENT OF PHYSICS
IN PARTIAL FULFILLMENT OF THE REQUIREMENTS
FOR THE DEGREE OF
DOCTOR OF PHILOSOPHY
IN PHYSICS

BY
XIN-YUE ZHANG

BOSTON COLLEGE
MORRISSEY COLLEGE OF ARTS AND SCIENCES
GRADUATE SCHOOL
CHESTNUT HILL, MASSACHUSETTS
APRIL 30, 2024

Copyright © 2024 by Xin-Yue Zhang

Abstract

Xin-Yue Zhang

Thesis Advisor: Brian B. Zhou

This thesis presents work in the context of multimodal magnetometry for two-dimensional (2d) materials. Research on van der Waals (vdW) materials has been rapidly emerging and several imaging techniques have been developed in the past decades. Among the modern techniques, solid-state spins feature outstanding sensitivity and nano-scale spatial resolution. Yet their full capacity in sensing still has room for improvement, as the quantum nature of their properties haven't been fully utilized. My research involves developing state-of-the-art sensing techniques to add new 'function modules' to the nitrogen-vacancy (NV) centers, with the goal of uncovering dynamical magnetic and electrical phenomena of 2d materials.

In the first chapter I will briefly discuss the basic opto-spin properties of the NV center. One shall see why NV is preferred as a quantum sensing probe: the opto-spin property comes handy as one simply counts photons to manipulate and read out quantum states, and the stability and long quantum coherence time makes NV adaptive with various environments and engineering. In the second chapter I will discuss the experimental setup with the focus on the home-built confocal microscope, which equips our sensing technique with the pump-probe scanning ability of sub-μm 2d resolution. In the third chapter I will discuss the developments of the sensing protocols, including the ac susceptometry and the opto-magnetization mapping, based on the lock-in method using the quantum dynamical decoupling (DD) sequences. In the fourth chapter I will describe the ac susceptibility measurements on thin $CrBr_3$ flakes. The magnetization behaviors under kHz to MHz excitations reveal the domain morphology and domain wall mobility, providing insights to the exchange interaction of the chromium trihalides in the 2d limit. In the fifth chapter I will describe the pump-probe measurements on few-layer $CrCl_3$ flakes. The mapping result demonstrates a photo-generated enhancement of the in-plane magnetization. Along with the time-resolved photoluminescence (PL) measurement, the results are indicative of a defect-assisted Auger recombination process of excitons.

To conclude, the multimodal sensing techniques with NV developed in this thesis allow for more versatile experiments with sensitivity for low-dimensional systems. The developments bring up new perspectives on fundamental physics in atomically thin materials, providing new ideas for future technological applications such as spintronics and quantum memory.

Table of Contents

List of Figures

List of Tables

Chapter 1
NV center

Solid-state spins have emerged as an attractive platform for nanoscale magnetic field sensing. With the intensive research in 2d vdW materials and biomacromolecules, solid-state spins stand out as a great probe for current and magnetism sensors or biolablers in these nanoscale materials, featuring the robustness to decoherence, inert hosts such as diamonds or silicon, and the ability to be isolated as single atomic-scale impurities. Among the different types of solid-state spins, the NV center is the most widely used for physical and biological sensing [1–3]. Because of its responsive photo-spin property, its stable coherence in a variety of environments such as in extreme temperatures [4], high pressure [5], and the customizable shape of its hosting diamond [6–8], the NV center achieves high proximity or integrates well with target materials, sensing with high signal-to-noise ratio (SNR).

In this chapter the basic physics of NV centers will be discussed. Firstly, the crystallographic and electronic structure will be explained. Secondly, the opto-spin properties and microwave driving will be introduced along with the ground-state Hamiltonian. The basic static magnetic field sensing technique, optically detected magnetic resonance (ODMR), can thus be understood. Thirdly, a full description of the NV center energy levels is introduced, explaining the origin of the opto-spin properties. Fourthly, the decoherence sources and different lifetimes will be discussed along with the DD protocols.

1.1 structure

1.1.1 crystallography

The NV center in diamond comprises a substitutional nitrogen atom and a missing carbon atom. The NV center axis is defined as the direction connecting the nitrogen and the vacancy. Each atom in the diamond has four nearest neighbors, so NV centers have four possible directions and the point group symmetry is C_{3V}.

1.1.2 charged states

The NV centers have three possible charged states: negatively charged, neutral or positively charged. Of the three charged states, only NV^- shows spin-selective photon emission and is thermodynamically favoured in bulk diamond, therefore NV^- is preferred for sensing or quantum info application. However the other charged states could form depending on the

local environment. Especially the neutrally charged state brings up challenges, as it tends to form with very shallow depth (< 10 nm) [9, 10] or under resonant excitation [11]. One has to balance coherence and sensitivity when choosing nitrogen ion implantation energy, which determines the NV depth; and avoid photo illumination of certain wavelength to reduce the unwanted switching between NV^- and NV^0, which impedes quantum efficiency.

1.2 spin-photo properties and ODMR

1.2.1 ground state triplet

The ground state is a spin triplet system. At zero magnetic field, the $|m_s = \pm 1\rangle$ states are degenerate and are separated from $|m_s = 0\rangle$ by $D = 2.88$ GHz. There is also an excited state triplet that is doubly degenerate (a total of six sublevels), with a zero-field splitting of $D_e = 1.42$ GHz. The precise values of D and D_e are temperature dependent. [12]

At non-zero magnetic field, the Zeeman splitting lifts the degeneracy of $|m_s = \pm 1\rangle$ states. When the field is aligned along the NV center axis, which is typically the case for most experiments, the splitting between the two states is simply linear, with a coefficient of $2\gamma_e = 0.56$ MHz/mT. When the field is not aligned with the NV center, the spin polarization is no longer a good quantum number, as $|m_s = 0, \pm 1\rangle$ are not eigenstates anymore. The energy is then calculated by solving the eigenvalues of the 3-by-3 matrix. In an ensemble NV sample, there are four possible NV orientations equally distributed over the substrate, of which one is usually aligned with external field and three are degenerately misaligned, as shown in Fig 1.2.2 (f).

A slightly misaligned magnetic field usually does not hurt dc sensing with ODMR as long as the perpendicular component is small and m_s is still a good quantum number. However when ac sensing with DD sequences, the arising of a misaligned dc field could tilt the axis of ac field projection, thus introducing bias. This is discussed in detail in Ch 3.2.5.

The ground state Hamiltonian with magnetic field is:

$$H_{\mathrm{GS}} = hDS_z^2 + g\mu_B \mathbf{B}\cdot\hat{\mathbf{S}} = \begin{pmatrix} hD + g\mu_B B_z & \frac{g\mu_B}{\sqrt{2}}(B_x - iB_y) & 0 \\ \frac{g\mu_B}{\sqrt{2}}(B_x + iB_y) & 0 & \frac{g\mu_B}{\sqrt{2}}(B_x - iB_y) \\ 0 & \frac{g\mu_B}{\sqrt{2}}(B_x + iB_y) & hD - g\mu_B B_z \end{pmatrix} \quad (1.1)$$

The NV center could also experience strain, which exists non-uniformly in the lattice, or an external electric field. For simplicity, we just need to consider the Hamiltonian at zero

magnetic field and omit the axial component of the electric dipole moment, which is much smaller than the non-axial component, d. The simplified Hamiltonian is:

$$H_{\mathrm{GS}} = hDS_z^2 + dE(S_x^2 - S_y^2) = \begin{pmatrix} hD & & dE \\ 0 & 0 & 0 \\ dE & 0 & hD \end{pmatrix} \tag{1.2}$$

The eigenvalues change from (0, hD, hD) to (0, hD-dE, hD+dE). The electric field breaks the degeneracy of $|m_s = \pm 1\rangle$ and opens a small gap at zero field. This is termed the Stark effect and is used to sense electrical field [13, 14].

1.2.2 optically detected spin polarization

The PL intensity of NV is spin dependent, about 30% fewer photons for $|m_s = \pm 1\rangle$ compared to $|m_s = 0\rangle$. This discrimination comes from the intersystem crossing (ISC) that couples the triplets and the singlets, which is explained in detail in Ch 1.3.3. This opto-spin property makes quantum sensing convenient with the NV center: one simply needs to count photons to figure out the qubit state. For example: One prepares the qubit state $|\alpha\rangle$ with a single NV center one million times. Each time after preparation, one shines a green photon onto the qubit and collects the red emitted photon. The number of the collected photons is either 0 or 1 each time, so the total number of collected photons is between zero and one million. If one prepares $|\alpha\rangle = |m_s = 0\rangle$, the total number of collected photons could be 10k; if one prepares $|\alpha\rangle = |m_s = -1\rangle$, the total number of collected photons could be 7k; if one prepares the superposition state $|\alpha\rangle = \cos\theta|m_s = 0\rangle + e^{i\phi}\sin\theta|m_s = -1\rangle$, the total number of collected photons is then 3k$\cdot\cos\theta$+7k. These numbers reflect the collection efficiency and contrast typically achieved with our confocal setup on deep single NVs in bulk diamonds. The photon collection efficiency is crucial for SNR and can be improved with better optical alignment and micro-structure engineering [16].

Most of the quantum sensing techniques with NV centers are about devising sequences to encode information into the quantum superposition phase θ and readout with brightness. For example magnetic field can be encoded into the azimuth phase through free Larmor precessions modulated with microwave or laser pulses.

1.2.3 Rabi, π and $\frac{\pi}{2}$ pulses

One uses NV brightness to readout the qubit state. The next question is how to prepare the qubit state with the desired superposition. One of the commons ways is to use microwave to

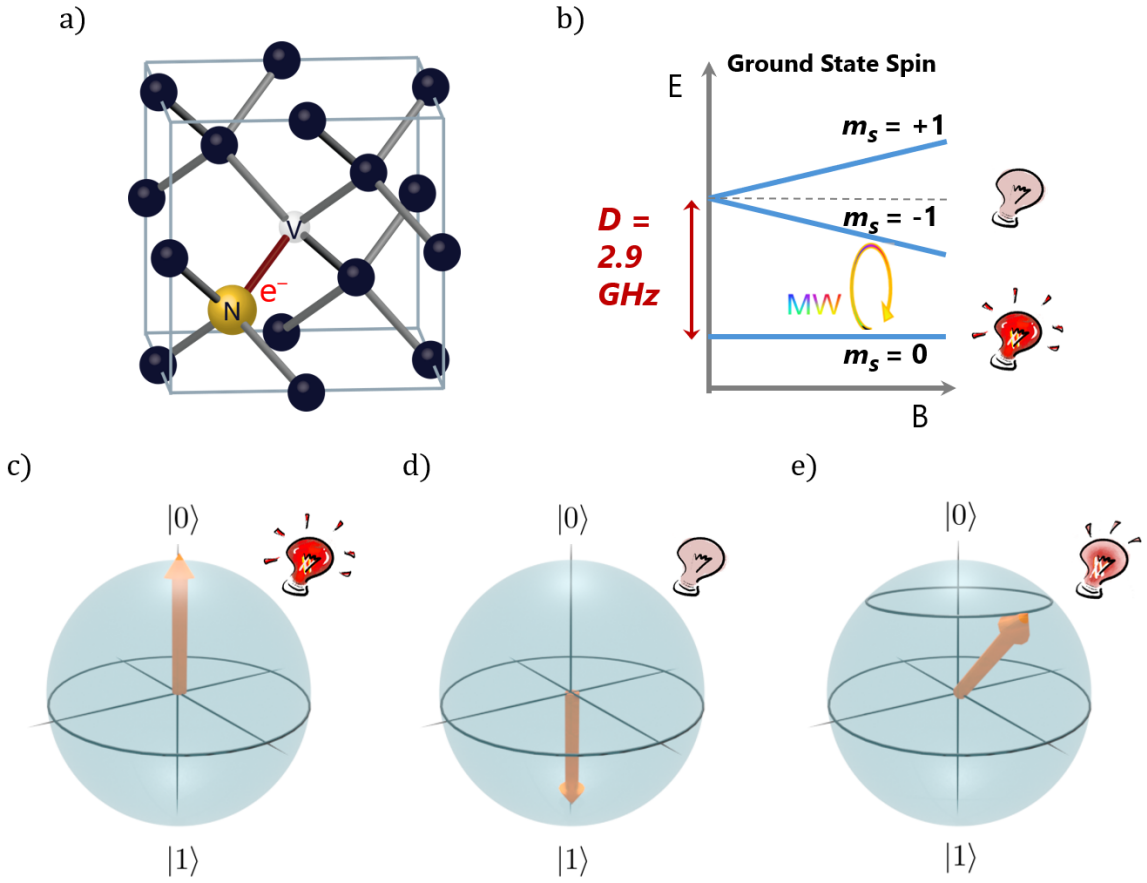

Figure 1.2.1: (a) Atomic structure of the NV^-. Figure adapted from Ref [15]. (b) Ground state triplet energy levels as a function of the parallel magnetic field. The transition between levels can be driven with resonant microwave. (c-e) Brightness of NV. $|0\rangle$ means $|m_s = 0\rangle$, $|1\rangle$ means $|m_s = -1\rangle$ or $|m_s = +1\rangle$. When the NV is in a superposition state, the collected photon number is larger than that when it is in $|1\rangle$ state, smaller than that when it is in $|0\rangle$ state. By normalizing the brightness, the superposition phase can be calculated.

drive the so-called Rabi oscillation, described by the rotating-wave approximation (RWA). The magnetic field with microwave driving is [17]:

$$\vec{B}(t) = B_0\hat{z} + 2B_1\cos(wt)\hat{x} = B_0\hat{z} + B_1\left[(\cos(wt)\hat{x} + \sin(wt)\hat{y}) + (\cos(wt)\hat{x} - \sin(wt)\hat{y})\right] \tag{1.3}$$

where B_1 and w describes the amplitude and frequency of the microwave; B_0 describes the energy splitting of the qubit, for example if one chooses to use $|m_s = 0\rangle$ and $|m_s = -1\rangle$ of NV, then $g\mu_B B_0 = hD - g\mu_B B_z$. Eq 1.3 includes only the perpendicular component of the magnetic field generated by the microwave because the parallel component averages out when applying RWA. The Hamiltonian in the lab frame is:

$$H = \frac{w_0}{2}\sigma_z + \frac{w_1}{2}\left[\cos(wt)\sigma_x + \sin(wt)\sigma_y\right] + \left[\cos(wt)\sigma_x - \sin(wt)\sigma_y\right] \tag{1.4}$$

where $w_0 = \gamma B_0, w_1 = \gamma B_1$. Rewriting the magnetic field term helps to transform the Hamiltonian using the interaction picture. The rotating frame is defined to be in pace with the microwave, i.e. $U_0 = e^{-iw\sigma_z/2}$. The second term of H transforms as $U_0^\dagger\left[\cos(wt)\sigma_x + \sin(wt)\sigma_y\right]U_0 = \sigma_x$, becoming static in the rotating frame. The third term $U_0^\dagger\left[\cos(wt)\sigma_x - \sin(wt)\sigma_y\right]U_0 = \cos(2wt)\sigma_x - \sin(2wt)\sigma_y$ is still an ac term in the rotating frame. The effect of the third term is to add a small and fast perturbation to the main trajectory of qubit evolution, as shown in the animation of Ref [18]. Usually $w \sim 3$ GHz, making the period of the small perturbation sub-nanosecond. Therefore the third term is not relevant in experiment and is discarded in the following discussion. The Hamiltonian in the interacting picture is:

$$H_I = \frac{w_0 - w}{2}\sigma_z + \frac{w_1}{2}\sigma_x = \frac{1}{2}\begin{pmatrix}\Delta w & w_1\\ w_1 & -\Delta w\end{pmatrix} \tag{1.5}$$

The Hamiltonian describes a rotation around an axis in the x-z plane with a polar angle of $\arctan(w_1/\Delta w)$. If the microwave is resonant, i.e. when the frequency of the microwave matches the energy level difference, then $\Delta w = 0$, meaning the rotation is around the x-axis. The evolution of an initialized state $|m_s = 0\rangle$ is then:

$$|\phi(t)\rangle = \cos\left(\frac{w_1 t}{2}\right)|m_s = 0\rangle - i\sin\left(\frac{w_1 t}{2}\right)|m_s = -1\rangle \tag{1.6}$$

The trajectory on Bloch sphere is shown in Fig 1.2.2(a). One can prepare a desired superposition state by controlling the amplitude w_1 and duration t of the microwave pulse.

For example:

$$\begin{aligned} t_1 &= \frac{\pi}{2w_1}, \quad |\phi(t_1)\rangle = \frac{1}{\sqrt{2}}\left(|m_s=0\rangle - i|m_s=-1\rangle\right) \\ t_2 &= \frac{\pi}{w_1}, \quad |\phi(t_2)\rangle = -i|m_s=-1\rangle \end{aligned} \tag{1.7}$$

The microwave pulse of duration t_1 and t_2 is called $\frac{\pi}{2}$ and π pulse respectively.

If the microwave is off-resonant, the evolution of the initialized state $|m_s=0\rangle$ is:

$$\begin{aligned} |\phi(t)\rangle = &\left[\cos\left(\frac{\sqrt{w_1^2+\Delta w^2}\ t}{2}\right) - i\frac{w_1}{\sqrt{w_1^2+\Delta w^2}}\sin\left(\frac{\sqrt{w_1^2+\Delta w^2}\ t}{2}\right)\right]|m_s=0\rangle \\ &- i\frac{w_1}{\sqrt{w_1^2+\Delta w^2}}\sin\left(\frac{\sqrt{w_1^2+\Delta w^2}\ t}{2}\right)|m_s=-1\rangle \end{aligned} \tag{1.8}$$

the rotation axis is tilted away from the x-axis towards the z-axis, and the amplitude and period of the qubit trajectory will be different, as shown in Fig 1.2.2(b). If the microwave frequency is far from resonant, the rotation axis will be the z-axis, and the qubit will not have a time evolution.

1.2.4 ODMR

The resonant microwave drives qubit to flip between bright ($|m_s=0\rangle$) and dark ($|m_s=\pm1\rangle$) states. We can use this property to measure the magnetic field, given that the energy splitting between bright and dark levels is dependent on the magnetic field. During ODMR measurement, the frequency of the microwave field is slowly swept and the photon emission rate is recorded. When the frequency matches the difference between energy levels, the NV center that was previously initialized in $|m_s=0\rangle$ with optical pumping can then be resonantly driven into $|m_s=\pm1\rangle$, resulting in a reduction of PL intensity. There are two dips in the recorded PL rate, the frequencies of which correspond to the energy of transitions from $|m_s=0\rangle$ to $|m_s=\pm1\rangle$ when the field is aligned. The ODMR result is also called electron paramagnetic resosnance (EPR) or electron spin resonance (ESR) spectrum. The microwave can be either constant or pulsed, pulsed ODMR usually has narrower dips in EPR spectrum and has higher precision on the measured magnetic field.

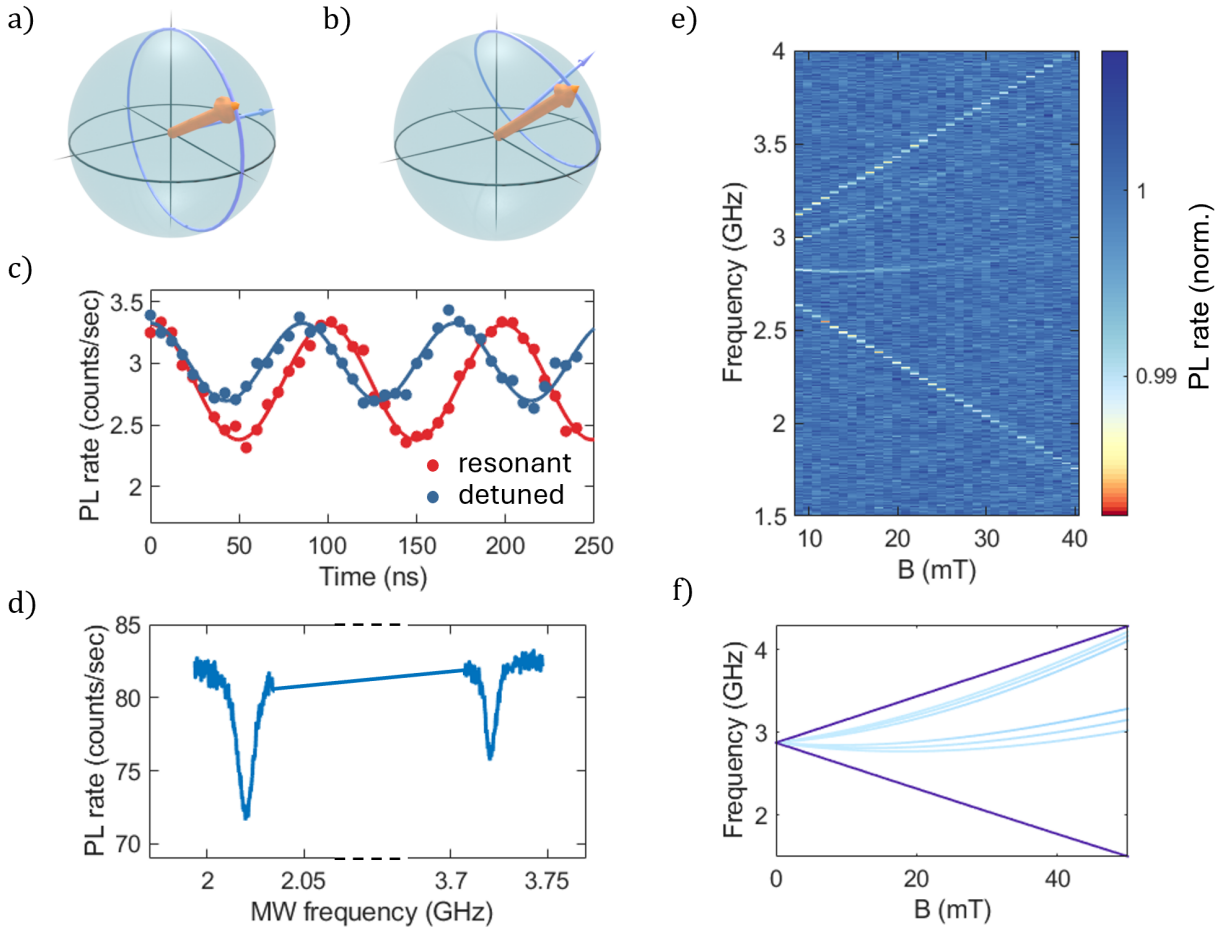

Figure 1.2.2: (a) Rabi trajectory with resonant microwave. (b) Rabi trajectory with detuned microwave. (c) Rabi measurement on a single NV center. Resonant microwave gives largest contrast because it drives full cycles between $|m_s = 0\rangle$ and $|m_s = -1\rangle$. Unresonant microwave gives lower contrast and faster frequency. This data set is taken at 50 mT, the resonant microwave is 1.5064 GHz, the unresonant microwave is 7.65 MHz detuned. (d) ODMR at 30 mT on ensemble NV centers. The lower frequency dip corresponds to $|m_s = 0\rangle \rightarrow |m_s = -1\rangle$, the higher frequency dip corresponds to $|m_s = 0\rangle \rightarrow |m_s = +1\rangle$. (e) ODMR spectrum as a function of magnetic field on ensemble NV centers. The PL rate is normalized by the highest brightness. The magnetic field is aligned with one of the four possible NV axis. The microwave also drives the NVs along the other three directions other than the one aligned with the magnetic field, demonstrated as the two middle obscure transitions. (f) Simulation of transition frequencies using Eq 1.1. The magnetic field direction is slightly tweeked, deviating from the perfect alignment, to show the three-fold degeneracy of the middle transitions.

1.3 electronic structure

In this section, the symmetric representation of states is introduced. Then the electronic states of the NV center in a single-particle picture are discussed. Based on the different occupations of the electronic states, the many-body states are constructed.

1.3.1 symmetry representations

The lowercase letters, such as a and e, represent the electronic states. These states are discussed in the single-particle picture, where each of the binding electrons is filled to the electronic states one by one, subject to Hund's rule. They are orthonormal and derived considering the binding and hybridization of orbitals from different atoms around the NV site. The uppercase letters, such as A and E, represent many-body states. With NV^-, the symmetry of a many-body state is determined by considering the wavefunctions of all the four in-gap electrons together.

The Mulliken symbols are used to describe the symmetry properties of the molecules. The letters represent a class of wavefunctions with certain behavior under different symmetry operations, the definitions of which can be referred to the character table. To use Mulliken symbols one has to first specify a point group. For example, some literature describe a as 'fully symmetric' states. One should not mistake it for a spherically symmetric state like an s orbital. The 'fullness' of a is specified by the point group: if one is talking about point group C_{2v}, then a is a two-fold symmetric electronic state, b is a two-fold antisymmetric electronic state; if one is talking about point group C_{5v}, then a is a five-fold symmetric electronic state. The same goes for the many-body state A.

For the NV center the point group is C_{3v}. This is obvious when one looks along the [1,1,1] axis: each of the three nearest carbon atoms contributes an sp^3 dangling bond $\sigma_{1,2,3}$ and the nitrogen atom contributes one dangling bond σ_4. Here we follow the convention in chemistry, where one uses σ to represent hybridized bonds and uses π to represent unhybridized bonds.

Therefore in NV centers, the electronic state a_1 means three-fold symmetric and e means doubly degenerate (e_x and e_y). For the many-body states, A_2 means three-fold rotational symmetric about z-axis ([1, 1, 1] axis) and antisymmetric about x- or y-axis flipping, A_1 means three-fold rotationally symmetric about the z-axis and symmetric about x- or y-axis flipping, E means doubly degenerate. The sublevels of E could have symmetries and be represented by A_1 or A_2 *etc.*

The superscript on the upper left corner for many-body states is indicative of the number of spin projection, i.e. ${}^3A_2$ is a triplet and ${}^1A_1$ is a singlet. In the following discussion,

the number in the parentheses, if any, for the single-particle states is just the index of different states with the same symmetry, i.e. $a_1(1)$ and $a_1(2)$ are two different fully symmetric electronic states. The different many-body states are not indexed and referred to in context.

1.3.2 electronic states in single-particle picture

The orthonormal states formed by the four dangling bonds are [19]:

$$\begin{aligned} a_1(1) :&\sqrt{1-\alpha^2}\sigma_4 - \frac{\alpha}{\sqrt{3}}(\sigma_1+\sigma_2+\sigma_3) \\ a_1(2) :&\alpha\sigma_4 + \sqrt{\frac{1-\alpha^2}{3}}(\sigma_1+\sigma_2+\sigma_3) \\ e_x :&\frac{1}{\sqrt{6}}(2\sigma_1-\sigma_2-\sigma_3) \\ e_y :&\frac{1}{\sqrt{2}}(\sigma_2-\sigma_3) \end{aligned} \tag{1.9}$$

where $\sigma_{1,2,3}$ are from the carbon and σ_4 is from the nitrogen. One can see a_1 states are clearly three-fold symmetric as contributed equally from the three carbon atoms. It is also interesting to note that e states have completely no contribution from the nitrogen. The $ab-intio$ calculation shows $\alpha \approx 0.7$, meaning that the nitrogen bond is mostly in $a_1(2)$.

Each of the four states can hold one spin up and one spin down electron. The spin-up and spin-down electrons have slightly different energies on the same states and are drawn separately on two sides in Fig 1.3.1 (a). The NV^- has six electrons. One can see that the $a_1(1)$ state is buried in the valence band, therefore it is always fully occupied with two electrons and does not contribute to the NV center properties.

1.3.3 many-body states and the optical transitions

The four in-gap electrons are filled to the in-gap states $a_1(2)$ and e, so there are three possible occupations: $a_1^2e^2$, $a_1^1e^3$ and $a_1^0e^4$. Each possible occupation could form several many-body states. For example, the occupation with the lowest energy is $a_1^2e^2$. Under this occupation, two out of four e levels are chosen to be filled, so the number of many-body states should be $C_4^2 = \frac{4!}{2!2!} = 6$. In fact, three of the six orthogonal many-body states of $a_1^2e^2$ occupation form the previously mentioned triplet ground state $^3A_2$. The other possible configurations are also listed in the table. One can also see why the optical excitation can only induce transitions from $^3A_2$ to ^3E (marked in blue and red), as the selection rule restricts spin projection M_S to be conserved.

Configuration	Γ	M_S	Wavefunction
$a_1^2e^2$	$^3A_2$	**1**	$\|a_1\bar{a_1}e_xe_y\rangle$
		0	$\|a_1\bar{a_1}\rangle \otimes \frac{1}{\sqrt{2}}\left[\|e_x\bar{e_y}\rangle + \|\bar{e_x}e_y\rangle\right]$
		-1	$\|a_1\bar{a_1}\bar{e_x}\bar{e_y}\rangle$
	$^1A_1$	0	$\|a_1\bar{a_1}\rangle \otimes \frac{1}{\sqrt{2}}\left[\|e_x\bar{e_x}\rangle + \|\bar{e_y}e_y\rangle\right]$
	^1E	0	$\|a_1\bar{a_1}\rangle \otimes \frac{1}{\sqrt{2}}\left[\|e_x\bar{e_x}\rangle - \|\bar{e_y}e_y\rangle\right]$
			$\|a_1\bar{a_1}\rangle \otimes \frac{1}{\sqrt{2}}\left[\|e_x\bar{e_y}\rangle - \|\bar{e_x}e_y\rangle\right]$
$a_1^1e^3$	^3E	**1**	$\|a_1e_xe_y\bar{e_y}\rangle$
			$\|a_1e_x\bar{e_x}e_y\rangle$
		0	$\|e_y\bar{e_y}\rangle \otimes \frac{1}{\sqrt{2}}\left[\|a_1e_x\rangle + \|a_1e_x\rangle\right]$
			$\|e_x\bar{e_x}\rangle \otimes \frac{1}{\sqrt{2}}\left[\|a_1e_y\rangle + \|a_1e_y\rangle\right]$
		-1	$\|\bar{a_1}\bar{e_x}e_y\bar{e_y}\rangle$
			$\|\bar{a_1}e_x\bar{e_x}\bar{e_y}\rangle$
	^1E	0	$\|e_y\bar{e_y}\rangle \otimes \frac{1}{\sqrt{2}}\left[\|a_1\bar{e_x}\rangle - \|\bar{a_1}e_x\rangle\right]$
			$\|e_x\bar{e_x}\rangle \otimes \frac{1}{\sqrt{2}}\left[\|a_1\bar{e_y}\rangle - \|\bar{a_1}e_y\rangle\right]$
$a_1^0e^4$	$^1A_1$	0	$\|e_x\bar{e_x}e_y\bar{e_y}\rangle$

Table 1.1: All the possible many-body states with NV^-. The colored text indicates possible optical transitions. Table adapted from Ref [19].

The sequential order of the energies of the many-body states is shown in Fig 1.3.1 (b). The ${}^1E$ state of $a_1^1e^3$ and the A_1 state of $a_1^0e^4$ are omitted because their energies are too high and not relevant to most quantum sensing experiments. The ground state triplet can be excited to the doubly degenerate triplet with optical excitations. The optical excitation used in experiments has higher energy than the zero phonon line (ZPL) because of the existence of wide phonon sideband (PSB). The ISC is realized through the ${}^1E$ state of $a_1^{2e^2}$ and the A_1 state of $a_{1e^3}^1$.

1.3.4 isc and psb

As shown in Fig 1.3.1 (b), once at the excited triplets there are two possible transitions. One is the radiative transition where a photon is emitted, with a lifetime $1/\gamma^r = 13$ ns; the other one is buffered by the singlet levels and the lifetime is $1/\gamma_{m_s}^{\text{isc}}$. The radiative transition is spin preserving, *i.e.* $\Delta m_s = 0$; while the ISC transition is spin selective, quantitatively $\gamma_{\pm1}^{\text{isc}} = 10\gamma_0^{\text{isc}}$, and $1/\gamma_0^{\text{isc}} = 250$ ns [21]. Therefore the total decay rate $\gamma_{m_s} = a^r\gamma^r + a^{\text{isc}}\gamma_{m_s}^{\text{isc}}$ is faster for $|m_s = \pm1\rangle$, where $a^r + a^{\text{isc}} = 1$ and a^r is 70-80%. Moreover, with continuous pumping the NV center will eventually end up with $|m_s = 0\rangle$, typically within several μs.

The ZPL is 637 nm and can be efficiently excited with shorter wavelength, typically green laser (515 nm or 532 nm). The emitted photoluminescence (PL) of 630-800 nm is accompanied by phonon emission, of which only 4% are coherently emitted into ZPL even at 6K. This wide PSB is advantageous for sensing, allowing for detection of an individual NV with optical confocal microscopy, but makes it more demanding in engineering for entanglement experiments where scattering losses have to be minimized.

At low temperature, a different photophysics is sometimes used with single NV centers for higher signal-to-noise ratio (SNR). Below 20K the fine structures of the orbital-doublet excited triplet are not obscured by phonons anymore. Therefore, the individual ZPL transitions can be resonantly addressed with a red laser with a fine-tuned variable wavelength. This spin-selective and spin-preserving pumping is protected from ISC and provides exceptional fidelity. However in this work we mostly use ensemble NV centers in bulk diamond for sensing, where the local strain varies location by location and the fine structure cannot be resolved.

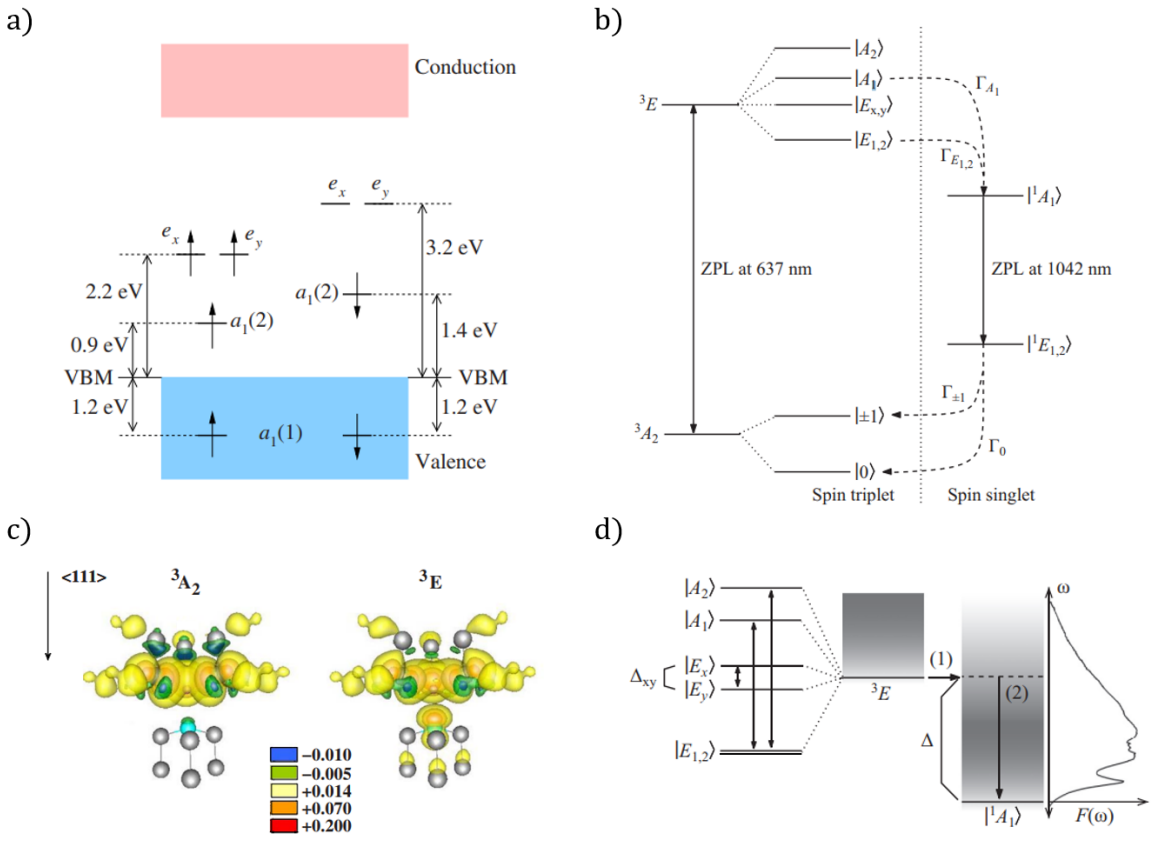

Figure 1.3.1: (a) The calculated spin-resolved single-electron levels with respect to the valence band maximum. The four levels are formed by the four bonds, one from each nearest neighbor atom. Each level hosts one spin up (plotted on left) and one spin down (plotted on right) electron. (b) The many-body levels that involve the photophysics. The collected photon is in the infrared spectrum. The state-selective nonradiative ISCs between the spin-triplet and spin-singlet levels (dashed arrows) arise from the different Γ values. (c) The calculated spin density isosurfaces in $m_s = 1$ state for the ground state triplet and the excited state doubly-degenerate triplet. The nitrogen atom is colored light blue, the carbon atoms are colored grey, and the vacant site is represented by the tiny pink sphere in the center. The isosurface plot reveals the nitrogen atom is more polarized in the excited state than the ground state. (d) The shaded region denotes phonon broadening. Left: detailed look at the excited state double-degenerate triplet. Δ_{xy} represents the strain-induced splitting. Right: $F(w)$ visualizes how $^3E - ^1A_1$ energy separation influences ISC rate. Figures adapted from Refs [19, 20].

1.4 relaxations

One of the advantages of NV center in quantum sensing is its remarkable coherence time, especially of those deep in bulk diamonds. The long lifetime enables sensing broad band signals in extensive environments. The lifetimes themselves are also sensitive probes of magnetic noises, providing insights into the system's magnetic excitation spectrum. In this chapter, the definition of different coherence lifetimes will be introduced, along with the origin of relaxation and the typical lifetime values.

1.4.1 T_1

T_1 is the longitudinal relaxation time, referring to the decay of the spin polarization along the quantization axis of the spin systems. Namely, one prepares the $|m_s = 0\rangle$ or $|m_s = \pm 1\rangle$ state and sees how long it stays. T_1 is sensitive to the magnetic noise of the frequency corresponding to the EPR energy. In bare diamond, the source of the GHz magnetic noise is mainly from phonons. Therefore T_1 is also referred to as spin-lattice relaxation.

In most diamonds, T_1 is on the order of ms at room temperature and on the order of seconds at a few kelvin [22]. When the NV is approached to magnetic materials, T_1 can also be diminished by magnons. As shown in Fig 1.4.1 (b), the T_1 for the three spin states meets the following conservation equation [23]:

$$\frac{d}{dt}\begin{pmatrix} P_0(t) \\ P_+(t) \\ P_-(t) \end{pmatrix} = \begin{pmatrix} -(\Gamma_+ + \Gamma_-) & \Gamma_+ & \Gamma_- \\ \Gamma_+ & -\Gamma_+ & 0 \\ \Gamma_- & 0 & -\Gamma_- \end{pmatrix} \begin{pmatrix} P_0(t) \\ P_+(t) \\ P_-(t) \end{pmatrix} \tag{1.10}$$

where $P_{0,+,-}$ are the probabilities of the NV being in the $|m_s = 0, +1, -1\rangle$ states, $\Gamma_{+,-}$ are the spin relaxation rates between $|m_s = 0 \leftrightarrow +1\rangle$ and $|m_s = 0 \leftrightarrow -1\rangle$ respectively. The transition rate between $|m_s = -1 \leftrightarrow +1\rangle$ is validated to be zero[24]. Fig 1.4.1 (c) shows the fitting to the three-level model.

1.4.2 T_2^* and hyperfine structures

T_2^* is the transverse relaxation time, referring to the coherence decay of a superposition state. Namely, one prepares the $\frac{1}{\sqrt{2}}\Big[|m_s = 0\rangle + e^{i\phi}|m_s = -1\rangle\Big]$ state and sees how long it stays. Environmental spins near the NV create the inhomogeneity of the local magnetic field, leading to the speed fluctuation of Larmor precession and eventually resulting in relaxation. Therefore T_2^* is also referred to as spin-spin relaxation.

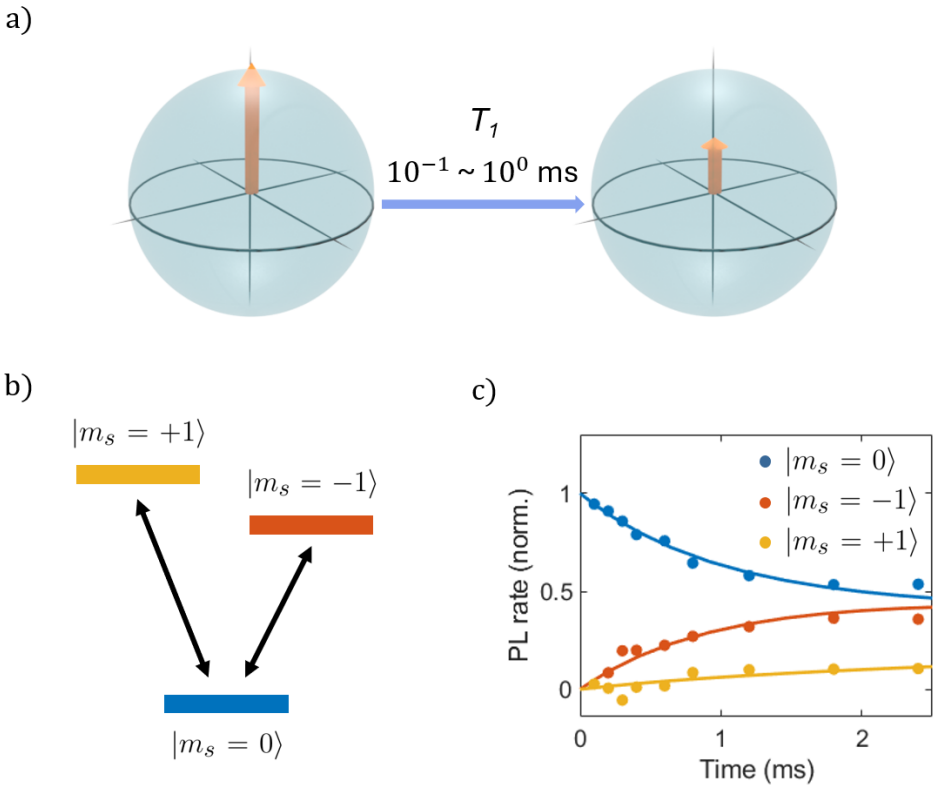

Figure 1.4.1: (a) T_1 relaxation process. (b) Three-level relaxation relation. (c) Three-level T_1 measurement with ensemble NVs in proximity to a piece of exfoliated $CrCl_3$ below the Néel temperature. T_1 is shortened by the magnetic noise from the material. The fitted relaxation rates are $\Gamma_- = 0.50$ ms^{-1} and $\Gamma_+ = 0.08$ ms^{-1}.

T_2^* typically ranges from hundreds of ns to a few μs [12]. The sensitivity of the pulsed ODMR is associated with T_2^*. Usually the lower the power of the microwave, the narrower the dips in the EPR spectrum and the better precision of magnetic field measurement. So one wants to drive with a low microwave power, which requires a long π pulse. If T_2^* is much shorter than the π pulse, the coherence gets lost while applying the microwave, resulting in a low contrast in ODMR.

During the T_2^* measurement, in the meantime of the decreasing coherence, the qubit is also doing Larmor precession in the equator plane. The effective magnetic field driving the Larmor precession is induced from the detuning of the microwave plus the hyperfine intensity of the coupled nuclear spin(s), which are usually the intrinsic ^{14}N or ^{15}N atom and nearby ^{13}C atoms. The NV Hamiltonian with coupled nuclear spins is:

$$H_{\text{full}} = H_{\text{NV}} + \sum_i \left[\gamma_i B_z I_{z,i} + Q I_z^2 + \mathbf{S}\cdot\mathbf{A}\cdot\mathbf{I}\right] \tag{1.11}$$

where i is the index of coupled nuclear atoms, the first term in the parentheses describes the Zeeman effect of nuclear spin, the second term describes quadrupole interaction, and the last term describes the hyperfine coupling, composed of the isotropic Fermi contact interaction and the anisotropic dipolar interaction [21]. For the intrinsic nitrogen atom, the hyperfine tensor only has diagonal components because of the C_{3V} symmetry:

$$H_{hf} = A_{\parallel} S_z I_z + A_{\perp}(S_+ I_- + S_- I_+) \tag{1.12}$$

Fig 1.4.2 (a) demonstrates the energy levels of the intrinsic ^{14}N ($I = 1$), showing that the allowed transitions have three different frequencies for different nuclear spin polarizations. From the table we know that an intrinsic ^{15}N ($I = 1/2$) would have two different frequencies of allowed transitions. A strongly coupled nearby ^{13}C ($I = 1/2$) would further double the number of frequencies, leading to a total number of six (with intrinsic ^{14}N) or four (with intrinsic ^{15}N). The hyperfine tensor is dependent on its position with respect to the NV, so individual ^{13}C atoms are possible to be selectively addressed [26, 27]. In addition to any strongly coupled ^{13}C, the naturally 1.1% abundant ^{13}C atoms in the background also create spin bath noise diminishing T_2^*. Therefore an isotopically purified diamond could elongate T_2^* by two orders of magnitude [12, 28, 29].

Fig 1.4.3 (b-c) shows an experimental T_2^* measurement with an intrinsic ^{14}N. X and Y projections are readout by doing $\frac{\pi}{2}$ pulses around the negative y-axis and the positive x-axis in the end respectively. They are fitted simultaneously as:

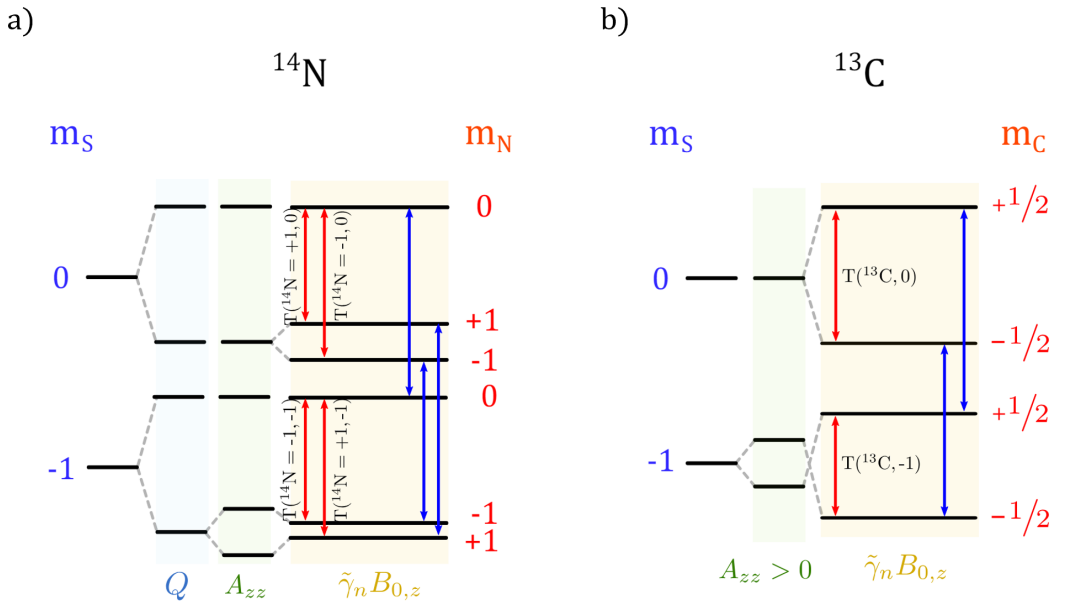

Figure 1.4.2: (a) Energy levels of ^{14}N according to Eq 1.11 and Eq 1.12. First, the quadrupole interaction is proportional to I^2, so the $|I = \pm 1\rangle$ states are still degenerate and are split from $|I = 0\rangle$ by $Q = -4.96$ MHz. Second, the hyperfine interaction is proportional to $S_z I_z$, so only the energies of $|m_s \neq 0, I \neq 0\rangle$ states are changed by $A_{\parallel} = \pm 2.165$ MHz. Third, the Zeeman effect induces sub-MHz change for typical experimental fields $B_z < 0.2$ T. The blue (red) arrows indicate allowed electron (nuclear) transitions. Because the effect of the quadrupole and the nuclear Zeeman term are the same for different electron spin polarizations, the three electron transition frequencies only differ by the hyperfine constant. (b) Energy levels of a strongly coupled ^{13}C. Figure adapted from Ref [25].

Isotope	natural abundance	I	γ (MHz·T^{-1})	Q (MHz)	$A_{\parallel}$ (MHz)	$A_{\perp}$ (MHz)
^{14}N	99.63 %	1	3.0766	-4.96	2.165	2.7 ± 0.07
^{14}N	0.37 %	1/2	-4.3156	0	3.03 ± 0.03	3.65 ± 0.03
^{12}C	98.9 %	0	0	0		
^{13}C	1.1 %	1/2	10.7051	0		

Table 1.2: Nitrogen hyperfine parameters in optical ground states [19, 30–32].

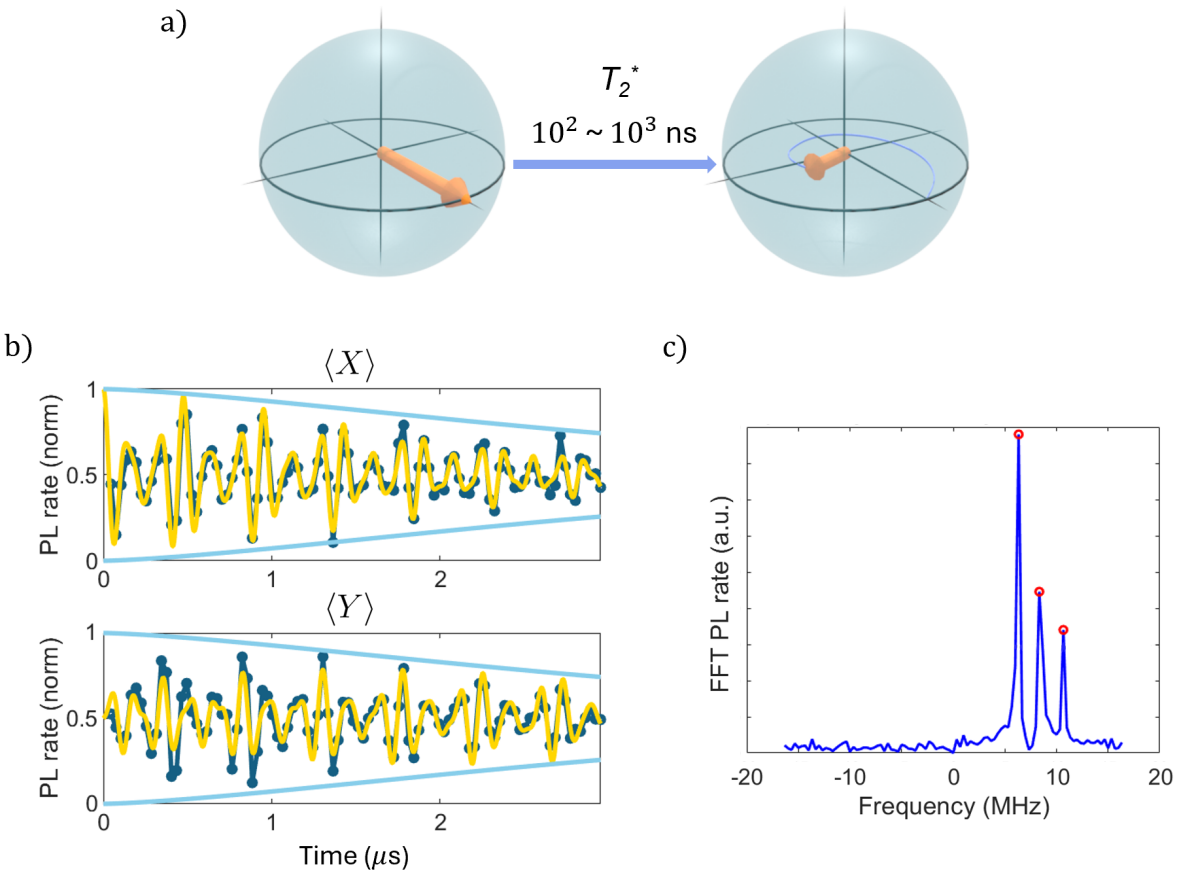

Figure 1.4.3: (a) T_2^* relaxation process. (b-c) T_2^* measurement with a single NV center in a bulk diamond. The microwave is set to be 8.5 MHz detuned. The nitrogen atom of this NV center is N^{14}, which has spin 1 nucleus with splitting 2.165 MHz. As a result the NV center precesses with frequencies 8.5 MHz and 8.5 $\pm$ 2.165 MHz, which is resolved in the Fourier transformed PL rate. T_2^* is fitted to be 2.3 μs. The Fourier peaks have uneven height because the external field polarizes the nuclear spin.

$$\begin{aligned} \langle X \rangle &= \sum_j a_j \cos(w_j t) \\ \langle Y \rangle &= \sum_j a_j \sin(w_j t) \end{aligned} \tag{1.13}$$

where the frequency w_j is the microwave detuning plus the hyperfine shift, the amplitude a_j is proportional to the chance of the nuclear spin being polarized at the corresponding I_z, indicated by the height of the peak in Fourier transformed spectrum.

1.4.3 T_2 and DD sequences

T_2 is the transverse relaxation time when magnetic noise is partially rejected with DD sequences [33]. DD sequences consist of a series of π pulses. The π pulses are evenly spaced with duration τ. The DD sequence works as a band filter, of which the frequency is centered around $\frac{1}{2\tau}$. The more the number of the π pulses, the closer the band filter is to a delta function. As a result, the application of π pulses causes refocusing of Larmor precession fluctuation, extending the coherence time [34]. The DD sequences involved in the work include Hahn (1 π pulse) and XY8xN (8×N π pulses). Typically T_2 is longer than T_2^* by one to two orders of magnitude, and the more the π pulses the longer the T_2.

The sensitivity of ac magnetic field is associated with T_2. A prototype ac magnetic measurement with DD sequence is nuclear magnetic resonance (NMR). Nuclei in a magnetic field precess with a frequency characteristic of the nucleus species and the magnetic field. When the NV is surrounded by an abundant amount of a species of nucleus, the speci can be sensed by DD sequence. When the nucleus characteristic frequency matches the $\frac{1}{2\tau}$, the π pulses will act in the opposite way of refocusing: they accumulate the signal instead of canceling out. Long T_2 is crucial because a long DD sequence is preferred in the sense of accumulating more magnetic signal. For shallow NV, the paramagnetic noise is largely contributed from surface contamination. For deep NV, the way to enlongate T_2 is to reduce nitrogen impurities ($S = \frac{1}{2}$) and ^{13}C nuclei ($I = \frac{1}{2}$) inside the diamond crystal. Same as T_2^* the coherence time can be improved with isotopical engineering [28, 29].

Fig 1.4.4 shows the T_2 measured with one of our isotopically engineered diamonds, with ensemble NV centers implanted 100 nm beneath the surface. The 200 nm isotopically purified ^{12}C (99.99%) diamond layer is grown by CVD on a non-purified diamond substrate.

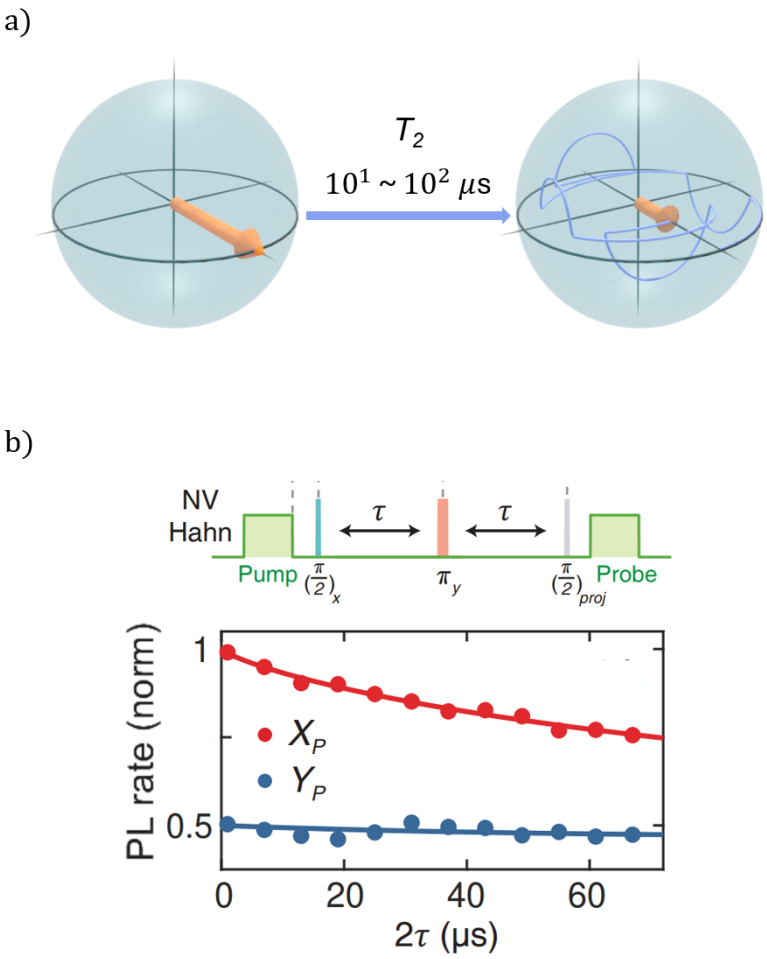

Figure 1.4.4: (a) T_2 relaxation process. Rotations around the x-axis and the y-axis are noise-cancelling π pulses. (b) Top: Hahn Echo sequence. Bottom: T_2 fits 113 μs.

Chapter 2
Experimental Setup

In this chapter, the details of the design and implementation of the experimental setup for quantum sensing with NV centers at cryogenic temperature will be discussed. The NV center is manipulated with the green laser and the microwave. A home-built confocal microscope is used to deliver the green laser and to collect the emitted red photon, working jointly with motorized mirrors to realize spatial resolution. The microwave is delivered with a manually wired coil suspended over the surface of the bulk diamond, through a customized printed circuit board (PCB) mounted inside the cryogenic chamber. The low temperature environment involves a vacuum chamber connected with a closed-cycle helium cooler. The helium cooling and resistor heaters provide temperature control from 3.6K to room temperature controlled with a PID loop.

This chapter first introduces the confocal setup, realizing the initialization and the readout of NV centers and the optical excitation of 2d materials. Then it follows with the microwave and waveform delivery, realizing the manipulation of NV centers and the ac magnetic field excitation of 2d materials. Next the cryostat is discussed, including the basics of a closed-cycle cooling and the geometry of our remodeled chamber shape. In the end the procedures of making 2d material devices are described.

2.1 confocal microscope

As illustrated in Fig 2.1.1, the NV green initialization and the spin-dependent fluorescence detection share the same steering mirror and the same set of confocal lenses. The optical excitation of 2d vdW devices has a separate steering mirror and a separate copy of the first confocal lens, while sharing the second confocal lens with green laser and PL collection. All the photons are input or output through an objective that is mounted inside the cryostat chamber such that we can use one with high NA. The objective is fixed, and the diamond is mounted on a piezo stage with 3-axis mobility (Attocube ANC350).

For the green illumination, a high performance fixed wavelength diode laser modules (Cobolt 06-MLD) with a wavelength of $\lambda = 515$ nm is applied on the diamond. The laser has high speed direct modulation capability and receives pulse signals directly from the AWG. The laser is coupled to a single-mode fiber to reduce the astigmatism. There is also a 75 ± 3 μm pin-hole between a 50 mm and a 175 mm collimation lenses to remove spatial intensity fluctuations.

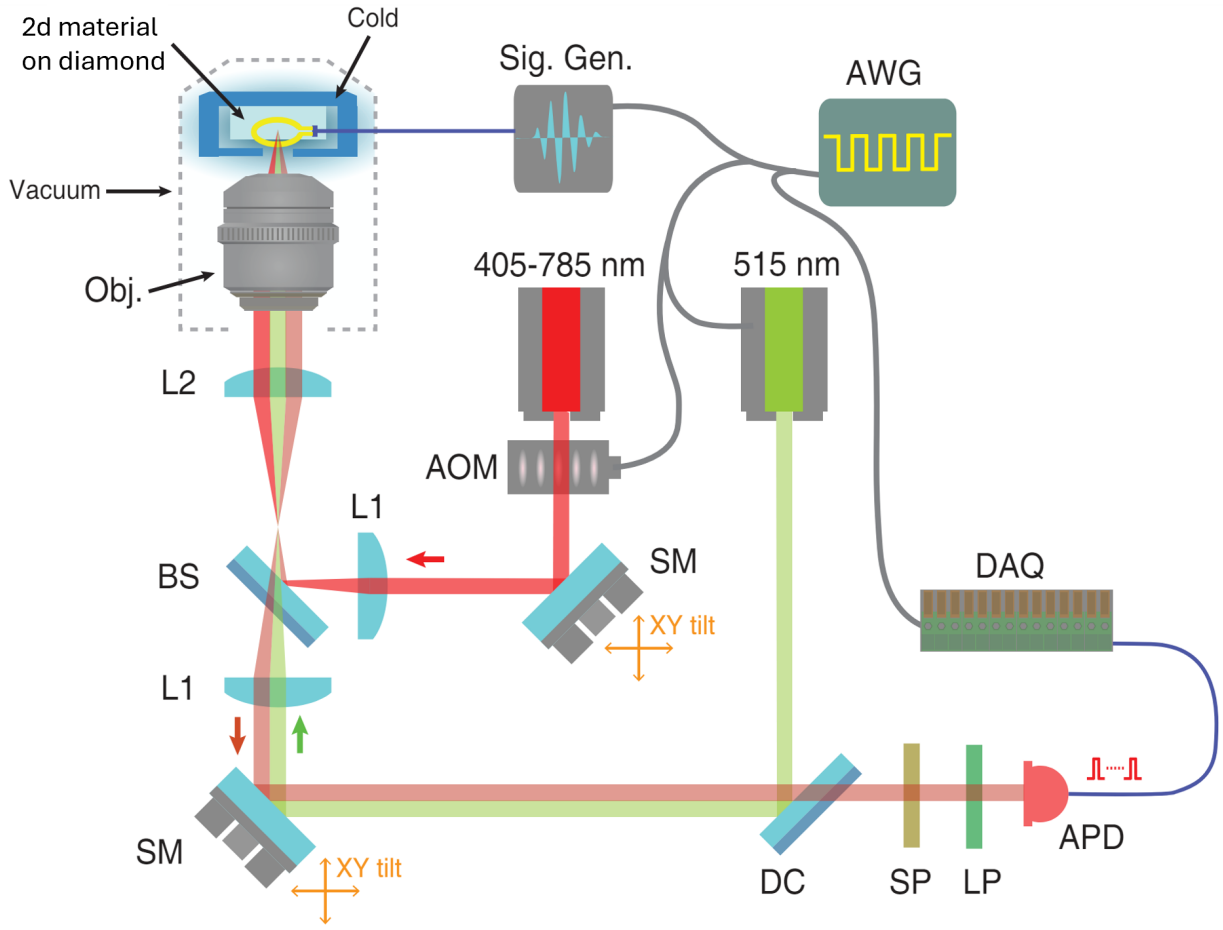

Figure 2.1.1: Confocal setup. The directly modulated 515 nm laser and the AOM-modulated variable laser are input beams. The former one is for NV initialization and the latter one is for optical excitation of 2d devices if needed, both independently steered with two separate motorized mirrors and joined with a beamsplitter. The output photon counts are in red wavelength, filtered from the green laser with a dichroic filter, collected with APD and counted by DAQ or Time Tagger. The microwave is for driving NV center ground state spin level transition. The microwave is generated by SigGen, amplified and delivered to the coil inside the cryostat. Electrical current is output by SDG and can be combined to the coil if needed. Everything is synchronized with AWG, including the modulation of lasers, the collection, the microwave or ac fields.

The second laser for excitation of 2d material is a single-mode fiber-pigtailed laser diode (LP685-SF15, LP405-SF10, LPS-785-FC, LP730-SF15, LP515-SF3, LP660-SF20 or LP637-SF70) mounted on a compact laser diode and temperature controller unit (CLD1010 or CLD1011, depending on the pin code of the pigtail). In order to create laser pulses, the laser is modulated with an acousto-optic modulator (AOM, ISOMET 1250C-848). The first order refraction is used and a single-pass arrangement is chosen. The wavelength variability is realized through unmounting and mounting the pigtails to the controller and the collimator. One needs to re-align the AOM and collimation lenses and re-calibrate output power to get consistent beam size, alignment and power after switching fiber.

The two lasers are independently steered, both with 2-dimensional scanning ability up to 100 μm x 100 μm. In sensing experiments, usually the AOM-modulated laser is fixed in the center of a mapping area and the green laser is scanned.

The NV fluorescence is guided back through the same optical path as the green until split by a dichroic mirror (Semrock LPD02-633RU-25). The fluorescence is eventually focused onto an avalanche photodiode (APD, Excelitas SPCM-780-54-FC) for single photon detection. The photon counts are binned with a data acquisition module (DAQ, National Instruments) using AWG-controlled switches, or are recorded with a time-resolved counter (Swabian, Time Tagger Ultra).

The PL collection beam path is calibrated with a portable red laser mounted on the objective base from the opposite direction. The red laser is a stick pointer that can be clamped inside and along a 2-in lens tube. The lense tube is mounted on the objective thread with adapters, facing outwards from the cryostat. The goal is to make the green laser (Cobolt 06-MLD) beam to totally overlap the red laser (portable pointer), because the NV initialization and PL collection should share exactly the same path until the dichroic mirror. However in reality this is usually found to be challenging to make a perfect alignment. While the confocal lenses (AC508-180-A-ML) are achromatic doublets with AR coating working for 400-700 nm, it was found that the green and red wavelengths don't have exactly the same focal length, thus making the overlapping and simultaneous collimation less optimal. We usually compromise by checking overlapping only at two selected reference points. Still, our collection efficiency is reasonably satisfying, judging from single NV center's Rabi contrast and fluorescence saturation curve.

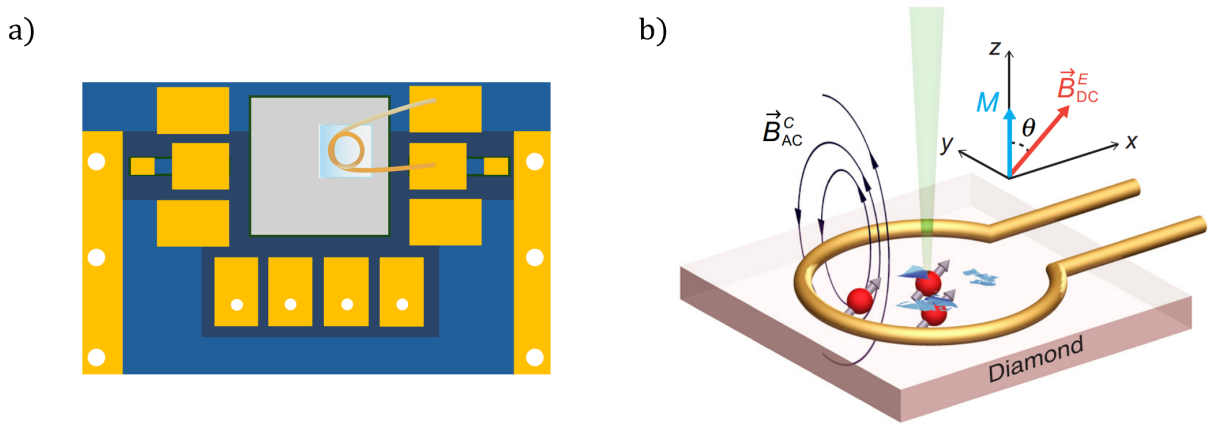

Figure 2.2.1: (a) The microwave is delivered to the NV centers with a coil placed on top of the diamond surface connected to a PCB. (b) The microwave and waveform going through the coil generate the GHz and kHz magnetic field, driving the transition of NV and excitation of 2d materials.

2.2 microwave delivery

Gigahertz microwaves are generated by a signal generator (SRS SG386) and an amplifier (Mini-Circuits ZHL-16W-43-S+). If any ac magnetic field excitation is involved in the measurement protocol, the kilohertz waveforms are generated by a function generator (Siglent SDG2042X) and joined together with the microwaves by a diplexer (Mini-Circuits ZX75-2R15-S+). The pulse timing and the microwave IQ mixing are controlled by the AWG. As shown in Fig 2.2.1, the microwaves and waveforms are delivered through connectors in the cryostat to a PCB, and finally to a wire loop placed on top of the diamond substrate. Both the diamond and the PCB are mounted onto a copper sample holder.

2.3 closed-cycle helium cryostat

The cryogenic station used for our sensing experiment is the Cryostation s-series model manufactured by Montana Instruments. The chamber can be mounted on the optical table and the construction components are as shown in Fig 2.3.1 (a). The chamber shape is remodeled into a non-congruent hexagon shape as shown in Fig 2.3.1 (b) in order to minimize the distance limit between the diamond sample and the permanent magnet outside the chamber. The side wall is set to be perpendicular to the NV center axis for our $[1, 1, 1]$ terminated diamond sample.

Closed-cycle cryocoolers, also known as dry cryostats, can cool the system to as low as liquid helium temperatures (< 4K) with helium gas in a closed loop. The helium only has to be refilled typically every few years if leak tight. With closed cycle helium gas, the

a)

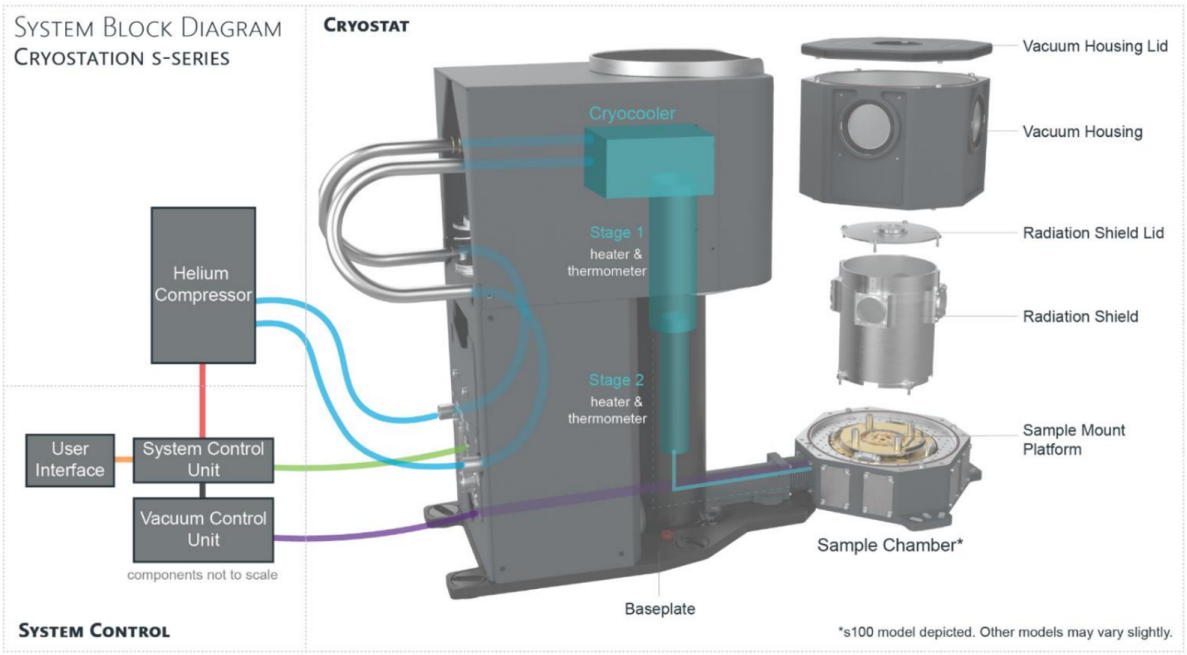

b)

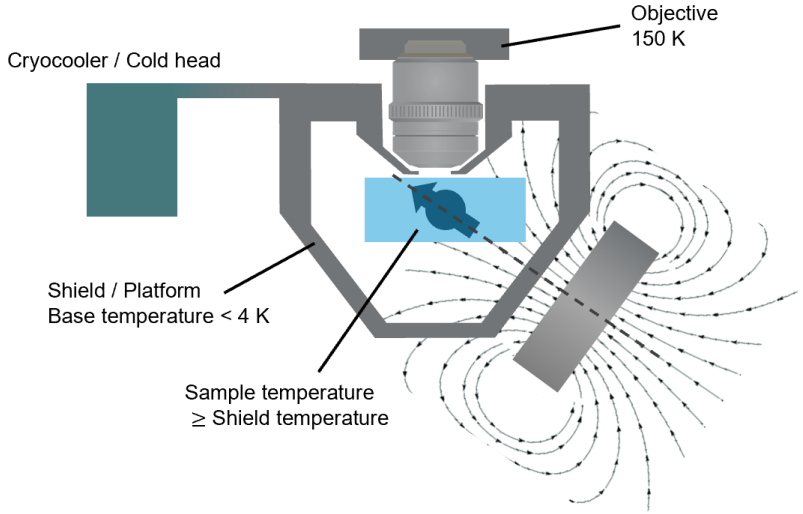

Figure 2.3.1: (a) Schematic of an S-series prototype cryostat. Adapted from Ref [35]. (b) Illustration of the geometry of our remodeled chamber with the permanent magnet outside and the temperatures of different parts in the cryostat.

only resources consumed for cooling are electricity and water-cooling. During a cooling cycle, first, the compressed helium is delivered to the cryocooler, or cold head as usually referred to. Second, at the cold head the heat will be absorbed by the process of helium volume expansion because of the Joule-Thomson effect, resulting in a cooling effect. The cold head has two stages, at base temperature stage 1 is cooled to $\sim$ 40 K and stage 2 is cooled to $<$ 4 K. Third, the helium is then sent back to the compressor. Fourth, the helium is compressed again, and the heat generated during compressing will be transferred to the external environment using some heat exchanger or radiator, ensuring that the compressed helium gas remains at a manageable temperature.

The cold head and the compressor comprise the closed-cycle cooling. One of the hoses supplies a high pressure helium and the other returns the low pressure helium. The cold head is connected to the cold fingers at the bottom of the chamber and to the radiation shield, or referred to as the platform. The shield insulates the sample from room-temperature thermal radiation emitted by the vacuum housing. There are several thermocouples and heaters taped at different parts of the chamber in order to stabilize temepartures for different sections of the chamber. The objective temperature should also be optimized to minimize outgassing. For more versatile vacuum control and leakage prevention we use a dedicated pump (Edward T-station 85) connected with a residual gas analysis filament (RGA) instead of using the built-in vacuum control unit.

2.4 device fabrication and vdW assembly

For the purpose of both fundamental research and industrial application, materials in the low-dimensional limit are studied extensively. Common growth methods include chemical vapor deposition (CVD) and molecular beam epitaxy (MBE). With vdW materials most of the time exfoliated few-layers are preferred because they preserve the pristine lattice quality from the single crystal bulk and are free of reconstruction or strain from a substrate. VdW materials have low binding strength between layers, thus can be cleaved with tapes. Chromium trihalides, which are the main vdW materials of this work, are relatively easy to exfoliate. It is not as easy as graphene, but the few-layer yield is much higher than that of TMD materials.

The following steps introduce two assembly techniques that are used in this work. The first one is Polydimethylsiloxane (PDMS). PDMS is a jelly-like material used as a stamp and is weakly sticky. The materials are directly exfoliated on a PDMS stamp and transferred onto diamond, all at room temperature or very gently heated. The second one is the polycarbonate

(PC) pickup technique. PC is a thin film and is suspended by a piece of PDMS. It rolls over the flake by heating. The whole stack is picked up layer by layer and finally the PC is melted and dissolved on the diamond. We use these two different methods depending on the device requirements.

PDMS transfer

1. PDMS preparation

   (a) Add about 12 grams silicon and 1.2 gram curing to a new and clean petri dish. The curing and silicon ratio can be varied from 1:10 to 1:13 to create different stickiness. The total amount can be varied to create different thickness preferred. Mix with a stir stick about 6 minutes.

   (b) Sonicate (medium power) for about half an hour to reduce bubbles.

   (c) Place the petri dish on a flat and leveled surface. Leave it for more than 24 hours for curing.

2. Exfoliation of flakes on PDMS

   (a) Cut one or a few pieces of PDMS and place them on a glass slide. Transfer the glass slides into the glovebox if needed.

   (b) Use tape to exfoliate thin flakes from crystals and lay down onto the PDMS. Low tack blue tape works better for $CrCl_3$. Scotch tape is preferred to exfoliate hBN, but blue tape also works.

   (c) Gently rub the tape-covered PDMS with tweezer or fingers to eliminate any bubbles.

   (d) May leave it for a couple of minutes, then peel the tape off. Speed may influence yield of thin flakes.

   (e) Search for good flakes under the microscope and mark the place of the flakes. With $CrCl_3$ the optical contrast is low on PDMS, so the thin flakes can only be seen with near-field 100X objective under high illumination. With hBN and some TMD the optical contrast is relatively higher.

   (f) Might cut the PDMS to a size that is suitable for transfer. For soft materials like $CrCl_3$ make the cut far away from the sample because The PDMS is soft and the strain may tear large thin flakes.

3. Transfer of the flake to the diamond

   (a) Mount the diamond substrate on a silicon wafer for handling. If the excitation and initialization is through the back of the diamond, then use tabs of rubber cement on the diamond conors for mounting, such that it is easy to remove the hundreds μm thin diamond after transfer and the middle area where light goes through will not be contaminated.

   (b) Engage the PDMS stack with the target diamond area at room temperature until close. Then either use the automatic stage to press the flake down at a slow speed, or use heating to roll the flake over. With $CrCl_3$ use no or gentle heating ($< 10°C$) even in glovebox in order to avoid flake degradation.

   (c) Retract the glass slide.

4. If making a stack, repeat steps (2-3) and press the new layers on top of the existing layers on diamond.

PC transfer

1. Dome PDMS preparation

   (a) Prepare a thin film of PDMS. Cut the PDMS into small squares.

   (b) Make a new mix of silicon and curing. Use a pipette to put one drop of PDMS gel on each PDMS square films. The PDMS gel will form a dome shape because of the surface tension.

   (c) Leave the dome shape PDMS stamps for more than 24 hours for curing.

2. PC film preparation

   (a) Pour Chloroform into a clean beaker. Then dissolve polycarbonate into it to make a 6% solution by weight.

   (b) Mix the solution overnight without heating. Then store the solution in a dark solution bottle.

   (c) Spray acetone and then IPA to clean two glass slides. Blow them dry.

   (d) Place a drop of PC solution on one of the cleaned glass slides. Place the other one on top and press down. The solution spreads out to cover the whole slide and overflows. Very quickly slide the two slides apart along the long direction, leaving thin smooth PC films on each.

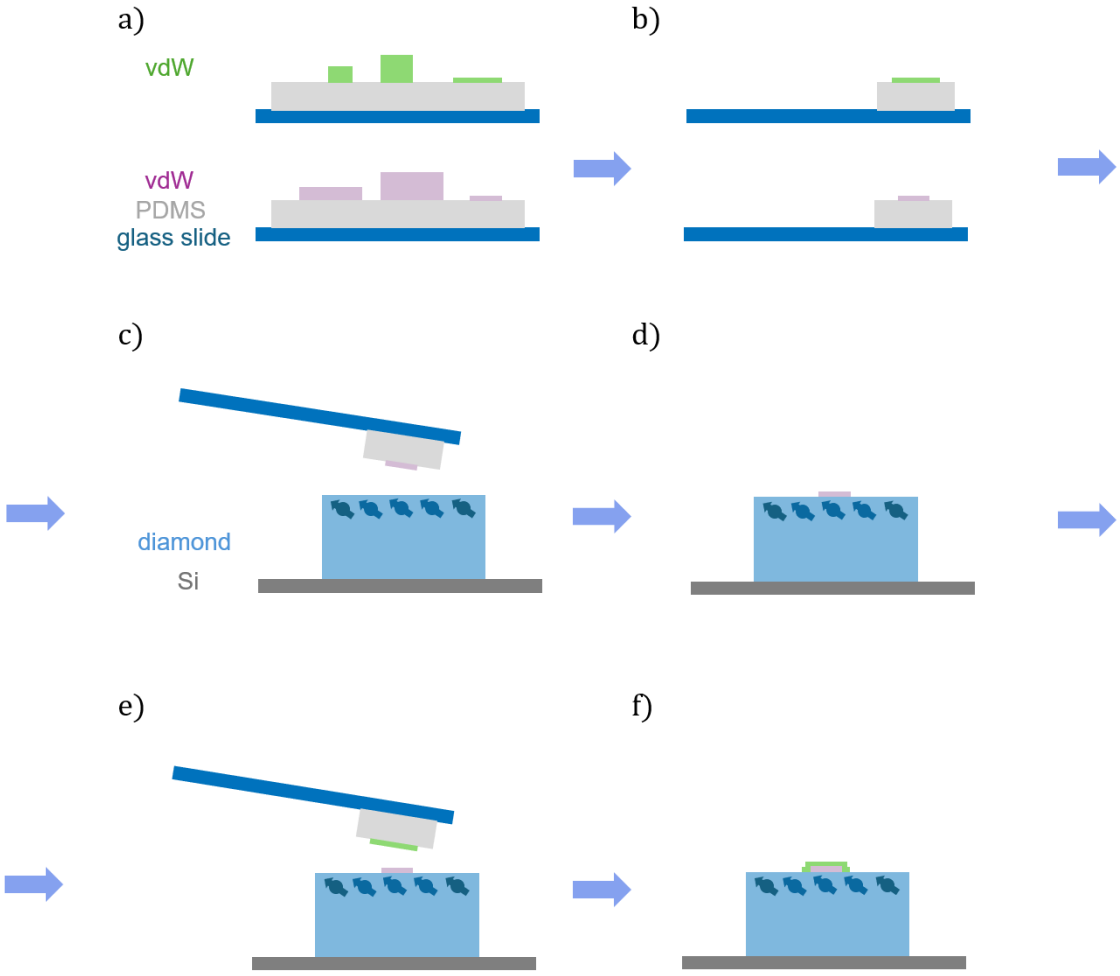

Figure 2.4.1: (a-b) vdW materials are exfoliated on PDMS and layer numbers. PDMS is then cut to suitable sizes for transfer after layer identification with optical contrast. (c-d) The bottom layer of the device stack is dropped onto diamond first. (e-f) The cap layer is dropped last.

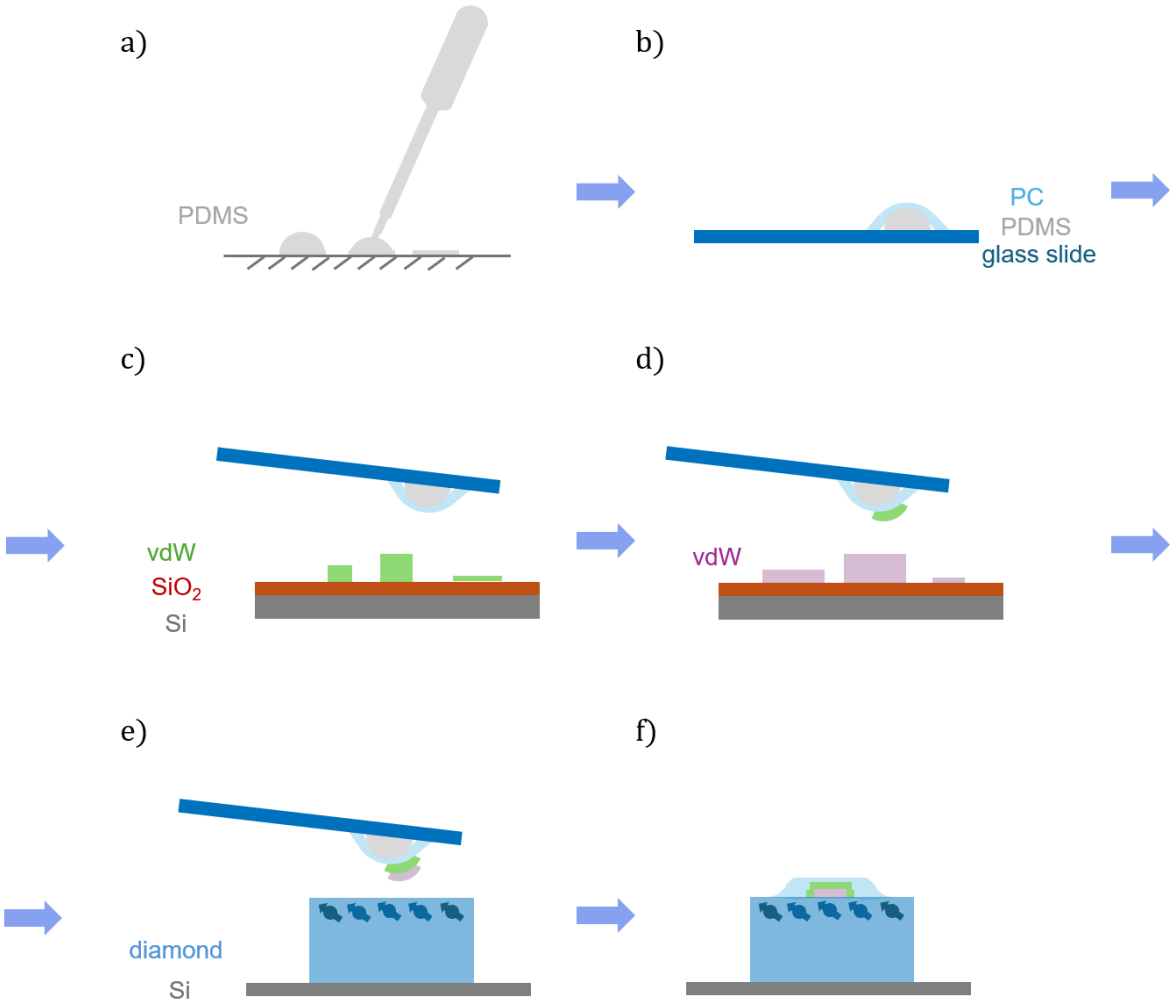

Figure 2.4.2: (a) Make dome shaped PDMS base. (b) Assemble PC/PDMS stamp. (c-d) vdW materials are exfoliated on SiO_2 and layer numbers are identified with optical contrast. PC picks up the stack from top to bottom layers. (e-f) The stack is dropped onto diamond with melted PC.

(e) Leave it to dry out for more than 10 minutes.

3. Stamp preparation

   (a) Place a dome shape PDMS on a new glass slide near one end.

   (b) Cut a square shape of double-sided tape. In the center cut out a smaller square.

   (c) Stick the double-sided tape onto the PC film. Cut the PC film with a razor blade to the shape of the double-sided tape. Then gently peel them off and avoid any wrinkles in the PC film.

   (d) Stick the other sided of the double-sided tape to the glass slide centered around the PDMS. Gently press down the tape, such that the PC attaches to the PDMS firmly hold by the tape on the ends.

4. Pickup stacks

   (a) Flakes are exfoliated onto cleaned SiO_2 wafers. The acetone and IPA sonication can be followed by a 30 second O_2 plasma cleaning for higher yield.

   (b) Engage the PC with the flake at room temperature. The flake should be slightly off the center of the dome shape stamp. Bring the edge of contacting close to the target flake. The advantage of using a dome shaped stamp is that the contacting position and rolling direction is highly predictable.

   (c) Heat up to 70-130 ° C to roll the PC over the flake. During cooling back down the flake is picked up. Higher temperature gives a higher chance of picking the flake up, but PC may lose elasticity and get wrinkles after heating to high temperature multiple times.

   (d) After cooling back to room temperature ($< 35°$ C), disengage the stamp with the stage.

   (e) If the stack has multiple layers of vdW materials, repeat step (b-d).

5. Transfer the stacks onto diamond

   (a) Engage the stamp with the stack fully to the diamond surface at room temperature.

   (b) Heat to 150 - 200 °C until the PC melts and breaks from the PDMS. With home-built transfer stages, the melting temperature could be different, depending on how close the thermocouple is placed with respect to the resistor heater and to the sample in the design.

(c) Disengage the PDMS from the diamond at the PC melting temperature. Then cool down the diamond back to room temperature.

(d) Dissolve the PC in chloroform. If the device is not interactive with chloroform, it can be immersed in chloroform overnight. If the device can interact with chloroform, minimize the time of dissolving by preparing multiple beakers of clean chloroform and immerse the diamond for a few seconds in each. It is also possible to keep the PC without dissolving when taking NV measurements. It was found the photoluminescence rate in 638-800 nm increases by only 5% on the PC-covered region compared to the non-covered region with ensemble NV centers at 4K.

(e) Take the diamond off the silicon wafer and mount it on the sample holder of the confocal microscope.

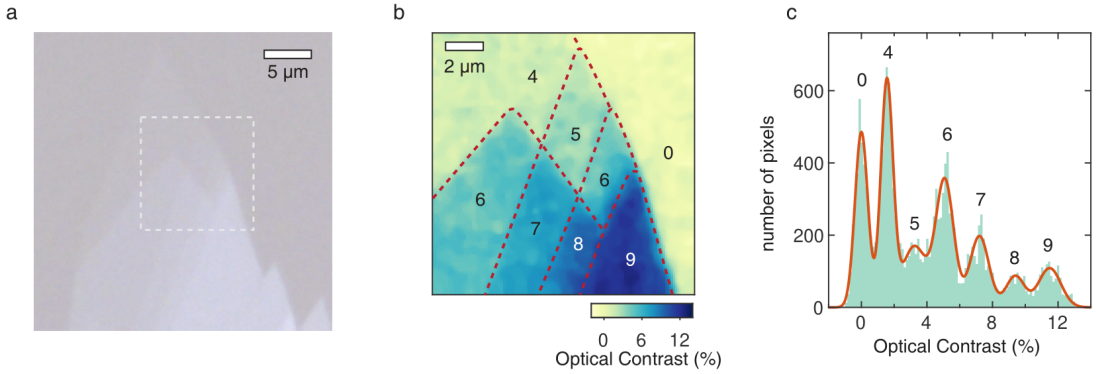

Figure 2.4.3: The raw photo (a) and the extracted optical contrast (b, c) of 4∼9 layers of $CrCl_3$ on PDMS. The area of (b) is illustrated as the white square in (a). The histogram (c) of optical contrast is able to resolve and fit Gaussian peaks for each individual layer thickness. The numbers in (b, c) represent the layer number.

layer identification with optical contrast The layer thickness of $CrCl_3$ on PDMS is identified with optical contrast before transferring onto diamond. The identification is operated inside our Argon-filled glovebox in order to avoid sample degradation. With $CrCl_3$ it is found that three layers or thinner flakes on PDMS is hardly resolved, while thicker flakes can be clearly determined with optical contrast. The optical contrast C is defined as the percentage of the brightness difference on flake versus on PDMS. The brightness I is weighted over the RGB channels, and the weight we choose is about optimized to separate the histogram peaks. Take few-layer $CrCl_3$ as an example, the optical contrast on PDMS with our objective and camera is defined as:

$$
\begin{aligned}
I &= 0.20 \cdot I_R + 0.38 \cdot I_G + 0.42 \cdot I_B \\
C &= (I_{\text{flake}}/I_{\text{substrate}} - 1) \times 100\%
\end{aligned}
\tag{2.1}
$$

In order to ensure the layer identification, we subsequently exfoliate $CrCl_3$ on PDMS, take optical image, then transfer $CrCl_3$ to 90-nm SiO_2 substrate and take optical image again. The optical contrast of $CrCl_3$ on SiO_2 is well characterized and reported in many previous works [36]. This allows us to decide the layer number. We repeat this procedure multiple times to ensure the one-to-one correspondence between optical contrast on PDMS and the number of layer.

Chapter 3
Measurement Protocols

3.1 ODMR with 2d magnets

As described in Ch 1.2, ODMR is the most basic measurement of magnetic field with NV centers. The frequency of an applied microwave is swept and the number of collected photons diminishes only when the frequency corresponds to the energy splitting between the spin zero state to the other two spin polarization. Mapping ODMR with scanning NV has been used to characterize vdW magnets[37], especially investigating domain wall evolution[38] and moire patterns[39]. In this work we use ensemble NV to map ODMR around vdW magnets.

A bias field is usually applied with 2d material sensing, and the bias field is subtracted from the field to extract the stray field of 2d materials. In our case the bias field is applied with a permanent magnet for our ensemble NV in bulk diamond. The magnet is aligned to be $\theta = 35.3^\circ$ tilted away from the diamond surface, conforming with one of the four axes of the ensemble NV centers.

The magnetization of 2d materials induces a stray field of a profile that is strongest and most rapidly changing at the flake edge and decays away on either side. The stray field changes the ground state energy of NV centers at proximity through Zeeman splitting, and thus can be inferred from the ODMR spectrum.

When the dc field is perfectly aligned with the NV center axis, the ground-state spin $|0\rangle \rightarrow |\pm 1\rangle$ transition frequency is determined by a linear Zeeman splitting: $f_\pm = D_0 \pm \gamma_e \cdot B_{\mathrm{NV}\|}$, where $D_0 = 2.87$ GHz is the zero-field splitting, $\gamma_e = 28$ MHz/mT is the gyromagnetic ratio and $B_{\mathrm{NV}\|}$ is the external field along the NV axis. With a magnetic flake present, the sample stray field $\vec{B}^S$ induces an additional frequency shift $\Delta f(\vec{r})$. In the optically detected magnetic resonance (ODMR) spectrum, we consider the first order approximation:

$$\Delta f(\vec{r}) = -\gamma_e \cdot B^S_{\mathrm{NV}\|}(\vec{r}) \tag{3.1}$$

for the $|0\rangle \rightarrow |-1\rangle$ transition, where Δf is linearly dependent on the parallel component of the local sample stray field. $B^S_{\mathrm{NV}\perp}$ does not affect the ODMR measurements within our experimental precision; however, we shall see that it induces a resolvable background signal in our ac sensing measurements in Ch 3.2. Determining the spatial distribution of magnetization from the stray field requires full two-dimensional imaging and some additional constraint [40].

3.1.1 *Fourier transform approach for arbitrary patterns of magnets*

$\vec{M}(x, y, t)$ describes the magnetization profile at diamond surface ($z = 0$). It assumes the thickness of the magnet is zero, which makes sense because the vdW materials are typically sub-nanometer to a few nanometers while the NV centers are tens to hundreds of nm away. $\vec{M}(x, y, t)$ can be any non-infinite functions. For example, with a uniform magnet, the magnetization is described with:

$$\vec{M}(x, y, t) = \begin{cases} \sigma \cdot (\cos\theta\hat{z} + \sin\theta\cos\phi\hat{x} + \sin\theta\sin\phi\hat{y}), & \text{if } (x, y) \text{ on flake} \\ 0\hat{z} + 0\hat{x} + 0\hat{y}, & \text{if } (x, y) \text{ not on flake} \end{cases}$$

(3.2)

where θ is the angle between the magnetic moment and out-of-plane direction, ϕ is the in-plane angle. At any moment of time t, the stray field *ref* would be:

$$\begin{aligned} \widetilde{M}_{x,y,z}(k_x, k_y) &= \mathcal{F}[M_{x,y,z}(x, y)] \\ \begin{pmatrix} \widetilde{B}_x \\ \widetilde{B}_y \\ \widetilde{B}_z \end{pmatrix} &= -\frac{\mu_0}{4\pi}\frac{e^{-|z|k_r}}{k_r} \begin{pmatrix} k_x^2 & k_x k_y & -ik_x k_r \\ k_x k_y & k_y^2 & -ik_y k_r \\ -ik_x k_r & -ik_y k_r & -k_r^2 \end{pmatrix} \cdot \begin{pmatrix} \widetilde{M}_x \\ \widetilde{M}_y \\ \widetilde{M}_z \end{pmatrix} \\ B_{x,y,z}(x, y) &= \mathcal{F}^{-1}[\widetilde{B}_{x,y,z}(k_x, k_y)] \\ B_{\mathrm{NV}} &= \cos(35.3^\circ)B_x + \sin(35.3^\circ)B_z \end{aligned} \tag{3.3}$$

where $k_r = \sqrt{k_x^2 + k_y^2}$. $z = 100$ nm is the NV center depth in our diamond substrates.

3.1.2 *semi-infinite dipole sheet approach for out-of-plane magnets*

Under the approximation of a semi-infinite, zero thickness dipole sheet, the vector stray field $\vec{B}^S = (B_x^S, B_y^S, B_z^S)$ due to a magnetic thin flake with out-of-plane polarization ($+z$) is [41, 42]:

$$
\begin{aligned}
B_x^S(\vec{r}) &= \frac{\mu_0 \sigma_z}{2\pi} \cdot \frac{z}{x^2+z^2} \\
B_y^S(\vec{r}) &= 0 \\
B_z^S(\vec{r}) &= -\frac{\mu_0 \sigma_z}{2\pi} \cdot \frac{x}{x^2+z^2}
\end{aligned} \tag{3.4}
$$

where $\vec{r} = (x, y, z)$, the semi-infinite dipole sheet resides in the $z = 0$ plane for $x < 0$ with the y-axis being its edge, μ_0 is the vacuum magnetic permeability and σ_z is the areal magnetization density. With $B_y^S = 0$ and an NV center axis in the xz-plane, we can decompose the stray field in the coordinate system parallel and perpendicular to the NV axis, i.e. $\vec{B^S} = (B_x^S, B_z^S) \rightarrow (B_{\mathrm{NV}\parallel}^S, B_{\mathrm{NV}\perp}^S)$ where

$$
B_{\mathrm{NV}\parallel}^S(\vec{r}) = \frac{\mu_0 \sigma_z}{2\pi} \cdot \left(\frac{z}{x^2+z^2} \sin(\theta) - \frac{x}{x^2+z^2} \cos(\theta) \right) \tag{3.5}
$$

$$
B_{\mathrm{NV}\perp}^S(\vec{r}) = \frac{\mu_0 \sigma_z}{2\pi} \cdot \left(\frac{z}{x^2+z^2} \cos(\theta) + \frac{x}{x^2+z^2} \sin(\theta) \right) \tag{3.6}
$$

Here, $\theta = 54.74°$ is the NV center polar angle (i.e., NV axis is parallel to $(\sin(\theta), 0, \cos(\theta))$ in xyz coordinates), and $z = -60 \sim -100$ nm is the NV center depth.

3.1.3 broadening of ODMR spectrum with ensemble NV

For ensemble NV samples, the green light reads out a collective signal of NV centers within the beam size. The ODMR line shape maintains a narrow shape when the NV centers experience nearly uniform magnetic field (far from the flake), but near the edge of the flake where the magnetic field is rapidly changing spatially, the ODMR signal becomes broadened. For fixed z depth, the shape of the ODMR dip measured at a location $\vec{r} = (x, y)$ relative to the flake's edge at $x = 0$ can be described by an integral of Lorentzian functions with varying center frequencies f_0 due to the local magnetic field, modulated by a Gaussian envelope which represents the density of NV centers probed over the beam size:

$$
I(f, \vec{r}) = A \int d^2\vec{r'} \, \frac{e^{-(\frac{\vec{r'}-\vec{r}}{\sqrt{2}\sigma})^2}}{2\pi\sigma^2} \cdot \frac{(w/2)^2}{(f - f_0(\vec{r'}))^2 + (w/2)^2} \tag{3.7}
$$

where the integral is over a circularly-symmetric beam spot centered about $\vec{r}$. $I(f, \vec{r})$ models the experimentally measured PL intensity with the beam center at $\vec{r}$ as a function

of the microwave frequency f. The beam width σ is determined from single NV PL scans to be 0.17 μm. The zero-gradient linewidth w for the Lorentzian line shape is estimated to be 8 MHz by measuring NV centers away from any flakes using the same microwave power settings. The center frequency $f_0(\vec{r'})$ as a function of position is determined by the stray field of the flake, using Eq 3.5 and 3.1. Since $f(\vec{r'})$ only depends on x', the coordinate perpendicular to the flake's edge, Eq 3.7 can be simplified to a 1D integral by integrating out the y'-coordinate:

$$I(f,x) = A \int dx' \, \frac{e^{-(\frac{x'-x}{\sqrt{2}\sigma})^2}}{\sqrt{2\pi}\sigma} \cdot \frac{(w/2)^2}{(f - f_0(x'))^2 + (w/2)^2} \tag{3.8}$$

We fit the experimental ODMR traces as a function of the distance x simultaneously to Eq 3.8. Explicitly, z, θ, σ, and w are fixed parameters determined from other measurements, A is a free parameter that varies for each data set, and σ_z is a common free parameter used for all data sets. An example of this fitting procedure is shown in Fig. 2a of the main text, where we determine $\sigma_z = 86 \pm 5 \; \mu_b/\text{nm}^2$ for a 9-layer $CrBr_3$ flake (Flake B).

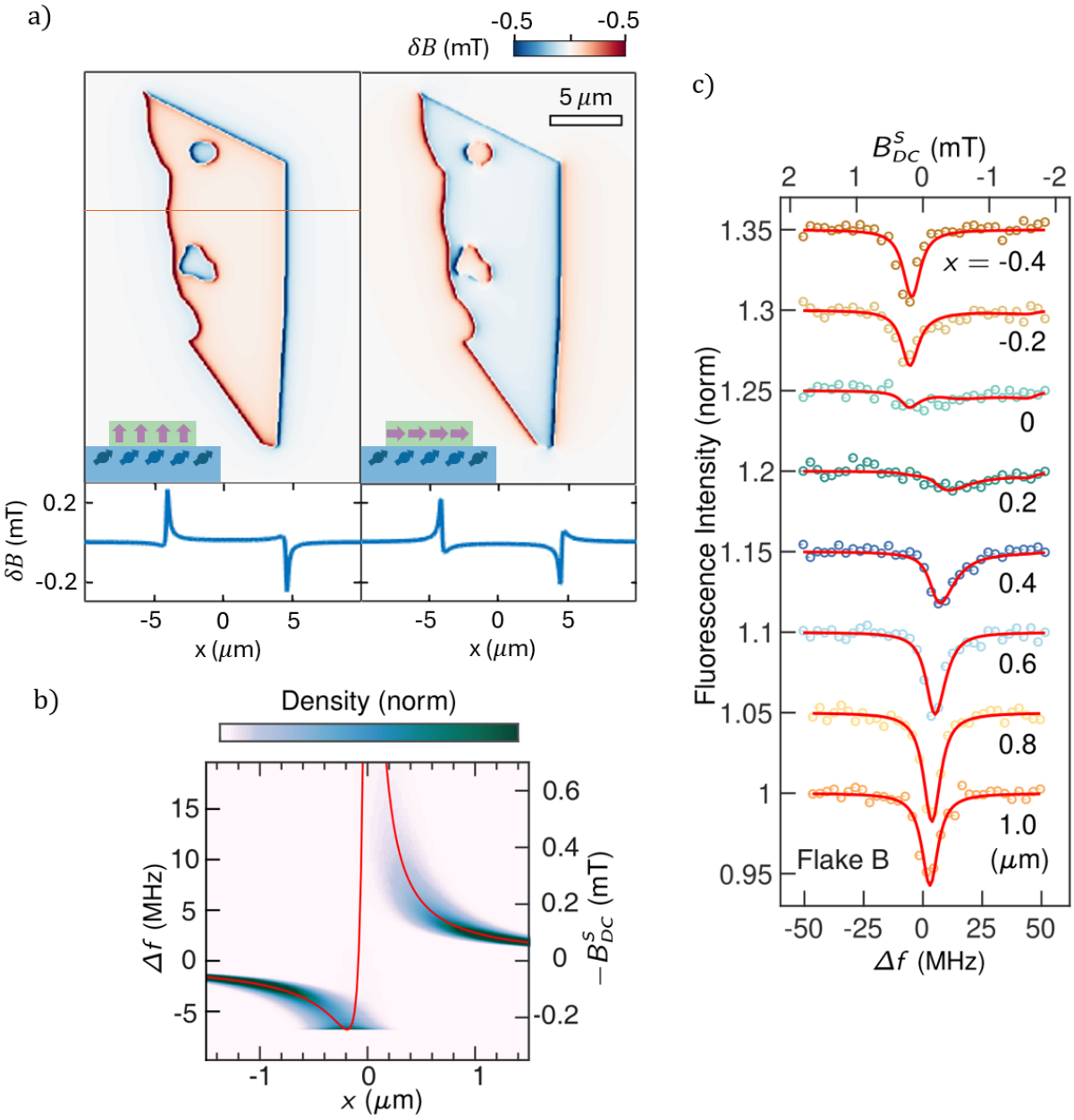

Figure 3.1.1: (a) Simulation of stray field of out-of-plane magnets (left) and in-plane magnets. The linecut of the simulated field along the orange line is plotted at the bottom. The magnetization and NV center direction are illustrated as the insets. The simulation assumes an NV depth of 100 nm and a magnet spin density of 14.7 μ_B/nm^2. (b) Blurring effect when measuring the linecut with ensemble NV samples, originating from the drastic spatial change of stray field within the laser beam size. The simulation is a linescan perpendicularly across the right side edge of an out-of-plane magnet. $x = 0$ μm means the edge. It assumes a beam size of a 2d Gaussian with the standard deviation as 170 nm. (c) ODMR frequency spectrum at selected points in (b).

3.2 ac susceptometry

ac susceptibility is a powerful technique to study dynamical magnetic properties. Measuring ac stray field from 2d magnetic flakes is challenging as the oscillating portion of magnetization is tiny and thus requires close proximity and great sensitivity of the probe. Here we present a technique where NV centers can measure ac susceptibility with sensitivity down to tens of μT. In this section, an overview of ac susceptibility definition and interesting measurements on representative bulk materials are first presented; then the setup and modulation sequence of ac susceptometry of NV are introduced; careful analysis including artificial signal and SI unit conversion are also detailed.

3.2.1 ac susceptibility

ac susceptibility measures the spin collective behavior under a small oscillation magnetic field. It is a useful tool to study the phase transitions, and dynamic magnetic properties such as domain walls in ferromagnets and vortex in superconductors. The definition of susceptibility is:

$$\chi = \lim_{H \to 0} \frac{M}{H} \tag{3.9}$$

As shown in Figure 3.2.1 (a), in ac susceptibility measurement a time-varying sinusoidal magnetic field $H_{\mathrm{ac}} \cos(\omega t)$ is applied to the sample. Meanwhile a static magnetic field H_{dc} may or may not be applied. The time-dependent portion of the magnetization $\propto H_{\mathrm{ac}} \cos(\omega t + \phi)$, where ϕ describes the lag between the response and the excitation. Namely the ac susceptibility is defined as:

$$\begin{aligned} H &= H_{\mathrm{dc}} + H_{\mathrm{ac}} \cdot e^{i\omega t} \\ M &= M_{\mathrm{dc}} + M_{\mathrm{ac}} \cdot e^{i\omega t} \\ \chi_{ac} &= \chi' - i\chi'' = \frac{M_{\mathrm{ac}}}{H_{\mathrm{ac}}} \end{aligned} \tag{3.10}$$

Ac susceptibility provides a more extensive characterization of dynamic properties of spins than the dc susceptibility measurements where the sample properties are assumed static. One can vary the static field amplitude H_{dc}, the sinusoidal field amplitude H_{ac}, and the ac frequency ω in order to explore the relaxation process in unique materials. Figure 3.2.1 (b-d) presents some representative systems where the application of ac susceptibility reveals

interesting properties.

ferromagnets Figure 3.2.1 (b) plots the susceptibilities of an isotropic three-dimensional ferromagnet with a constant dc field. The net magnetization as a function of temperature has a discontinuity from paramagnetic phase to ferromagnetic phase, therefore it is a first-order phase transition and the susceptibility blows up at the long-range order transition temperature T_C. Usually the χ'/ minimum and χ'' onset coincide and can precisely determine the T_C.

spin ice Fig 3.2.1 (c) top panel plots the imaginary component versus the real component of ac susceptibility of a spin ice material. Spin ice are usually systems where a large number of degenerate ground state configurations are available, such that no long-range order down to low temperatures can form. For example the identified spin ice systems in the early ages are some rare-earth pyrochlores, where the four spins on the corners of each lattice tetrahedron have to satisfy $\sum_i \vec{S}_i = 0$[43]. The frequency dependence of the ac susceptibility is described as [44]:

$$\chi_{ac} \propto \frac{1}{(1 + i\omega\tau_c)^\beta} \tag{3.11}$$

or

$$\begin{aligned} \chi' &= \chi_0 \cdot \cos^\beta(\arctan(\omega\tau_c)) \cdot \cos(\beta \cdot \arctan(\omega\tau_c)) \\ \chi'' &= \chi_0 \cdot \cos^\beta(\arctan(\omega\tau_c)) \cdot \sin(\beta \cdot \arctan(\omega\tau_c)) \end{aligned} \tag{3.12}$$

where τ_c is the cutoff of a wide range of long relaxation spectrum of spin ice, β is between 0 and 1, $\beta = 1$ corresponds to the Debye relaxation with a single dispersion. On each curve in Figure 3.2.1 (c) top panel, data points on the right side (bigger χ') correspond to low frequency, and in the $\omega \to 0$ limit the curve should make a perpendicular angle with the χ'-axis; data points on the left side (smaller χ') corresponds to high frequency, and in the $\omega \to \infty$ limit it should make an angle of $\beta\pi/2$ against the χ'-axis. Each curve fits to equation 3.11 and produces a fitted β and τ_c. The fitted τ_c as a function of temperature is plotted in the bottom panel, illustrating a faster increase than what should be expected for simple thermal activation which scales as $1/T$.

superconductors Fig 3.2.1 (d) plots a theoretical frequency dependence of superconductor ac susceptibility. Superconductors themselves don't carry spin moments, but the current induced by ac magnetic field through the Meissner effect creates the counter field, thus the susceptibility is negative. With type I superconductors the magnetic flux is totally screened, therefore $\chi' = -1$ and $\chi'' = 0$. With type II superconductors between the two transition fields, the ac susceptibility is related to vortex movements. The current forming the vortex experience Lorentz force under the ac magnetic field, so the flux line starts moving; the moving vortex generates an electric field, which in return impedes the vortex motion. The result of the two balancing forces is [45]:

$$\begin{aligned} \chi' &= \frac{\sinh u + \sin u}{u(\cosh u + \cos u)} - 1 \\ \chi'' &= \frac{\sinh u - \sin u}{u(\cosh u + \cos u)} \end{aligned} \tag{3.13}$$

where $u \propto \sqrt{\omega}$. u also depends on the amplitude of ac field, and the dimension and the normal state resistivity of the superconductor. At low frequencies, the ac field totally penetrate the superconductor, yileding no susceptibility; at high frequencies, the ac field almost only penerates the surface, yielding the same situation as a type I superconductor.

3.2.2 setup and sequences

Our ac susceptibility technique is based on controlling the NV spin precession with an XY8-N sequence [50] while exciting the material with a synchronized ac magnetic field. As shown in Fig. 3a in the main text, the sequence contains $8N + 2$ pulses on the NV center spin:

$$\left(\frac{\pi}{2}\right)_x - \left[\pi_x - \pi_y - \pi_x - \pi_y - \pi_y - \pi_x - \pi_y - \pi_x\right]^N - \left(\frac{\pi}{2}\right)_{\text{proj}}$$

The ac magnetic field is dynamically coupled to the NV center's spin precession using frequency-selective quantum control sequences [51, 52]. The π-pulses are separated by a free evolution time τ, while the ac excitation field is resonant with this sequence: at zero lag, the ac field switches sign for every π-pulse (i.e., $f_{AC} = 1/(2\tau)$). The relative lag between the XY8-N sequence and the ac excitation field is denoted as $t_0 = \frac{\delta}{\pi} \cdot \tau$, where δ is the phase delay in radians. Each π_j pulse flips the NV superposition state around the j-axis on the Bloch sphere by a half-circle (e.g. $\frac{1}{\sqrt{2}}(|0\rangle + e^{-i\varphi}|-1\rangle)$ is turned into $\frac{1}{\sqrt{2}}(|0\rangle + e^{i\varphi}|-1\rangle)$ by a π_x pulse, negating the phase accumulated prior to the pulse. Thus, the net action of

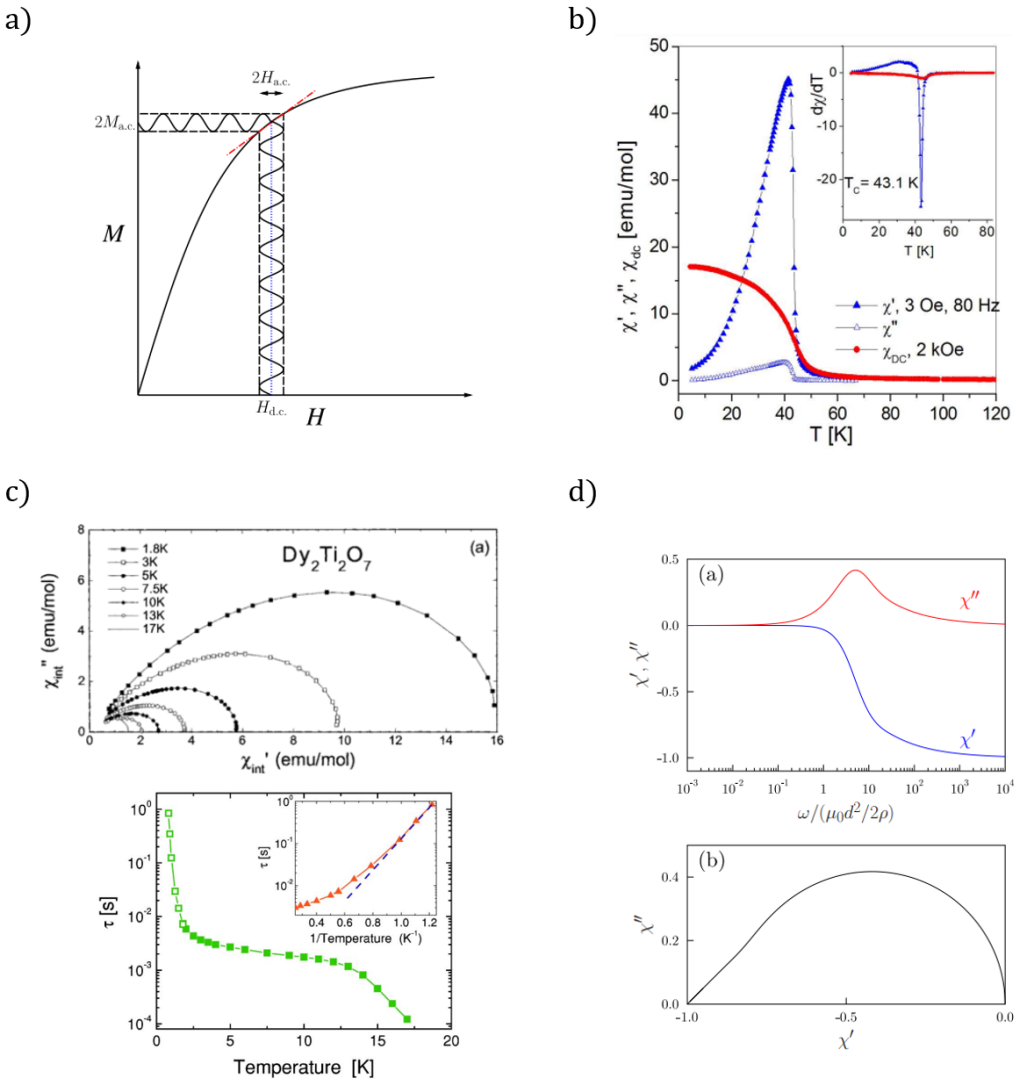

Figure 3.2.1: (a) Illustration of ac susceptibility measurement. The magnetization responds to an oscillating magnetic field applied in addition to an optional constant field. Figure adapted from Ref [46]. (b) The temperature dependence of the real and imaginary components of ac susceptibility and dc susceptibility measured with a molecular 3d ferromagnet $[Fe^{II}(H_2O)_2]_2[Nb^{IV}(CN)_8]\cdot 4H_2O$. Figure adapted from Ref [47]. (c) Frequency dependence of ac susceptibility measured on a spin ice material (top) and extracted relaxation cutoff from another measurement (bottom). Figure adapted from Ref [48, 49]. (d) Simulation of frequency dependence of ac susceptibility of Type II superconductors. Figure adapted from Ref [46].

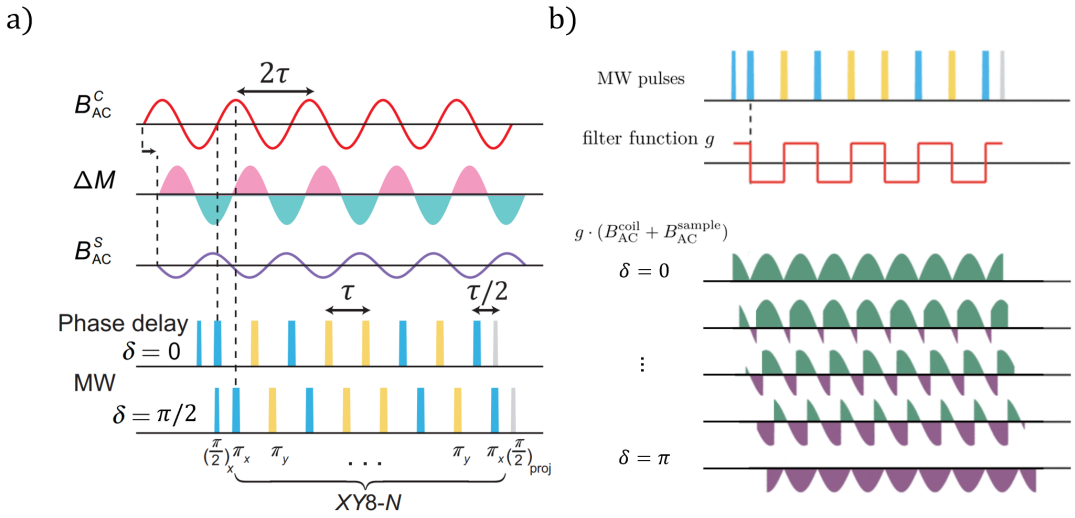

Figure 3.2.2: (a) Experimental sequence: the oscillating coil field excites oscillating magnetization change, with a possible phase shift, of a 2d material flake. The magnetization change in turn produces an extra oscillating field. An XY8-N DD sequence is applied to the NV center to lock-in the total ac field. The phase delay between the coil field and the microwave pulses can be tuned to isolate either the in-phase ($\delta = 0$) or out-of-phase ($\delta = \pi/2$) magnetization response. (b) The filter function g of the microwave pulse sequence is as described by Eq 3.15. The total ac field is modulated by the filter function g as described by Eq 3.3.1 and is dependent on the delay δ.

the π-pulses is to rectify the phase accumulation due to the ac field, which would otherwise vanish by time integration. The rotation around orthogonal axes in succession decouples pulse errors.

3.2.3 determination of the maximum precession angle

The total accumulated phase φ_{end} at the end of the evolution is optically read out after a $\left(\frac{\pi}{2}\right)_x$ projection pulse. The measured NV center PL is proportional to $X_P(\delta) = A\cos(\varphi_{\text{end}}(\delta))$, where X_P is the x-projection of the final superposition state on the Bloch sphere and A is the measurement contrast. We first consider that the external dc field is perfectly aligned along the NV center axis such that the frequency shift of the NV spin state is due to only the component of the ac field parallel to the NV axis:

$$\varphi_{\text{end}}(\delta) = \int_{t_0}^{t_0+8N\tau} 2\pi\gamma_e \cdot \widetilde{B}^T_{\text{NV}\parallel}(t) \cdot M\,(t - t_0)\,dt \tag{3.14}$$

where $t_0 = \delta \cdot \tau/\pi$, and the modulation function representing the effect of the π-pulses is:

$$M(t) = \begin{cases} -1 & 0 \leqslant \mathrm{mod}\left(\frac{t}{\tau} - 0.5, 2\right) < 1 \\ +1 & 1 \leqslant \mathrm{mod}\left(\frac{t}{\tau} - 0.5, 2\right) < 2. \end{cases} \tag{3.15}$$

In the chapter we use the $\widetilde{}$ overbar to represent the amplitudes of ac fields. $\widetilde{B}^T_{\mathrm{NV}\|}(t)$ is the total ac field parallel to the NV center axis, consisting of the excitation coil field $\widetilde{B}^C_{\mathrm{NV}\|}$ and the sample ac response $\widetilde{B}^S_{\mathrm{NV}\|}$:

$$\begin{aligned} \widetilde{B}^T_{\mathrm{NV}\|}(t) &= \widetilde{B}^C_{\mathrm{NV}\|}(t) + \widetilde{B}^S_{\mathrm{NV}\|}(t) \\ &= \widetilde{B}^C_{\mathrm{NV}\|} \cdot \left[(1+\kappa) \cdot \cos\left(\frac{\pi}{\tau} \cdot t\right) + \kappa' \sin\left(\frac{\pi}{\tau} \cdot t\right)\right] \end{aligned} \tag{3.16}$$

where κ and κ' are proportional to real and imaginary parts of the complex ac susceptibility of the sample. By integrating Eq 3.3.1 with Eqs. 3.15 and 3.16 substituted in, the normalized x-projection of the final state $X_P = \cos(\varphi_{end}(\delta))$ as a function of the phase delay δ is:

$$X_P(\delta) = \cos\left(\ \Phi_{\mathrm{NV}} \cdot \cos(\delta - \delta_0)\ \right) \tag{3.17}$$

where

$$\begin{aligned} \Phi_{\mathrm{NV}} &= 2\pi\gamma_e \cdot 2/\pi \cdot 8N\tau \cdot |\widetilde{B}^C_{\mathrm{NV}\|}| \sqrt{(1+\kappa)^2 + \kappa'^2} = 32\gamma_e \cdot N\tau \cdot |\widetilde{B}^T_{\mathrm{NV}\|}| \\ \delta_0 &= \arctan\left(\frac{\kappa'}{1+\kappa}\right). \end{aligned} \tag{3.18}$$

We fit our experimental data to Eq 3.17 to determine Φ_{NV}, referred to as the maximum precession angle, and use Eq 3.18 to convert Φ_{NV} to $|\widetilde{B}^T_{\mathrm{NV}\|}|$. If the imaginary component of the ac susceptibility is negligible, as in our case, then $\delta_0 \to 0$ and $\widetilde{B}^T_{\mathrm{NV}\|} \to \widetilde{B}^C_{\mathrm{NV}\|} \cdot (1+\kappa)$. For brevity of notation, $\widetilde{B}^T_{\mathrm{NV}\|}$ is denoted as B^T_{AC} in the main text, etc.

Eq 3.17 oscillates rapidly in δ when Φ_{NV} is large. It is time-consuming to map the whole fringe pattern, so δ is only swept around a small range around $\delta = 0$. However, when Φ_{NV} is large, the $X_P(\delta)$ fringes are almost invariant near $\delta = 0$ when Φ_{NV} differs by $\pm 2n\pi$ where n is a small integer. This suggests that the restricted δ sweep can only determine Φ_{NV} modulo 2π. We illustrate this in Fig 3.2.3 (a) for a simulation of $\Phi_{\mathrm{NV}} = 50.87\pi$ and $\Phi_{\mathrm{NV}} = 52.87\pi$.

However, the change in Φ_{NV} due to the sample response per temperature or magnetic field increment is much smaller than 2π. If we first determine which 2π branch of Φ_{NV} we start in, then we can track these incremental changes continuously by restricting the fit to the appropriate 2π branch.

There are two ways to initially determine the absolute magnitude of Φ_{NV}. The first is to simply measure $X_P(\delta)$ for δ spanning more than $\frac{\pi}{2}$ once prior to a temperature sweep. Fig 3.2.3 (a) shows an exemplary full δ sweep. On this full range, the teal experimental data clearly fits to $\Phi_{\mathrm{NV}} = 50.87\pi$ and not to $\Phi_{\mathrm{NV}} = 52.87\pi$, as is evident in the fast oscillating region highlighted by the dashed rectangle.

The second method is to measure $X_P(\delta)$ at different amplitudes of the coil field, controlled by the voltage output of the ac generator. Far from any flakes, Φ_{NV} should be proportional to the current (voltage) in the coil. As shown in Fig 3.2.3 (b-c), the fringe pattern is sampled for increasing voltages, where for the lowest voltage there is no 2π ambiguity in determining Φ_{NV}. The linear scaling of Φ_{NV} versus voltage shown in Fig 3.2.3 (c) confirms the correct 2π assignments. Hence, by using these methods to determine the initial 2π branch for Φ_{NV}, we can take a restricted set of data around $\delta = 0$ during a sweep, but still track the absolute magnitude of $\widetilde{B}^T_{\mathrm{NV}\|}$ without ambiguity.

3.2.4 quantization in SI unit

By convention the sample response is usually normalized by the easy-axis component of driving field. Since the ac excitation in our setup is produced by a coil which doesn't create a uniformly out-of-plane field, we need to estimate the angle. As sketched in Fig.3.2.4, first $\widetilde{B}^C_{\mathrm{NV}\|}$ is directly measured. Then the angle α between out-of-plane and the direction of external field $\widetilde{H}^C$ is simulated by assuming a 0.5 mm radius coil placed 500 μm above the diamond, thus the total coil field is calculated as $\widetilde{H}^C = \widetilde{B}^C_{\mathrm{NV}\|} \cdot \frac{1}{\cos(\theta+\alpha)}$. Last the easy-axis component is calculated by projecting $\widetilde{H}^C$ onto z axis, which gives $\widetilde{B}^C_z = \widetilde{B}^C_{\mathrm{NV}\|} \cdot \frac{\cos\alpha}{\cos(\theta+\alpha)}$.

The susceptibility is defined as magnetization per unit excitation field per magnetic atom: $\delta M/\delta H$, where $\delta H = \widetilde{B}^C_z$, $\delta M = \widetilde{\sigma}_z/(\rho \cdot t)$. d is the thickness. ρ is the molar density. $\widetilde{\sigma}_z$ is the "AC magnetization density", i.e. the part of magnetization density that is responding to ac excitation. $\widetilde{\sigma}_z$ is proportional to the ac stray field $\widetilde{B}^S_{\mathrm{NV}\|}$ measured outside the flake, assuming a homogeneous response across the whole flake. For example in Fig 4.4.1 (c), by fitting the 26 K curve to Eq 3.5, we find that the closest distance to the flake edge is 0.3 μm and $\widetilde{\sigma}_z = 0.109\ \mu_B{\cdot}\mathrm{nm}^{-2}$. Given its thickness $d = 7$ nm, the molar density of $CrBr_3$ $\rho = 0.0146\ \mathrm{mol{\cdot}cm}^{-3}$, $\alpha = 9°$ and $\widetilde{B}^C_{\mathrm{NV}\|} = 20.99\ \mu$T (Fig.3b)), the ac susceptibility is

calculated as:

$$\begin{aligned}\chi^{\parallel}_{AC}(26\text{ K}) &= \frac{\widetilde{\sigma}_z}{\widetilde{B}^{C}_{\mathrm{NV}\parallel}\cdot\rho\cdot d}\\ &= \frac{0.109\times 9.274\times 10^{-21}\text{ emu}\cdot\text{nm}^{-2}}{20.99\frac{\cos 9^\circ}{\cos(9^\circ+54.736^\circ)}\ \mu\text{T}\times 7\text{ nm}\times 0.0146\text{ mol}\cdot\text{cm}^{-3}}\\ &= 21.1\text{ emu}\cdot\text{mol}^{-1}\cdot\text{Oe}^{-1}\end{aligned}$$

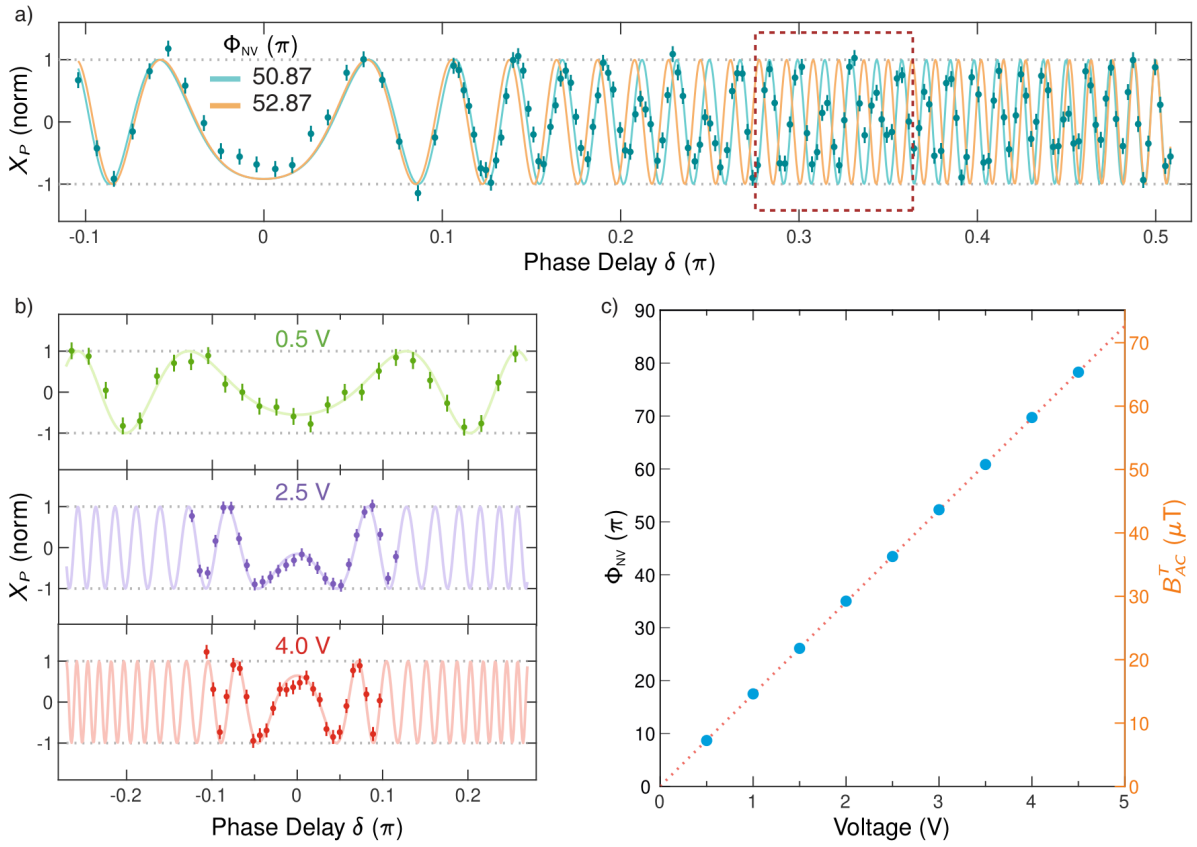

Figure 3.2.3: Determining the absolute magnitude of Φ_{NV}. (a) Full fringe pattern of $X_P(\delta)$ (teal markers) and its best fit curve (teal line). The expected behavior of $X_P(\delta)$ for Φ_{NV} offset by 2π is also plotted (orange line), showing disagreement with the data in the boxed region. (b) $X_P(\delta)$ curves for increasing amplitudes of the coil field (controlled by the voltage applied to the coil). (c) Fitted Φ_{NV} versus coil voltage shows a precise linear dependence and confirms the correct assignment of the 2π branch for each voltage.

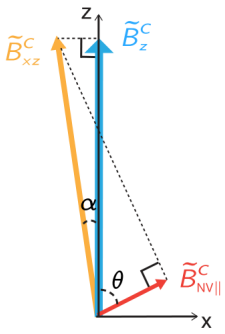

Figure 3.2.4: Illustration of external ac field geometry. $\widetilde{H}^C$ is the vector ac field produced by the coil at the location of the sample. It's projection on the NV center axis $\widetilde{B}^C_{\mathrm{NV}\|}$ is directly measured. The out-of-plane projection $\widetilde{B}^C_z$ is used as normalization to calculate ac susceptibility.

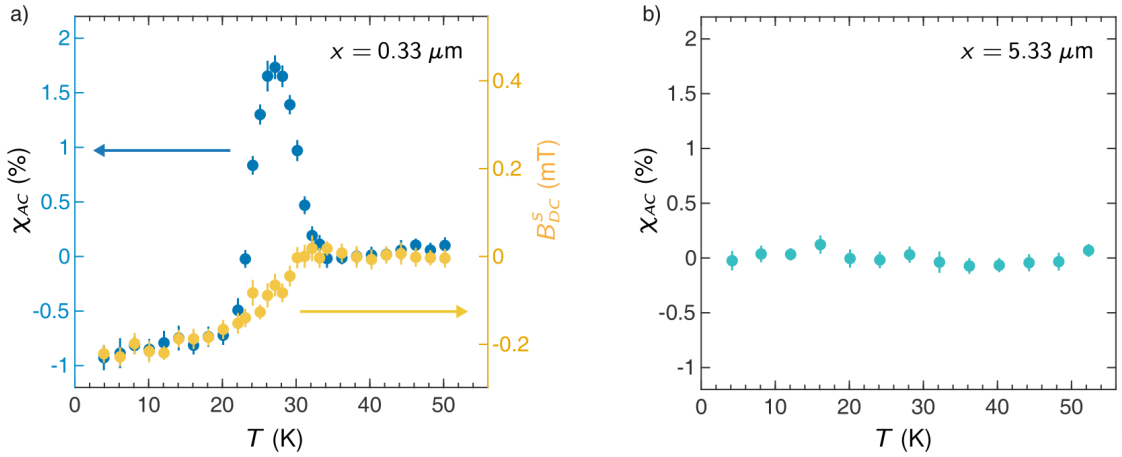

Figure 3.2.5: (a) The shape of the spurious ac background is well described by dc polarization. (b) ac measurement taken far from the flake, representing the bare coil field as a function of temperature. It shows no systematic error related to the drift of the coil.

3.2.5 ac background induced by dc magnetization

The ac signal has a spurious offset below T_c. It shows the same spatial dependence as $B^S_{\mathrm{NV}\perp}(\vec{r})$ described by Eq 3.6, to which the 4 K data in Fig.3e) is fitted. We attribute this effect to the quadratic dependence of NV center energy splitting on $B_{\mathrm{NV}\perp}$.

Larmor precession comes from magnetic-field-induced energy splitting. When sensing ac field, NV centers experience periodic energy splitting, which drives the spin to precess on the equator of the Bloch sphere. How much the precession angle is accumulated is determined by how sensitive the energy levels are to the magnetic field. While the parallel component $B_{\mathrm{NV}\|}$ induces a large linear Zeeman shift, the effect of $B_{\mathrm{NV}\perp}$ is a only a second order perturbation. Explicitly, as one calculates the transition frequency of the $|0\rangle \rightarrow |\pm 1\rangle$

transition with $\epsilon = B_{\mathrm{NV}\perp}/B_{\mathrm{NV}\parallel}$ expanding to the second order[53]:

$$\begin{aligned} f^{\pm} &\doteq D_0 + \frac{3(\gamma_e B_{\mathrm{NV}\parallel})^2}{2D_0}\left(1+\epsilon^2\right)\epsilon^2 \pm \gamma_e B_{\mathrm{NV}\parallel}\cos\epsilon\sqrt{1+\epsilon^2}\sqrt{1+\left(\frac{\gamma_e\epsilon^2}{2D_0}\right)^2} \\ &\doteq D_0 + \frac{3(\gamma_e B_{\mathrm{NV}\parallel}\epsilon)^2}{2D_0} \pm \gamma_e B_{\mathrm{NV}\parallel}\left(1-\frac{1}{2}\epsilon^2\right)\left(1+\frac{1}{2}\epsilon^2\right)\left(1+\frac{1}{2}\left(\frac{\gamma_e\epsilon^2}{2D_0}\right)^2\right) \\ &= D_0 + \frac{3\gamma_e^2}{2D_0}(B_{\mathrm{NV}\perp})^2 \pm \gamma_e B_{\mathrm{NV}\parallel}\left(1-\frac{1}{2}\epsilon^2+\frac{1}{2}\epsilon^2\right) \\ &= D_0 \pm \gamma_e B_{\mathrm{NV}\parallel} + \frac{3\gamma_e^2}{2D_0}(B_{\mathrm{NV}\perp})^2 \end{aligned} \tag{3.19}$$

The maximum precession angle comes from both parts: $\Phi_{\mathrm{NV}} = \Phi_{\mathrm{NV}\parallel} + \Phi_{\mathrm{NV}\perp}$, where

$$\begin{aligned} \Phi_{\mathrm{NV}\parallel} &\propto \frac{\partial f}{\partial B_{\mathrm{NV}\parallel}} = \pm\gamma_e \\ \Phi_{\mathrm{NV}\perp} &\propto \frac{\partial f}{\partial B_{\mathrm{NV}\perp}} = \frac{3\gamma_e^2}{D_0}B_{\mathrm{NV}\perp} \end{aligned} \tag{3.20}$$

such that the parallel contribution is not field dependent, i.e. the maximum precession angle is Φ_0 whatever $B_{\mathrm{NV}\parallel}$ is, as illustrated in Fig.3.2.6a); while the perpendicular contribution has a linear dependence. In Figure 4.4.1, the 4 K data fits to Eq 3.6 while 26 K fits to Eq 3.5. In the geometry of our setup, a flake creates a negative $B^S_{\mathrm{NV}\perp}$ outside the right edge. All of the data presented in this work is done with $|0\rangle \rightarrow |-1\rangle$ subspace, in which such a negative $B^S_{\mathrm{NV}\perp}$ enhances the precession angle as indicated by $+\delta\Phi$ in Fig.3.2.6b). This is also confirmed by Fig.3.2.7 when we deliberately apply a misaligned field. The maximum precession angle is measured as a function of the horizontal position of the permanent magnet. The x-axis is defined such that a larger number means smaller $B_{\mathrm{NV}\perp}$. So when the x-axis is on the larger side of alignment, it has negative $B^S_{\mathrm{NV}\perp}$, same as the stray field of $CrBr_3$ samples. Consistently it gives larger precession angle as indicated by $\Phi_0 + \delta\Phi$ in the figure.

As one fixes the distance to the flake and sweeps temperature, the ratio between perpendicular and parallel stray field is fixed, i.e. $B^S_{\mathrm{NV}\perp}(T)|_{x=x_0} \propto B^S_{\mathrm{NV}\parallel}(T)|_{x=x_0}$, such that the ac spurious offset should have the same shape as dc signal. Fig.3.2.5a) plots the dc data (yellow on the right axis) over ac data (blue on the left axis) measured during the same sweep, showing the perfect match. The yellow line in Fig 4.4.1 (d) is a fit of the dc data

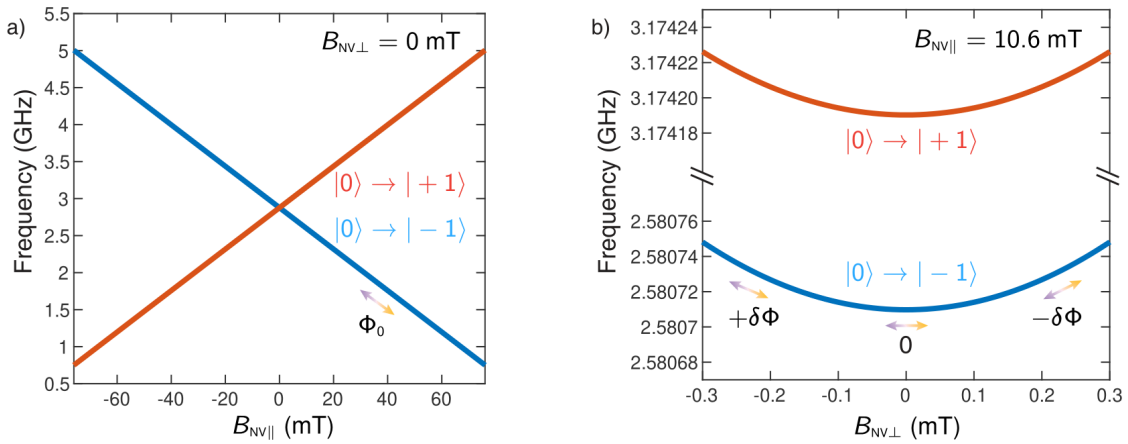

Figure 3.2.6: (a) NV center energy splitting as a function of parallel field with zero misalignment. The maximum precession angle is not field dependent. (b) as a function of perpendicular field with finite parallel component. The shift of maximum precession angle is proportional to $B_{\mathrm{NV}\perp}$.

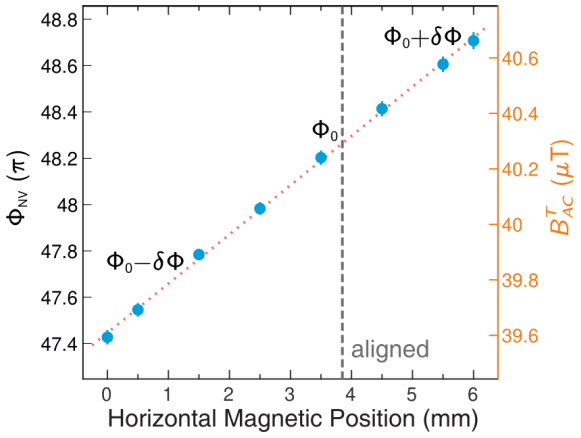

Figure 3.2.7: Maximum precession angle showing dependence on $B_{\mathrm{NV}\perp}$ by pushing the magnet misaligned.

using spin wave model $\sigma_Z(T) \sim S - \frac{k_B T^\beta}{2\pi JS} e^{-\Delta_0/k_B T}$.

3.2.6 spatial distribution of susceptibility source

Our measurement is a single-point or at most a line scan measurement, different from the traditional ac susceptometry where an averaged signal of a large area of the sample is collected. As previously described, we quantify the susceptibility assuming a uniform sheet, but part of the ac susceptibility comes from domain wall displacement which is intrinsically nonuniform. In other words, if our measurement location happens to be near a domain wall, the signal is big; if the measurement location happens to be away from any domain wall, the

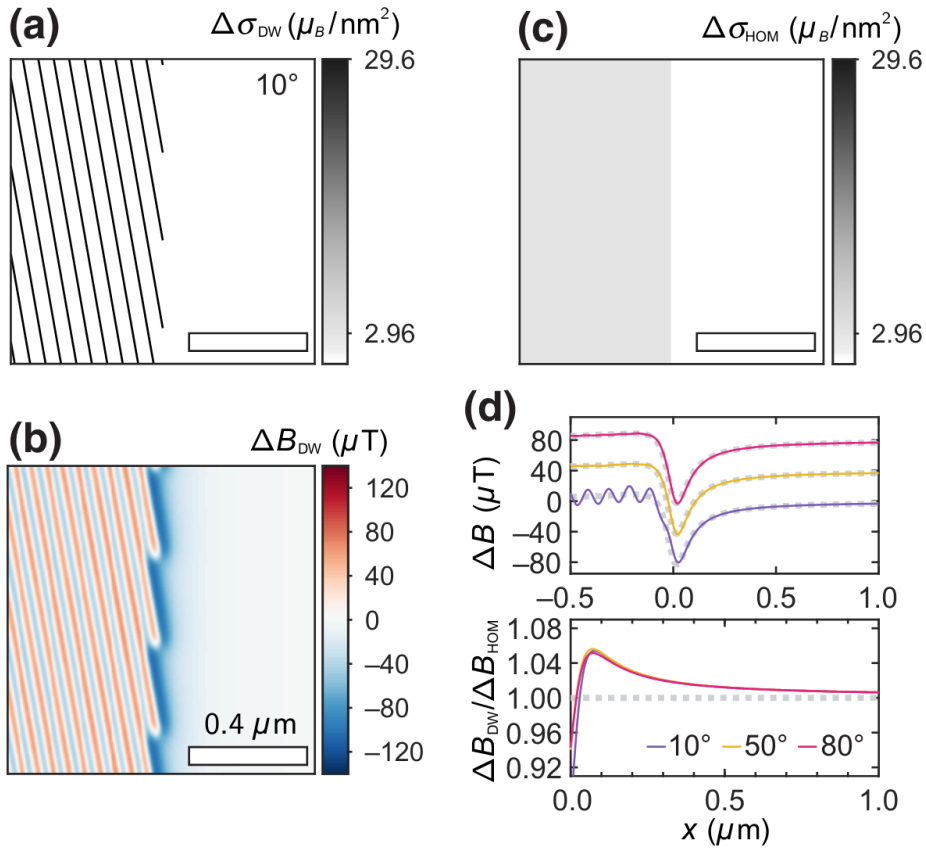

Figure 3.2.8: (a) Spatial distribution of the magnetization change of stripe domains. The domain walls form a 10° angle to the edge of the flake with spacing of 100 nm, and are assumed to move by 10 nm under an excitation field. (b) Simulated stray field of stripe domains. (c) Spatial distribution of a homogeneous magnetization change, with the density equivalent to spatial average of the stripe configuration. (d) Top: linecuts of the stray field versus the distance perpendicular to the flake's edge. Solid lines of different colors mean different angles of the stripes with respect to the flake edge. The dashed lines are of the homogeneous configuration. The linecuts are offset for clarity and are Gaussian-averaged in the y direction, parallel to the flake, over our optical beam size. Bottom: ratio of the stray field of the stripe configurations to that of uniform distribution. The ratio approaches one as x increases, independent of the exact spatial distribution.

signal is small. However an ideal ac susceptometry should present an averaged quantification of the whole material, regardless of where we park our probe. As a matter of fact, we observe the ac susceptibility line scan shows a faster spatial decay than the dc signal. As shown in Fig 4.4.1 (c), the dashed blue line does not perfectly fit the blue data, suggesting a nonuniform ac signal. This brings up the question of how well our number represent the overall ac susceptibility.

We find that the stray field outside the flake provides a convergent estimate for the spatially averaged magnetization change when the individual sources of susceptibility are

relatively dense on the length scale of the distance between the measurement location and the flake edge. Assuming domain wall movements of 100 nm width [54], the ac susceptibility measured at a distance $\sim 1\mu$m away from the flake edge produces a good estimation of the average value across the flake, as the simulation shows in Fig 3.2.8.

3.3 pump-probe microscopy for photo-generated phenomena

The dynamical decoupling sequence extends the coherence time T_2 of the NV superposition state and allows only ac fields synchronized to the π pulse spacing to affect the NV precession, while blocking the influence of wideband magnetic noise. As such we can lock-in the signal of resonant frequencies. Previously it was used to detect subtle environmental signals, such as nuclear magnetic resonance [55, 56] and electron paramagnetic resonance [57]. In the ac susceptometry it is the total ac magnetic field that the DD sequence locks in. In this chapter we discuss photo-generated transient magnetism or photocurrent [52, 58].

3.3.1 pump-probe protocol

one-beam microscopy The 515 nm green laser is used for both initialization and readout of NV centers, and also photo-excitation of 2d material. An example sequence is simply a Hahn sequence as shown in Fig 3.3.1 (b) . The π pulse negates the modulation, such that the accumulated phase measured as $\Phi = \arctan\left(\frac{Y_P}{X_P}\right)$ is proportional to the difference between the integral of stray field over the first τ and the second τ.

two-beam microscopy, single excitation The 515 nm green laser is to illuminate ensemble NV centers and scanned across the diamond substrate; the other beam (illustrated as red) is used for photo-excitation of 2d material and kept fixed during mapping measurement. The two beams are independently steered. The sensing sequence is shown in Fig 3.3.1 (c). The pump pulse can be delayed by a duration that is long enough for the transient field excited by the green pulse to fade away after the initializing pulse, in case the green laser has an effect on the material. Because NV centers have T_1 on the order of ms, a delay on the order smaller than ms has virtually no effect on the NV initialization. Microwave pulses of duration t_p are applied waiting t_d after the pump pulse.

two-beam microscopy, multiple excitation In the case that the photo-excited phenomenon quickly fades away after the excitation is turned off (sub μs scale), or the signal is too small and requires repetitions of integration, multiple photo excitation can be used in

sync with the DD sequence. An example sequence is illustrated in Fig 3.3.1 (e). The phase to magnetic field conversion is similar to the ac susceptometry introduced in the previous chapter, other than that the $\widetilde{B}^{T}_{\mathrm{NV}\parallel}(t)$ in Eq is no longer sinusoidal but square waves.

Photo-current and photo-magnetization are the two most common photo-physics that can be measured with the pump-probe microscopy. As illustrated in Fig 3.3.1 (a), the pump beam (red beam) stimulates the excitons, inducing the transient enhancement of magnetic moments (white and red spheres with arrows; red intensity indicates the magnetization magnitude) in the layered antiferromagnet; as illustrated in Fig 3.3.1 (b), the pump beam excites photocurrent, of which the flow direction and intensity is spatially resolved with NV mapping. In the following section, we focus on the case of transient magnetism measured with the pump-probe technique.

3.3.2 conversion between the accumulated phase to B

The conversion between M and B is introduced in the Ch 3.1.1. Here we present the conversion between B and Φ. By implementing the conversion first from experimentally measured Φ to B, and then from B to M, one can reconstruct the spatial distribution of photo-generated transient magnetization. Given the Hahn measurement sequence:

$$\text{NV Initialization} \xrightarrow{t_w} \text{Pump } CrCl_3 \xrightarrow{t_d} \left(\frac{\pi}{2}\right)_x \xrightarrow{\tau} \pi_y \xrightarrow{\tau} \left(\frac{\pi}{2}\right)_{\text{proj}} - \text{NV Probe}$$

where t_w is a wait-time used in the dual-beam experiments to allow the incidental effect of the green NV probe beam to decay. At a particular location, $\Delta B_{\mathrm{NV}}(t)$ decays with time t after the end of the pump pulse. Thus for the Hahn sequence, the phase Φ we measure is a modulated integral of the Larmor precession, with the phase acquired prior to the π-pulse being inverted in the final total:

$$\begin{aligned}\Phi(x,y,2\tau,t_d) &= -\int_{t_d}^{t_d+\tau} 2\pi\gamma_e \cdot \Delta B_{\mathrm{NV}}(x,y,t)\ \mathrm{d}t + \int_{t_d+\tau}^{t_d+2\tau} 2\pi\gamma_e \cdot \Delta B_{\mathrm{NV}}(x,y,t)\ \mathrm{d}t \\ &= 2\pi\gamma_e \cdot \Delta B_{\mathrm{NV}}(x,y,0) \cdot \left(\int_{t_d+\tau}^{t_d+2\tau} e^{-\left(\frac{t}{\tau_m}\right)^{\alpha}}\ \mathrm{d}t - \int_{t_d}^{t_d+\tau} e^{-\left(\frac{t}{\tau_m}\right)^{\alpha}}\ \mathrm{d}t\right)\end{aligned} \tag{3.21}$$

where $+2\pi\gamma_e = +2\pi\cdot$ 28 MHz/mT is the gyromagnetic ratio for the $|m_s = -1\rangle$ state above the NV ground-state anti-crossing. $\Delta B_{\mathrm{NV}}(x,y,0)$ is the stray field at $t = 0$, which

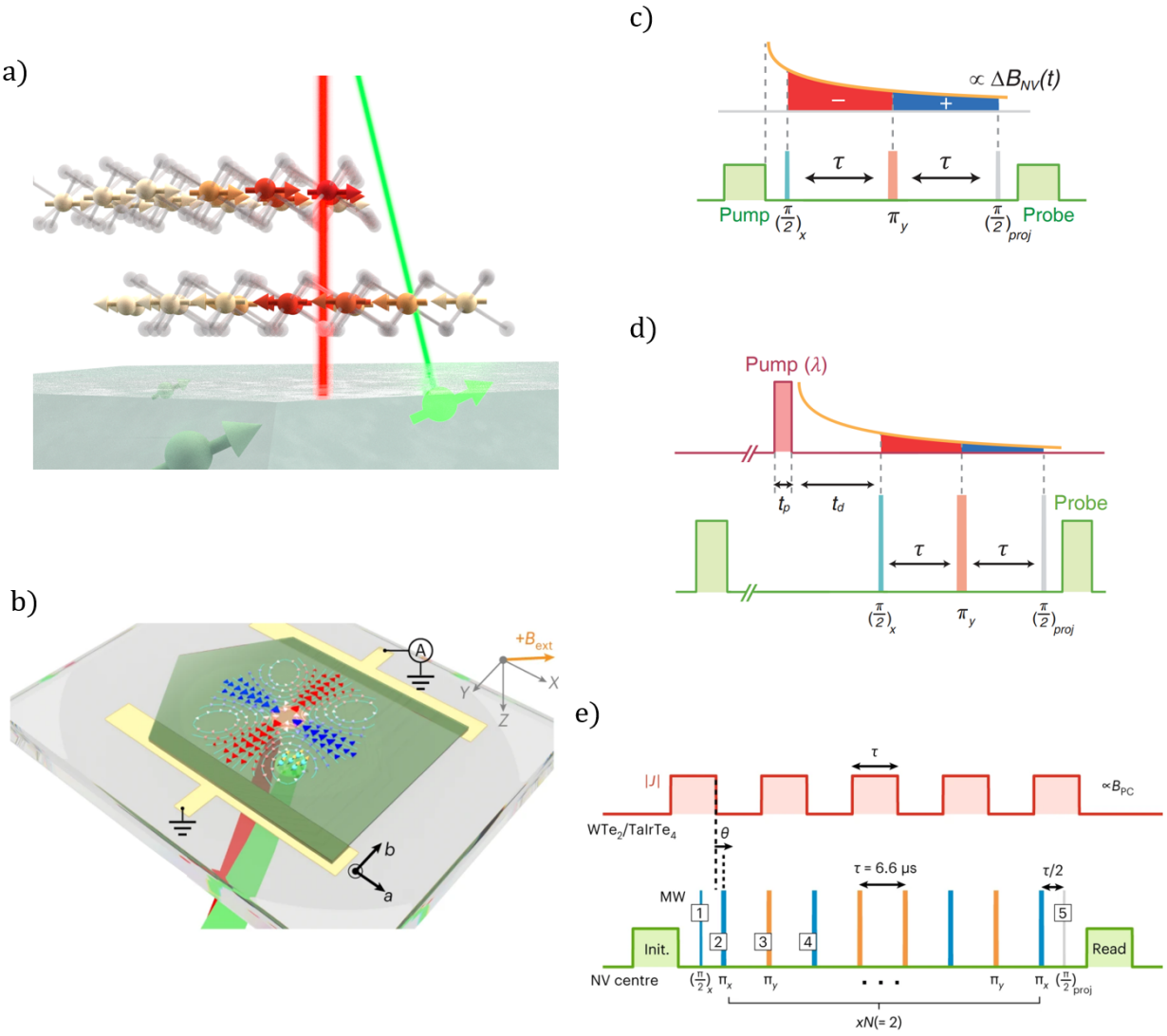

Figure 3.3.1: Illustration of pump-probe detection of photo-generated magnetism (a) and current (b). Measurement sequence of one-beam mapping (c), two-beam single-excitation mapping (d) and two-beam multiple-excitation mapping.

can be calculated using Eq 3.3 with $\Delta\vec{M}(x, y, t = 0) = \vec{M}_0 \exp\left(-\frac{x^2+y^2}{2\sigma^2}\right)$.

The sum of the time integrals in parentheses is a strictly negative quantity; hence, we can immediately deduce that $\Phi(x, y, 2\tau, t_d) \propto -\Delta B_{\mathrm{NV}}(x, y, 0)$, or more simply stated, the spatial pattern for $\Phi(x, y)$ is the same as for $-\Delta B_{\mathrm{NV}}(x, y)$. A single measurement of $\Phi(x, y, 2\tau, t_d)$ is not able to constrain the three unknown factors ($\Delta B_{\mathrm{NV}}(x, y, 0)$, τ_m, α), but a set of $\Phi(x, y, 2\tau, t_d)$ for different 2τ and t_d can be jointly fit to determine the free parameters.

3.3.3 confirmation of the sign of M

The interpretation of our experiment crucially depends on the sign of ΔM, as a decrease in magnetization could potentially be trivially explained by laser-induced thermal demagnetization. Hence, we have been careful to rigorously check our conclusion.

Experimental check on the sign of Φ for a simulated time-varying stray field $\Delta B_{NV}(t)$ Here we use an in-plane magnetized 2d material such as $CrCl_3$ as an example. As shown in the simulations of Fig 3.1.1 (a), a stronger in-plane magnetization along the $+x$-axis leads to more negative ΔB_{NV} along the NV center axis right underneath the magnetization. Therefore, during the Hahn echo sequence, the transient magnetic field (right underneath the pump beam) is expected to be more negative during the first half of the echo than in the second half, since the optically-induced magnetization change decays to zero. Thus we should verify that the sign of Φ measured under identical conditions is positive for a controlled signal field that is more negative during the first half of the Hahn echo than during the second half.

To do this, we add another current signal through a diplexer to the same coil that is used to apply the microwave pulses. This calibration experiment is shown in Fig 3.3.2, where $B_{ext} = 141$ mT. For $B_{ext} > 102.8$ mT (NV center anti-crossing), a positive shift in ODMR frequency corresponds to a positive sign of the field along the NV center axis. In Fig 3.3.2 (b), we see that a positive dc voltage creates a positive dc magnetic field at the NV location, as revealed by the pulsed ODMR measurements.

Intuitive Bloch sphere picture of NV precession To visualize the NV center precession, we look at the Hamiltonian of the NV center in the rotating wave approximation. Suppose the NV center is under a microwave and dc magnetic field. Here, the dc field includes ΔB, the stray field excited by pump laser, which changes over a timescale of $\sim$10 μs and is essentially static compared to the microwave frequency of $\sim$GHz. The equation below is written in the coordinate of NV center, i.e. $\hat{z}$ is along $\mathrm{NV}_{\parallel}$, $\hat{x}$ is along $\mathrm{NV}_{\perp}$. In the microwave frame with the rotating wave approximation (RWA), the Hamiltonian is

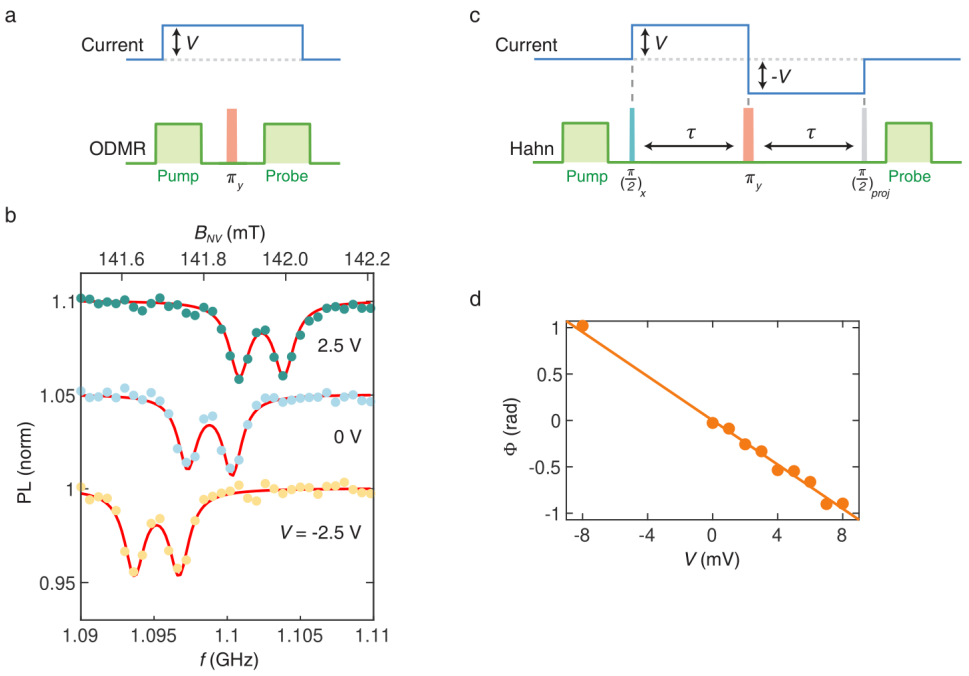

Figure 3.3.2: ODMR (a,b) and Hahn (c,d) measurement with simulated magnetic fields applied through the coil. The ODMR measurement indicate a positive voltage creates a positive dc field ΔB_{NV} along the NV center axis. Thus, by applying a square wave as shown in c), a time-varying magnetic signal that is more positive (negative) during the first half of the Hahn echo than the second half is created by the V = +8 (-8) mV data point in d) and produces a negative (positive) precession angle Φ. This proves that a positive precession angle Φ is associated with a -B_{NV} due to an *enhancement* of the in-plane magnetization.

$$H_{\text{rwa}} = \frac{\delta\omega}{2}\sigma_z + \frac{\omega_{\text{rf}}}{2}\sigma_x \tag{3.22}$$

where for the $|m_s = 0\rangle$ and $|m_s = -1\rangle$ basis states

$$\begin{aligned} \delta\omega &= |f_0 - \gamma(B_{\text{ext}} + \Delta B)| - \omega \\ \omega_{\text{rf}} &= \gamma B_{\text{rf}} \end{aligned} \tag{3.23}$$

Here, f_0 is the zero-field splitting. During free evolution, the σ_x component is negligible since the microwave is off. Due to the absolute value, the sign of the σ_z component depends on whether $B_{\text{ext}} + \Delta B$ is below or above the NV center anti-crossing field ($f_0/\gamma \sim 102.8$ mT). The microwave frequency ω is set on resonance to match B_{ext}, *i.e.* $\omega = |f_0 - \gamma B_{\text{ext}}|$. Hence, below the anti-crossing, $\delta\omega = -\gamma\Delta B$; above the anti-crossing, $\delta\omega = +\gamma\Delta B$.

Most of our Hahn echo data are taken above the crossing field. Under this circumstance, $\delta\omega > 0$ for $\Delta B > 0$, so the superposition state undergoes counterclockwise evolution on the

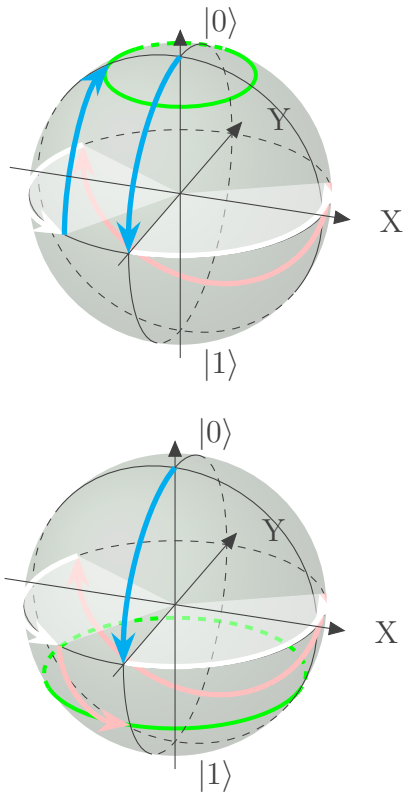

Figure 3.3.3: Evolution of the superposition state of the NV center on a Bloch sphere during the Hahn sequence with a positive detuning $\delta\omega$. The final $\pi/2$ readout pulse is either an X-pulse (left) or Y-pulse (right). The trajectory during X-pulses is drawn as blue arrows, Y-pulses as pink arrows, and the free evolution during the interval between the pulses as white arrows. Because ΔB is decaying, the evolution angle is larger during the first half of the echo (right white shaded region on each sphere) than in the second half (left white shaded region). The normalized NV center photoluminescence reads out positive (negative) if the polarization (green circle) of the state after the projection pulse is above (below) the equator.

Bloch sphere equator (by right-hand rule) during the free evolution intervals of the Hahn echo sequence as visualized in Fig. 3.3.3. With $\delta\omega > 0$ and $\Delta B \to 0$ during the echo, the counterclockwise precession is larger during the first half before the π-pulse than after the π-pulse. The phase acquired in the first half is inverted by the π-pulse. Hence, the net accumulated phase Φ is negative, and the X-projection of the final evolved state reads out positive for small angles; the Y-projection reads out negative. Alternatively, if the field is below the crossing field, then $\delta\omega < 0$ for $\Delta B > 0$ will make the superposition state evolve clockwise during the free evolution intervals between the microwave pulses. In that case, the final X-projection for small angles still reads out positive, but Y-projection also reads out positive, giving a positive phase Φ.

Theoretically expected signs for various quantities after a Hahn echo evolution under a decaying, positive $\Delta B(t)$

B_{ext}	$\delta\omega$	Free Evolution	$\langle X \rangle_{final}$	$\langle Y \rangle_{final}$	Φ
$B_{\text{ext}} > 102.8$ mT	$+$	counterclockwise	$+$	$-$	$-$
$B_{\text{ext}} < 102.8$ mT	$-$	clockwise	$+$	$+$	$+$

Chapter 4
ac Susceptometry of CrBr3

The work in this chapter and Ch 3.2 is supported by NSF ECCS-2041779. The findings and conclusions do not necessarily reflect the view of the funding agency.

4.1 introduction

The magnetism in low dimensions is theoretically forbidden by Mermin-Wagner Theorem, unless anisotropy arises. In spin rotational invariant systems, long range order is destroyed below three-dimension because of thermally excited magnons. The discovery of 2d vdW magnets completes the missing part of the 2d vdW realm. Since the first exfoliation of graphene using the Scotch tape technique, research in exfoliated 2d materials has been thriving. 2d vdW materials have strong in-layer bonds and weak interlayer coupling, so individual or few-layer materials can be isolated and re-assembled. 2d materials are in general interesting because they possess a wide range of properties distinctive from their bulk counterparts, including the crystal structure or the band structure, leading to intriguing electronic or photonic properties and unconventional couplings. Moreover, 2d materials are more flexible in parameter tuning, free of substrate effect, because of stacking versatility. The angstrom level proximity havs provided modulation power not accessible in the bulk regime. After the discovery of magnetic 2d materials, they are studied both as themselves and also stacked onto other 2d materials, for example to provide strong magnetic field to lift valley degeneracy [59].

Atomically thin magnets are generally challenging to characterize [60–62]. The magnetic moments of a micron-sized exfoliated monolayer (approximately 10^{-11} emu) lie below the sensitivity of commercial superconducting quantum interference device (SQUID) [63] (approximately 10^{-8} emu). Previously only indirect probing methods were applied, such as fluorescence [64, 65], the magneto-optical Kerr effect [66–69] or the integration into electrical devices [70–72]. The limitations of these probing methods are that they don't provide sub-micron resolution, or they lack quantitative evaluation about the magnetization [73–75]. NV magnetometry in the dc range have been developed [37, 38, 76, 77]. With a diamond tips comprising a single NV center, or widefield ensemble NV substrate brought to nanometer scale proximity, 2d magnets can be quantitatively imaged down to monolayer limit with nanometer resolution, showing even-odd effect of interlayer antiferromagnetism.

However the dynamical properties of these 2d magnets have not been quantitatively studied. It is crucial to measure the ac susceptibility of 2d magnets to unveil their properties,

such as phase transition, relaxation and domain wall movements. The ac susceptibility is fundamentally informative in systems such as antiferromagnets, spin glasses and ensembles of single-molecule magnets [46, 78]. For ferromagnets, the divergence of ac susceptibility near paramagnetic transition with a critical exponent γ characterizes the universality class of underlying interactions [79], while below T_C the ac susceptibility characterizes magnetization rotation, domain wall motion, superparamagnetism, and the interactions of these processes with defects, strain, and external dc field [80]. The NV works as a multi-modal probe given its great sensitivity in wide range of frequencies and stability in versatile environments. Therefore it is natural to devise an ac sensing technique for the micro-scale magnets. Through this work the formation, mobility, and consolidation of single domain walls in $CrBr_3$ below T_C was illuminated by our ac susceptometry, providing information on the potential for domain-based memory and logic devices [81–83].

4.2 $CrBr_3$ a ferromagnetic 2d material

Chromium trihalides CrX_3 (X = F, Cl, Br and I) are indirect bandgap magnetic semiconductors. Different from CrI_3 and $CrCl_3$, which have opposite spin alignments across neighbour layers, $CrBr_3$ has ferromagnetic inter-layer coupling, therefore the ac signal is larger and provides a great prototype for 2d ac susceptibility sensing. Bulk $CrBr_3$ is a ferromagnet with Curie temperature 37 K.

The lattice structure of $CrBr_3$ is shown in Figure 4.2.1. In each layer of $CrBr_3$, the chromium ions form the honeycomb lattice. Each chromium ions is surrounded by six iodine atoms, arranged in a corner-sharing octahedra. The six iodine atoms form the top and the bottom sublayer, each sublayer having three iodine, forming two triangles facing the opposite directions in the top view. R-stacking means that in all chromium trihalide layer, the triangles of the top sublayers point in the same direction, and those of the bottom sublayers point in the same direction. R-stacking can be further divided into monoclinic and rhombohedral stacking, depending on whether the system has two mirror symmetry planes or three-fold rotation symmetry. While in H-stacking, the orientation of triangles in the top or the bottom sublayers switch the direction between neighbouring layers. Both bulk and exfoliated $CrBr_3$ have H-stacking. R-stacking $CrBr_3$ can be grown with molecular beam epitaxy (MBE) [84].

The electron configuration of a charge-neutral chromium atom is $[Ar]4s^1 3d^5$. With six bromine atoms around, the chromium ion has three positive charges and the electron configuration is $[Ar]4s^0 3d^3$. According to Hund's rule, the three d-electrons are filled in such a

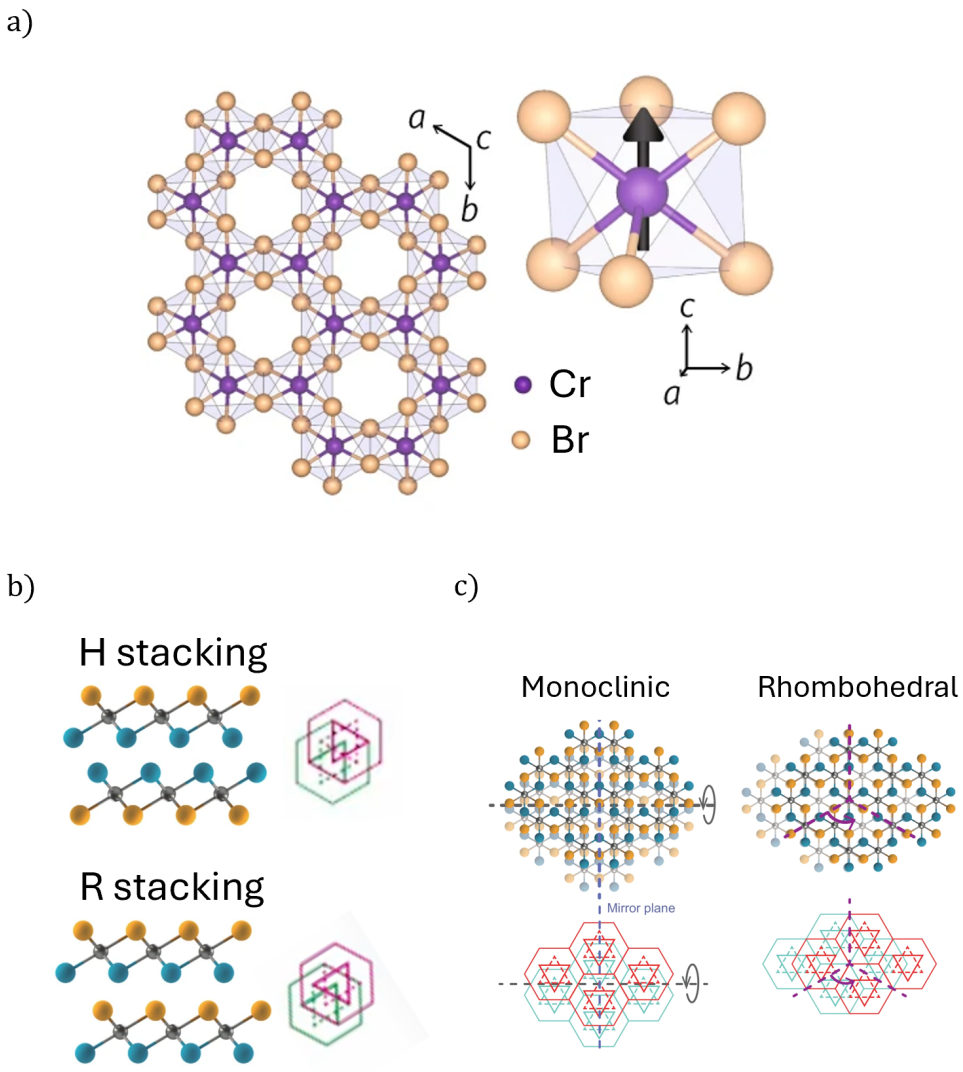

Figure 4.2.1: Chromium trihalides lattice structures. Figures adapted from Refs [64, 84].

way that each chromium atom has an out-of-plane magnetic moment of $3\mu_B$. The density of magnetic momentum is 14.7 μ_B/nm^2.

4.3 dc field sensing of magnetic hysteresis

In this work we use an ensemble NV substrate beneath the ultrathin $CrBr_3$ [85, 86] exfoliated without hBN encapsulation. By parking the optical spot outside the flake, we characterize the magnetic hysteresis of $CrBr_3$ of different thickness. We observed that the 515 nm laser could easily burn $CrBr_3$ with laser power even as low as a few tens of μW. It is also advantageous to measure near the edge because the stray field is large, as illustrated in Figure 4.3.1 (a).

The behavior of the hysteresis is dependent on the layer number and the temperature. In this work the external bias field B^E_{DC} is applied along the NV direction. The stray field B^S_{DC} is also the projection along the NV axis. The in-plane component of magnetic moments can be neglected in the range of bias field used in this work, as $CrBr_3$ has strong uniaxial anisotropy that forces magnetization to the out-of-plane direction [87]. As we can see, for Flake A the hysteresis tends to be flat and square, showing only one or two jumps when the external field is swept at cold temperatures. The hysteresis displays full remanence and a large coercive field. While for Flake B, which has a similar thickness to Flake A, the hysteresis tends to show continuous stray field change, comprising a few more jumps of smaller amplitudes. These are called discrete Barkhausen jumps (gray arrows), corresponding to the hopping of individual domain walls between different pinning sites. When the temperature rises, similar continuous magnetism changes are observed in Flake A, and also the saturation stray field is decreased. These observations indicate that there are intrinsically variations across flakes. Some flakes tend to form smaller domains under the same field and temperature. The metastable domain structures and magnetization reversal process in intermediate thickness CrBr3 flakes (9–10 layers) are extremely sensitive to details of the local microstructure, including strain and defects. The same behavior is also seen in NV scanning works [38]. This is possibly because intermediate thickness flakes could have defects in some batches, inducing pinning sites or some local areas with modified exchange coupling [88].

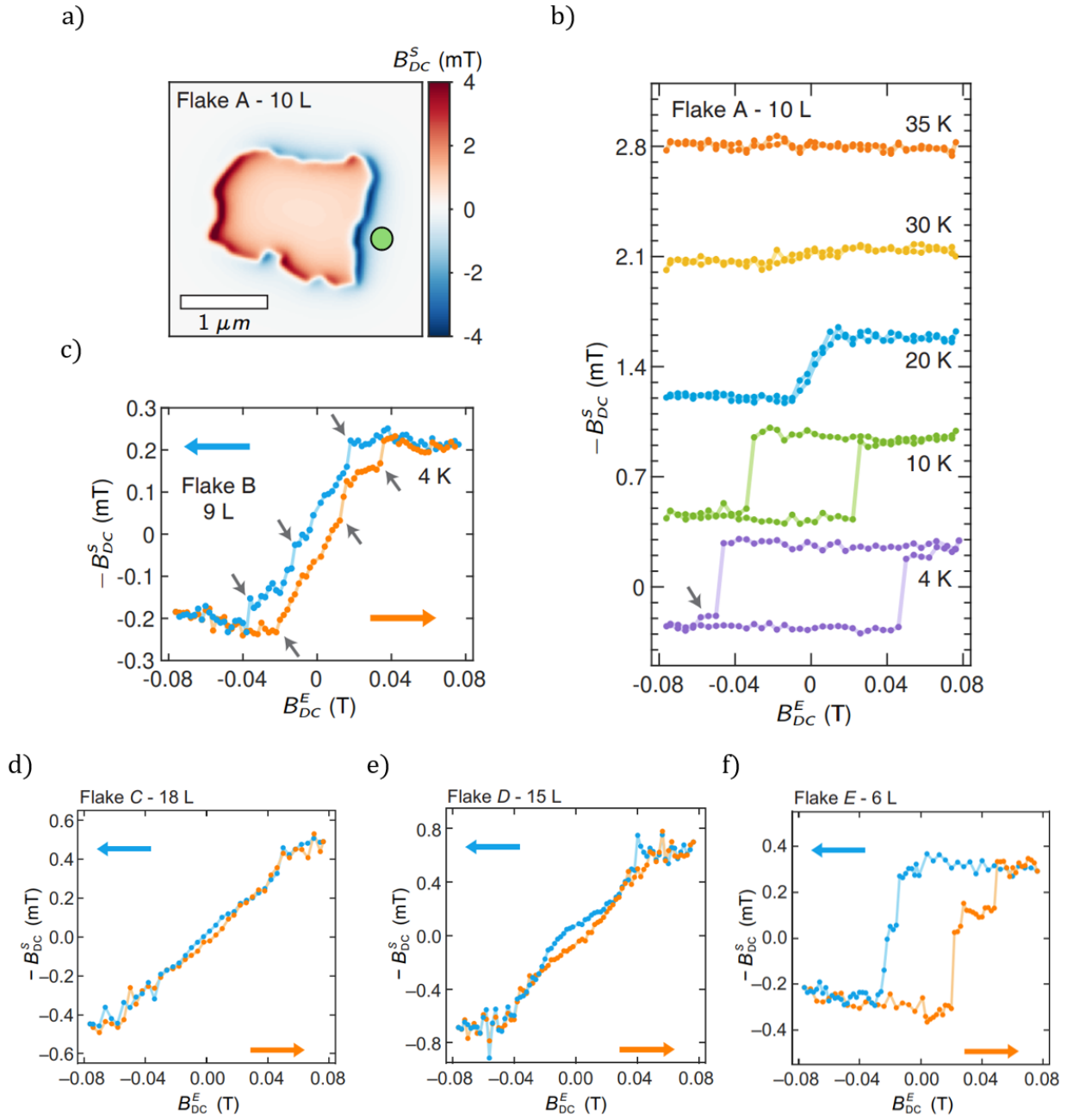

Figure 4.3.1: (a) Simulated map for Flake A (ten layers thick) for the component of the flake's stray field parallel to the NV center axis. Measurements are primarily taken outside the flake's right edge (green dot) and are referenced to the background signal far away from the flake. (b) Temperature-dependent hysteresis curves for Flake A (ten layers thick), which display rectangular hysteresis indicating minimal pinning of domain walls once nucleated. (c) Magnetic hysteresis curve for Flake B (nine layers thick), where the magnetization M slowly reverses due to domain wall pinning. Discrete Barkhausen jumps are marked by the grey arrows. (d-f) Magnetic hysteresis curve for 18-layer, 15-layer and 6-layer.

4.4 ac field sensing of susceptibility

As introduced in Ch 3.2, the ac susceptometry uses a coil to produce both microwave pulses for manipulating NV centers and ac magnetic field to excite the magnetization response in the material. Then microwave pulses construct the DD sequence which extends the NV center coherence time by filtering the noise of unsynchronized frequency, while amplifying the signal of synchronized frequency. The total ac signal comprising both the external applied field B^E_{AC} and the stray field from flake B^S_{AC}. Figure 4.4.1 (a-b) illustrate the total ac field at the nearest spot outside the flake. The quantification of total ac field is by fitting the curve to Eq. 3.17. The difference of the total ac magnetic field amplitude between 27 K and 50 K indicates the contribution from the $CrBr_3$ sample.

In order to get the pure stray field signal B^S_{AC}, the background signal of external ac field is subtracted. The background signal represents the B^E_{AC} created by the coil, determined by doing a linear fit on the ac magnetic field measured as a function of the distance from the flake edge at 50 K. Figure 4.4.1 (c) illustrates the spatial dependence of the stray field after background subtraction, being zero at 50 K and negative at 26 K. The 'unexpected' positive signal at 4 K is an artifact signal induced by the flake's dc stray field arising on the perpendicular axis of NV center as described in Ch 3.2.5. The 26 K data is fitted to the parallel component of stray field Eq. 3.5 (orange solid), and the 4 K data is fitted to the perpendicular component of the stray field Eq. 3.6 (blue dashed).

The artifact signal from the perpendicular dc component is subtracted out in the temperature dependence. Figure 4.4.1 (d) plots the ac susceptibility in two different definitions. The left axis is $-B^S_{ac}/B^E_{ac}$ with a unit of %. The right axis is defined as magnetization per unit excitation field per magnetic atom with a unit of emu$\cdot$ mol$^{-1}\cdot$Oe^{-1}. The yellow line is a fit proportional to the dc stray field measured simultaneously with the ac field, and is scaled such that it overlaps the ac field at low temperatures (< 20 K). The true signal for the field warming (FW) cycle at 10.6 mT is plotted in the inset, with only a divergent peak around the Curie temperature.

With the calibrations we can measure the ac susceptibility with varying field and flake thickness. Compared with FW at 10.6 mT, FC at the same or lower field shows overlapping behavior at the paramagnetic transition, but possesses one more broad peak in the ferromagnetic phase known as Hopkins peak [89], as illustrated in Figure 4.4.2. The behavior in the ferrormagnetic phase is suppressed by increasing field, accompanied by an increase of dc saturation magnetization. We attribute the initial rounding and decrease of χ_{ac} to the formation of the domain structure, which impedes the coherent magnetization rotation

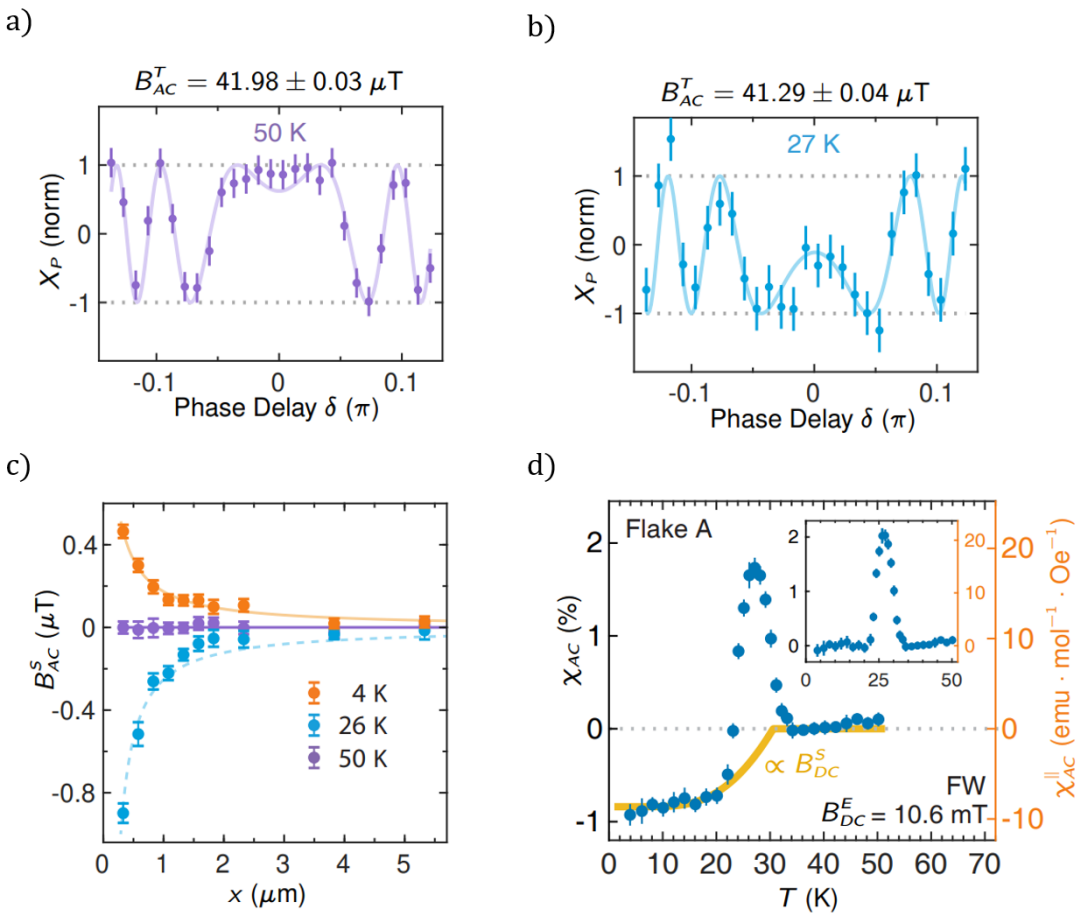

Figure 4.4.1: (a-b) The total ac field for Flake A is determined from the fringe pattern using the ac sensing protocl comprising an XY8-N2 sequence of $\tau = 2.1$ μs (238 kHz) with a final X_P projection. The fringes are induced by the integration of NV center precession of the superposition state. The data are taken at a dc bias field of 10.6 mT. (c) Linecut of the ac stray field away from Flake A's right edge. A linear background is determined from the 50 K data and subtracted from all. (d) Temperature dependence of uncorrected (main) and corrected (inset) ac susceptibility for Flake A. The data is collected after cooling with a bias field of 10.6 mT and during warming at the same field.

relative to the paramagnetic state. We attribute the two peaks to different microscopic behaviors of the magnetism. The peak near the transition temperature indicates the formation of small batch domains involving magnetization rotation. Monte Carlo simulations [90, 91] indicate that incipient domain-like patches begin to form a few kelvin above Tc, with the magnetic axes of the domains initially isotropically distributed. The second peak existing in the ferromagnetic phase indicates the growth and expansion of aligned magnetic domains, involving domain wall movements and nucleation.

For Flake C, the bulk-like flake, the temperature dependence of the ac susceptibility shows a different behavior at low field. The susceptibility demonstrates more than two local maximums and does not have an obvious trend of decreasing at low temperatures. This is probably becuase of our probe is rather local than global. As we park our measurement spot outside the flake, the measurement characterizes the averaged signal only when the domain size is either tiny or big. For example, with Flake A where the density of pinning sites is low, the domain size quickly switches from granular to a single patch when cooling through the transition temperature, therefore our ac protocol always measures an averaged signal that shows two peaks. In contrast, with bulk-like Flake C, 2 mT is not high enough to polarize the sample to large domains as illustrated by the hysteresis and the dc cooling curve. Electron microscopy observes periodic stripe-like domains in bulk CrBr3 with widths of approximately 100 nm [54], consistent with significantly reduced stray fields even when measured at our near-field location. Therefore the probe is sensitive to a few domain wall nearby, of which the bulging and contracting may fluctuate at various temperatures. As a result the measurement is too local to represent a statistical average of global susceptibility and displays several peaks.

Quantitatively, the peak value of χ_{ac} [approximately 7 emu·(mol Oe)$^{-1}$] determined for Flake C by NV magnetometry is close to that measured for bulk CrI_3 using a SQUID magnetometer [approximately 6 emu·(mol Oe)$^{-1}$] [92]. The dc magnetization during the subsequent FW in strong field is also plotted and fitted to $M(T) \propto (1 - T/T_c)^{\beta}$, with $\beta = 0.38 \pm 0.02$ and $T_C = 30.5$ K, in close agreement with prior works that found $\beta \approx 0.4$ for both bulk [93] and monolayer [68] $CrBr_3$.

Figure 4.5.1 presents the frequency dependence of ac susceptibility for Flake A. The frequency variation is realized by changing the excitation current going through the coil, at the same time of changing τ and the repetition of the microwave XY8 sequence. The frequency dependence is:

$$\chi(\omega) = \frac{\omega_0}{1 - (\omega/\omega_0)^2 + i(\omega/\omega_c)} \tag{4.1}$$

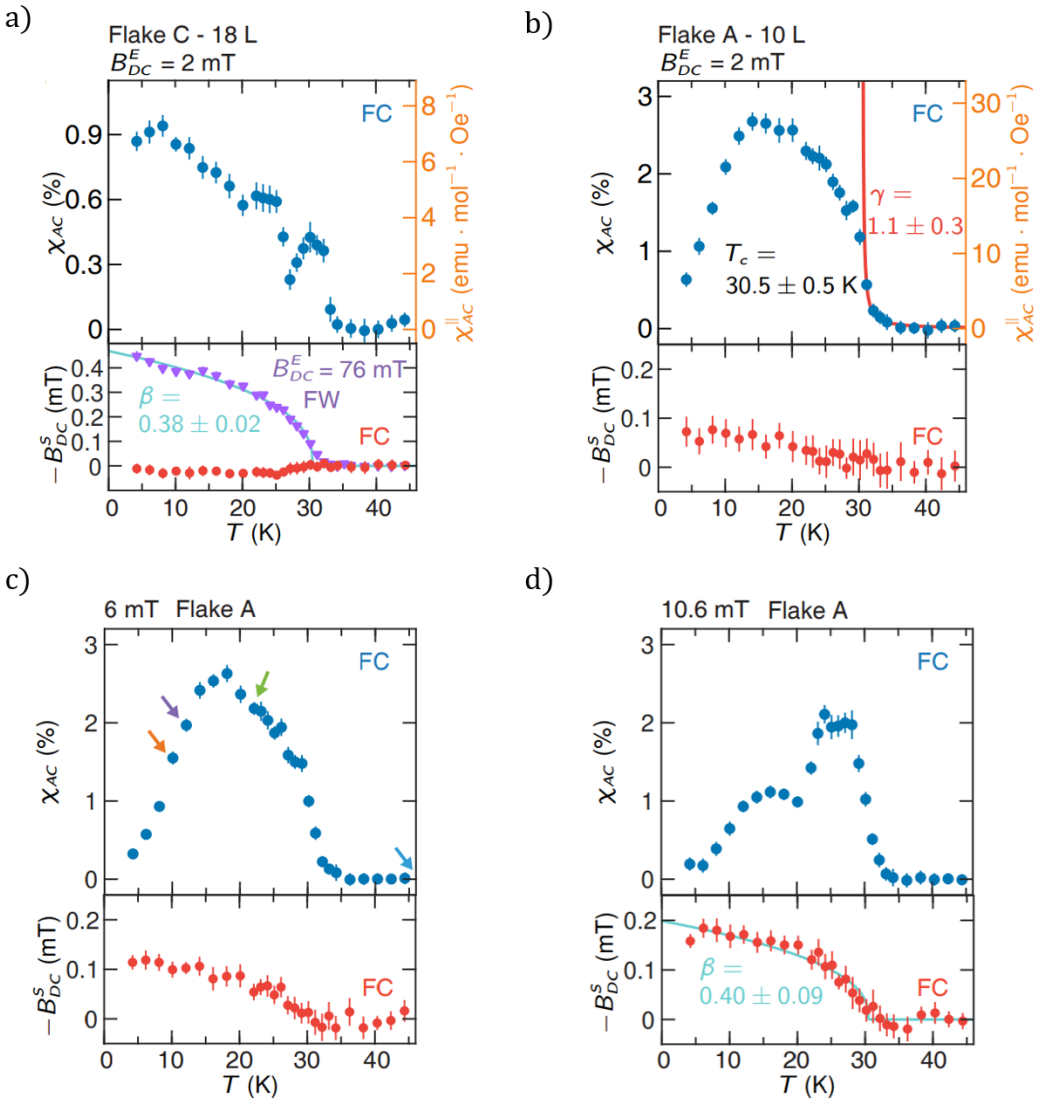

Figure 4.4.2: (a) Temperature dependence of ac susceptibility (blue) and dc magnetization (red) for bulk-like Flake C (18 layers) during FC at low bias field. The magnetization remains nearly zero, indicating a finely fragmented domain structure. The magnetization during FW at a high bias field (purple) is also plotted for comparison. It shows a critical scaling $M(T) \propto (1T/Tc)^{\beta}$ with $\beta = 0.38 \pm 0.02$. (b)–(d) Temperature dependence of ac susceptibility (blue) and dc magnetization (red) for Flake A (10 layers) during FC at various bias fields. Flake A, the flake with square hysteresis, has higher susceptibility than Flake C at the same field. The divergence of χ_{ac} at transition temperature $T_C = 30.5$ K fits a critical exponent $\gamma = 1.1 \pm 0.3$, shown as the red line in the upper panel of (b); while the dc magnetization scales with a critical component $\beta = 0.4 \pm 0.09$, shown as the red line in the lower panel of (d). Arrows in (c) represent the frequency dependence in Figure 4.5.1 with corresponding colors. χ_{ac} are all taken with XY8-N2 238 kHz.

where $\omega = 2\pi f_{ac}$. The domain wall movement is like a damped harmonic oscillation [94, 95]. ω_0 is the resonance frequency and ω_c characterizes the relaxation and contributes to the imaginary component of ac susceptibility. With our ac susceptometry, the imaginary would be observed as unsynchronization of total ac field and XY8 sequences. In other words the fringes pattern in Figure 4.4.1 (b) would shift left or right with respect to the center if the imaginary component is present. In this work we never observed any imaginary above the uncertainty level for any flake at various temperatures and fields, indicating there is little spin ice nature in $CrBr_3$. The resonance frequency ω_0 exceeds 700 MHz [96], therefore without considering the imaginary component the susceptibility is fitted to:

$$\chi(\omega) = \frac{\omega_0}{1 + (\omega/\omega_c)^2} \tag{4.2}$$

ω_c approximately fits 2 MHz at 22 K and fits 1 MHz at 10 K, indicating a slow relaxation in $CrBr_3$. In the damped oscillation model, ω_c is proportional to restoring force and anti-proportional to the damping viscosity. A small relaxation frequency means a strong damping in domain wall movement caused by pinning sites. In addition, for ferromagnetic insulators the damping is partially contributed by lattice-spin relaxation, which is proportional to the square root of uniaxial anisotropy. This is consistent with the observation that the fitted ω_c decrease monotonically from 22 K to 10 K because the anisotropy term increases with decreasing temperature [97].

4.5 conclusion

The application of ac susceptometry on $CrBr_3$ demonstrates NV centers a true mutlimodal probe for few-layer magnetic materials. The precision of the ac magnetic field reaches as low as 40 nT, two orders of magnitude smaller than the precision accessible with dc magnetometry. It was found that different thicknesses of $CrBr_3$ flakes exhibit varied magnetic behavior in hysteresis and ac susceptibility measurements, influenced by factors such as layer number, temperature, and local microstructure. An interesting yet challenging future step is to apply the technique to scanning NV measurements for nanoscale imaging of ac susceptibility. Our development paves the way for studying subgigahertz magnetic dynamics in diverse 2D systems, especially those lacking magneto-optical coupling [98–100] and nanoparticles at the single-particle limit [101].

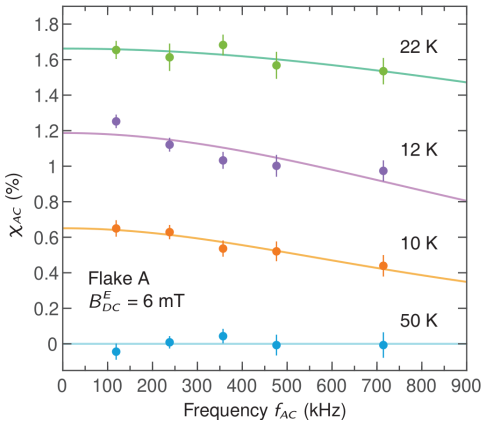

Figure 4.5.1: Frequency dependence of ac susceptibility for Flake A (10-layer) at 50 K (blue), 22 K (green), 12 K (purple), and 10 K (orange) during FC. The solid lines are fits using a damped driven domain wall oscillation model. The repetition of dynamical decoupling pulses increases for higher frequency (e.g. XY8-N6 for 714 kHz).

Chapter 5
Defect Assisted Magnetization Tuning of CrCl3

The work in this chapter and Ch 3.3 is supported by NSF DMR-2047214, NSF ECCS-2041779, and FA2386-21-1-4095. The findings and conclusions do not necessarily reflect the view of the funding agency.

5.1 introduction

Since the discovery of 2D magnets, their properties have been explored with optical characterization method. On one hand, the magnetism induces tuning in optical reflection [66, 67], absorption [65], polarization [59, 102] and spectrum [103]; on the other hand, efforts have been made to modulate magnetism with optical pulses through spin-valley coupling [104], valley-asymmetric proximity effect [105], moire band tuning [106], doped magnetic transition metal atoms [107], and spin transfer between carriers and local moments [108]. One of the mechanisms of light-magnetism interaction is driven by the exciton, where an electron forms a pair with a nearby hole. In bulk materials, excitons are known to influence magnetization through charge transfer [109, 110] and exchange alternation [111, 112]. However their potential in tuning 2D magnetism remains under exploration.

In transition metal dichalcogenide (TMD) materials, excitons play an important role in the 2D limit because the reduced dimensionality decreases the dielectric screening, thus enhances the Coulomb interactions. The exciton binding energy [113] is appreciably hundreds of meV [114]. In the chromium trihalide materials, excitons are characterized as localized or Frenkel type, which are less sensitive to dimensionality and exhibit an even larger binding energy on the order of several eV [115–117]. Among the three chromium trihalide materials, $CrCl_3$ displays the weakest *d-p* hybridization between the ligand and the Cr atoms, thus features the smallest exciton radii and the largest binding energy [73, 75]. Therefore we expect a long lifetime for excitons in $CrCl_3$.

Here we study the transient magnetic moment in few-layer $CrCl_3$ with a pump-probe setup, where the optical excitation is synchronized with a quantum dynamical decoupling sequence. Compared with the conventional dc measurement where the stray field is only strong around the flake edges, the pump-probe measurement has a faster and more straightforward imaging ability, given that the transient stray field is uniform when the optical excitation is scanned across the flake. We identify a remarkable enhancement of the in-plane magnetization density up to 0.5 μ_B/nm^2 which displays strong contrast between even and

odd layers, consistent with the layered antiferromagnetism. The relaxation of this enhancement is also significantly slow, with a lifetime up to 26 μs. Guided by DFT calculations, we attribute the transient moment to electrons hopping from the defect level to the positively-polarized $CrCl_3$ conduction band. Combined with time-resolve PL measurement, we infer that the electron hopping arises from the Auger recombination [118, 119]. Once an exciton is generated, it either triggers the Auger recombination inducing a spin inversion, or decays radiatively emitting a photon. Our results demonstrate the optical tunability of magnetization through defect adsorption, and provide insights for further exploration in tuning magnetic properties such as critical temperatures [120], magnetic ground state [100] and anisotropy [121].

5.2 in-plane layered antiferromangetization

We first demonstrate the antiferromagnetism in $CrCl_3$ with dc magnetometry. The few-layer $CrCl_3$ flakes are exfoliated and transferred onto top of the diamond with ensemble NV centers, which are ^{12}C isotopically-enriched and show prolonged coherence time. The flake identification and transfer are operated in an argon-filled glovebox unless otherwise described. After encapsulating the flakes with hBN, the diamond was exposed in ambient environment for a minimized time and then loaded into the cryostat.

The layered in-plane antiferromagnetism in $CrCl_3$ with a Neel temperature of approximately 17 K [122] was previously characterized with tunneling magnetoconductance [72, 87, 123, 124] and x-ray magnetic circular dichroism (MCD) with a glazing angle [125] in thin films. Traditional MCD with a normal incident angle is unable to detect in-plane magnetization. Here we use pulsed optically detected magnetic resonance (ODMR).

In Figure 5.2.1, the stray field at a bias field of 3.3 mT (c) and 141.5 mT (e) are plotted. The flake comprises four to six layers and the layer numbers for different sections of this flake are indicated in (a). At 3.3 mT the stray field is mostly near the edge of the 5-layer and the 9-layer. As the field increases to 141.5 mT, we notice that: the stray field contributed from the 8-layer and the nearby 6-layer increases from negligible to almost double that of the odd layers; the stray field near the edge of the 9-layer grows to similar amount as the 5-layer and the 7-layer; the stray field near the edge of the 4-layer and the nearby 6-layer section increases but remains small.

We attribute these changes to the following evolution of magnetic moments: Firstly, one of the anti-aligned layers in the 8-layer and the nearby 6-layer flips, resulting in a switch from fully-compensated to doubly uncompensated; Secondly, the 9-layer has a higher saturation

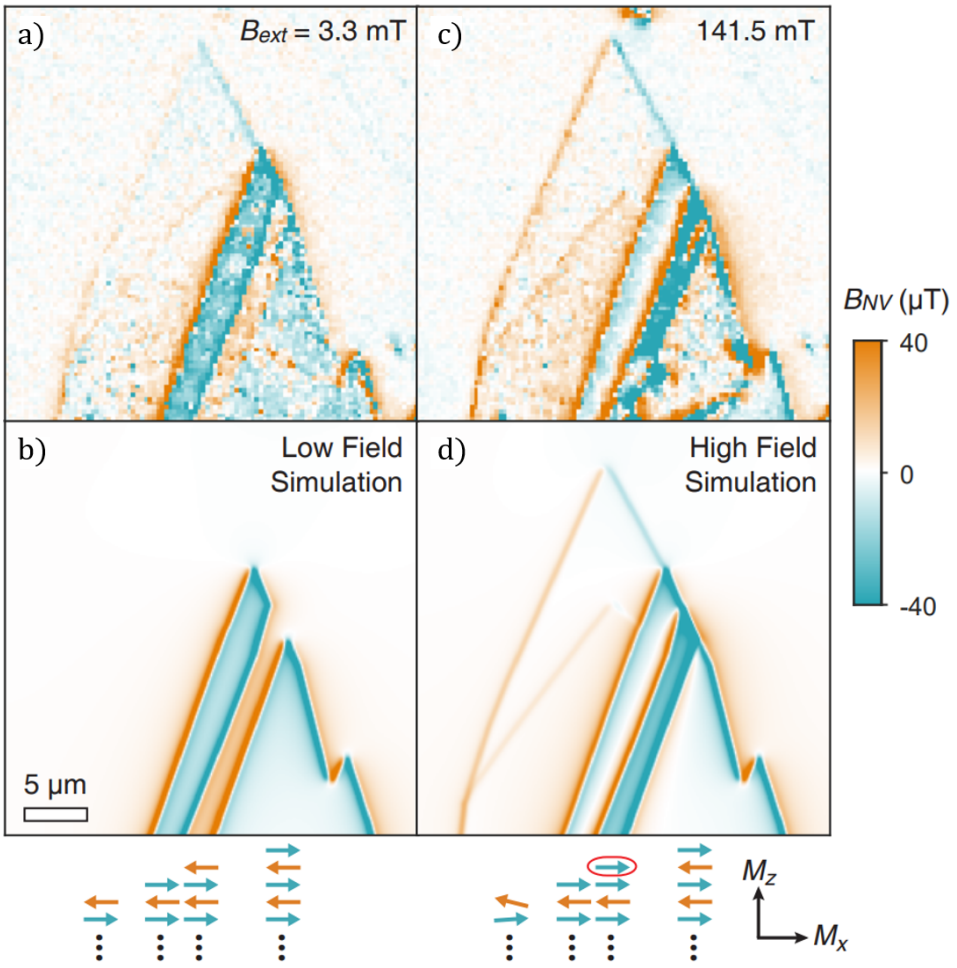

Figure 5.2.1: (a, c) Experimental stray field data of ODMR at different bias field. (b, d) Simulated stray field at different bias field. The configurations of magnetization which generate the simulations are indicated underneath. At high field the 8-layer has a flipped layer of magnetization (circled in red).

field than the others, thus at low field it is fragmented or not polarized, and at high field it shows a saturated uncompensated moment as the other odd layers; Thirdly, the 4-layer and the nearby 6-layer start to tilt out-of-plane in a strong field. A simulation of the stray field with the proposed magnetization [77] is plotted in (d) and (e), in close alignment with the data. It reveals an uncompensated layer of 14 μ_B/nm^2 magnetization density, slightly reduced from the expected saturation of 19 μ_B/nm^2. Our ODMR imaging well characterizes the layered antiferromagnetism in $CrCl_3$.

5.3 optical modulation of magnetic moments

We then present the sensing of optically induced transient field. As shown in Fig 5.3.1, the measurement synchronizes an optical excitation with the Hahn Echo sensing protocol, such that the accumulated phase measured as $\Phi = \arctan\left(\frac{Y_P}{X_P}\right)$ is proportional to the difference between the integral of stray field over the first τ and the second τ. The Hahn Echo measurement uncovers a surprising transient stray field on $CrCl_3$, and shows a striking difference between odd and even layers. Fig 5.3.1 (c-e) measures Hahn Echo as a function of τ on the bare diamond, the 5-layer and the 6-layer separately, the locations of which are indicated in (f). The curves in (c-e) are simultaneous fit of $X_P = e^{-\left(\frac{2\tau}{\tau_{\text{coh}}}\right)^p} \cdot \cos(\Phi(2\tau)), Y_P = e^{-\left(\frac{2\tau}{\tau_{\text{coh}}}\right)^p} \cdot \sin(\Phi(2\tau))$. Contrasted by the bare diamond where the coherence time fits $\tau_{\text{coh}} = 113\ \mu$s, the 6-layer $CrCl_3$ shows a significantly shorter coherence time $\tau_{\text{coh}} = 24\ \mu$s, indicating the existence of magnetic noise but with a zero average; the 5-layer $CrCl_3$ shows not only a decoherence but also an increasing accumulated phase Φ, indicating a transient magnetic field varying on the order of μs to tens of μs.

We then fix $2\tau = 13\mu$s and sweep this sensing protocol across the flake. The accumulated phase induced by the transient stray field is plotted in Fig 5.3.1 (f). Consistent with (c-e), it shows that the transient field uniformly exists across the 5-layer, while the signal is significantly less across the 6-layer and 8-layer. It is also noticeable that the transient field is as small on the bulk as on the even layers. The static stray field measured with ODMR on the same flake is shown in Fig 5.3.1 (a). As expected, the stray field is mostly around the edge of the 5-layer. We attribute the localized stray field along the edge of 8-layer to be magnetic edge defects, or a tiny piece of odd-layer that cannot be resolved in the optical layer identification. The bulk piece shows non-uniform magnetization. This fragmentation could explain its negligible transient field, since the magnetization modulation could average to zero.

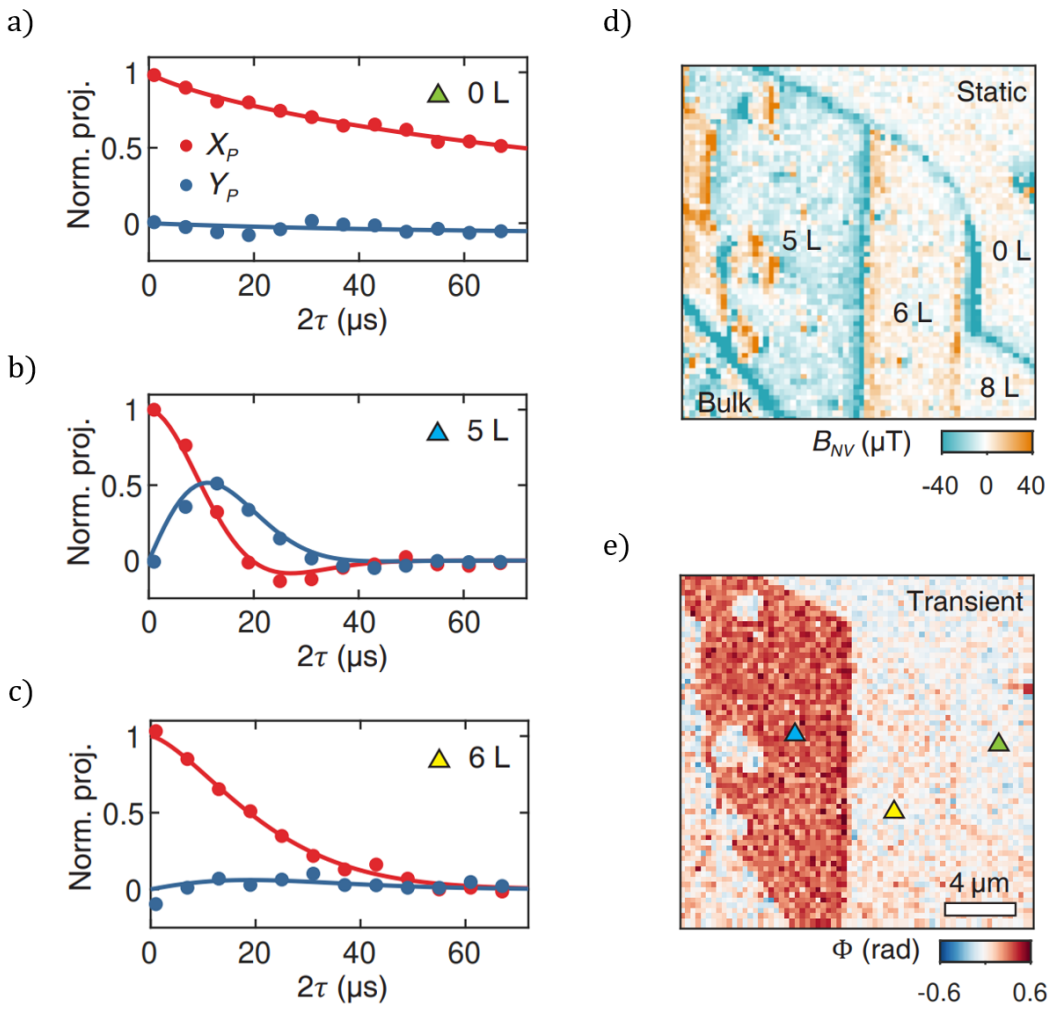

Figure 5.3.1: Single beam pump-probe measurement on the 5, 6, 8-layer and bulk area using the Hahn Echo sequence. (a-c) The Hahn Echo measurement as a function of 2τ. (e) Hahn imaging by scanning the single green beam, where 2τ is fixed to be 13 μs. The triangles mark the locations of measurement in (c-e) with corresponding colors. It shows the even-odd effect compared with the static field imaing in (d)

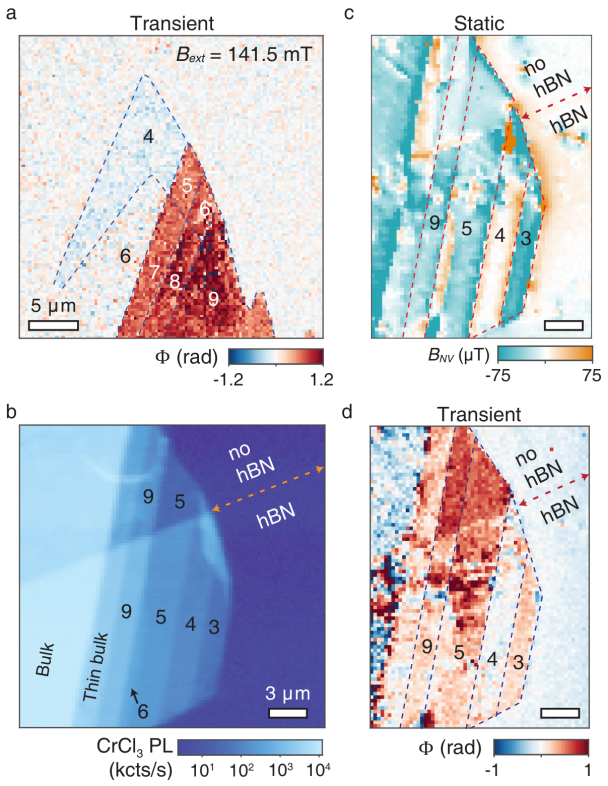

Figure 5.3.2: Single beam transient field measurement on two other flakes illustrating defect level effect. (a) Hahn imaging at 141.5 mT. The configuration of magnetization is shown in Figure 1(e-f). The 8-layer stripe has similar intensity as its odd layer neighbors, although the 8-layer has double the uncompensated net magnetization. (b) PL imaging where the wavelength is filtered to be above 800 nm. The hBN-covered part has higher PL intensity, indicating the excitons are more inclined to go through the radiative pathway. (c) ODMR data showing the even-odd parity and the weaker magnetization in the exposed part. (d) Hahn imaging showing the transient stray field is much stronger in the exposed part, indicating the defect is responsible for the transient enhancement of magnetic moment.

5.4 pump-probe imaging of the transient stray field

In order to figure out the origin of this optically excited effect, it is important to image the whole profile of the transient field. With the single beam protocol mentioned above, we are only able to measure the stray field at the same location of the excitation. Therefore we employ a two-beam setup, where the pumping is applied by a separately steered laser beam of variable wavelength.

The imaging result is shown in Fig 5.4.3 at different temperatures. It is taken with a bias field of 141 mT and excited with 730 nm and 515 nm pump beam on two different 7-layer flakes. The profile of the Φ below Neel temperature shows a two-lobe pattern of a circular shape, and the location of pumping (yellow circle) resides in the positive lobe. This sign switching feature and the deviation of the lobe boundary to the left of the pumping location are reminiscent of the static stray field of in-plane magnetization. Therefore we are inspired to fit the pattern to the stray field created by a gaussian-like amplification of the in-plane magnetization, as shown in Fig 5.4.1. The fit turns out to be excellently capturing the features of the data. We also fit the data to the stray field of amplified magnetization along several different directions, and we are confident to say that the direction should be within $\pm 10^\circ$ with respect to the in-plane direction.

The temperature dependence shows that the transient field stays nearly the same far below the Neel temperature. While approaching the Neel temperature upon warming to 16K, the profile is completely changed. A finer resolution on temperature in the shows a more drastic and non-repeatable profile evolution. We attribute these subtle patterns to domain formation and magnetization rotation, as the anisotropy is weakened near the critical temperature.

We emphasize that the optical effect we observe indeed corresponds to an *enhancement* in magnetization, rather than a trivial heat-induced de-magnetization. Firstly, the accumulated phase by our sensing protocol is given in Eq 5.1, therefore a positive accumulated phase correspond to a negative stray field above the anti-crossing field of 102.7 mT. This inference is also supported by a test measurement with an electrical current applied through the coil. Then based on the stray field profile, it is reconstructed that the transient moment is aligned with the applied field, indicating an enhancement of magnetization. Secondly, the lifetime of the transient field (tens of μs) is significantly longer than what would be expected (1 μs) for thermal demagnetization. Ref [127] shows that the accumulated phase due to thermal effect quickly saturates when 2τ exceeds the thermal time constant. It is a completely different behavior from Fig 5.5.1 where Φ keeps increasing without slowing down from 8 μs to 46 μs.

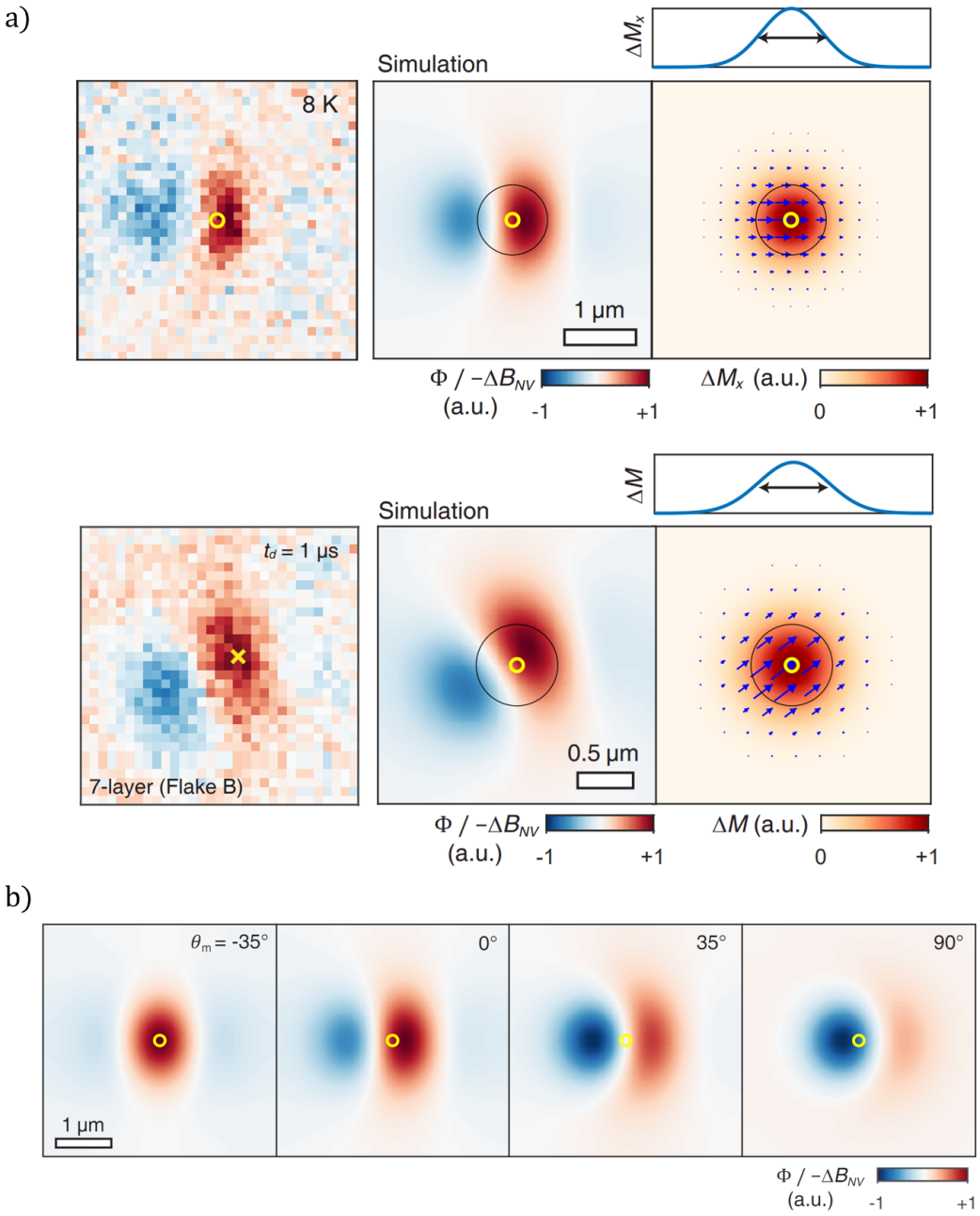

Figure 5.4.1: (a) Φ mapping measurement (left) on two 7-layer flake. It is pumped with $\lambda = 730$ nm, $P = 220$ μW. Timing is chosen to maximize the contrast: $t_p = 1.2$ μ, $t_d = 0$ μs, $2\tau = 13$ μs. Transient moment (right) and stray field (middle) fitted to the data on the left. The bottom pattern fits an in-plane angle of 37° with respect to bias field. (b) Simulation of stray field with different magnetization direction. $\theta_m = 0$ means in-plane, $\theta_m = 90°$ means out-of-plane, $\theta = 35°$ means along NV center direction.

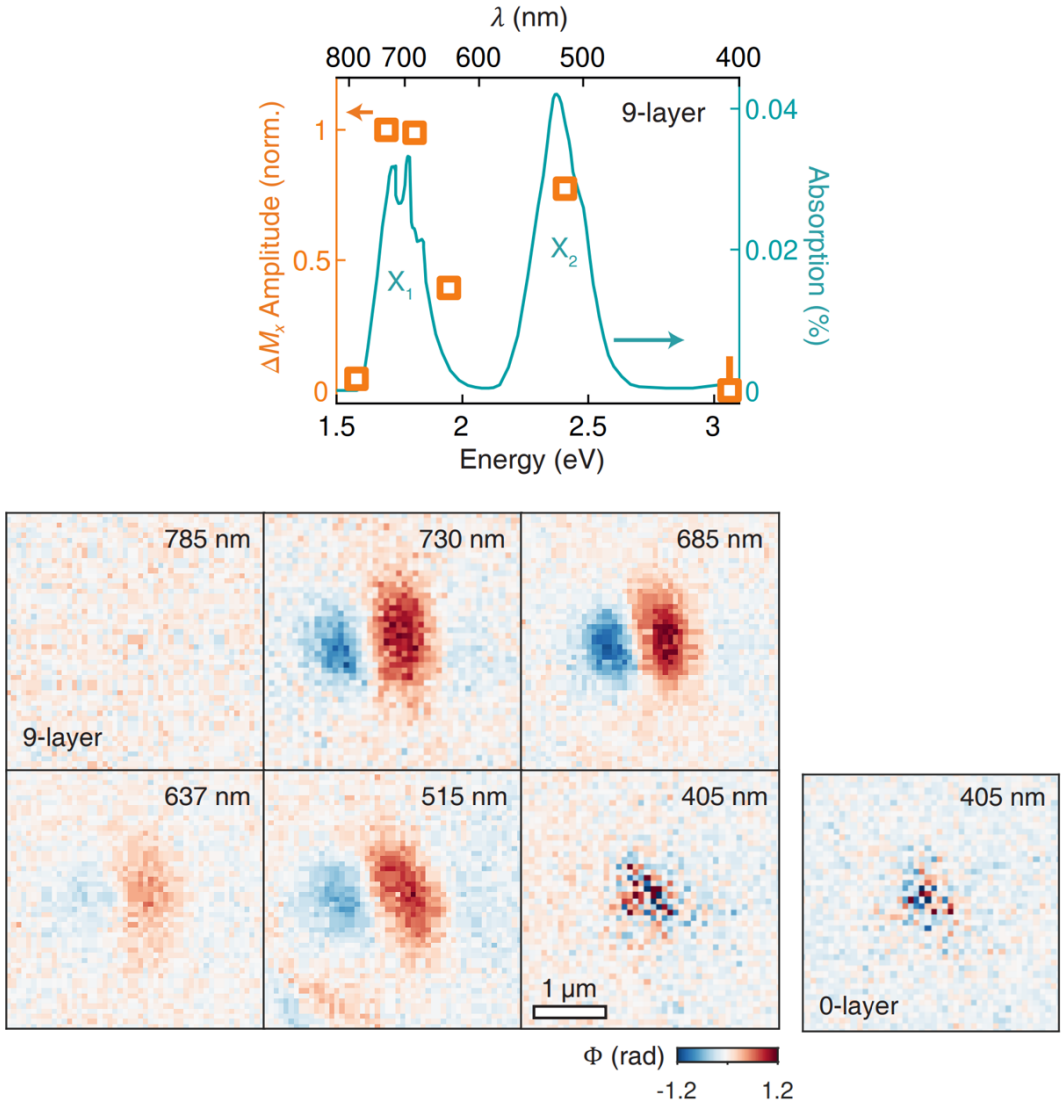

Figure 5.4.2: The transient moment amplitude as a function of wavelength. Φ mappings with variable wavelength are measured, and the fitted 2D gaussian amplitudes represent the amplitudes of ΔM_x. The absorption data re-plotted from Ref [126] reveals that the two-peak feature of the magnetization enhancement coincides with the d-d excitons X_1 and X_2. The optical power P for $\lambda > 405$ nm is 180 μW; for $\lambda = 405$ nm, P = 55 W and the fitted amplitude is scaled for fair comparison. For $\lambda < 637$ nm, the pump beam can excite or convert the charge state of NV centers, but this introduces only incoherent photon noise, while the coherent signal is contributed by NV centers that remain in the correct, microwave-addressable ground state. To allow some fraction of excited NV centers to relax, we use a non-zero delay $t_d = 1$ μs for all λ here. Some noise is still visible in the $\lambda = 405$ nm image, but it is not contributed by CrCl3 since similar noise occurs over the bare diamond substrate (0-layer).

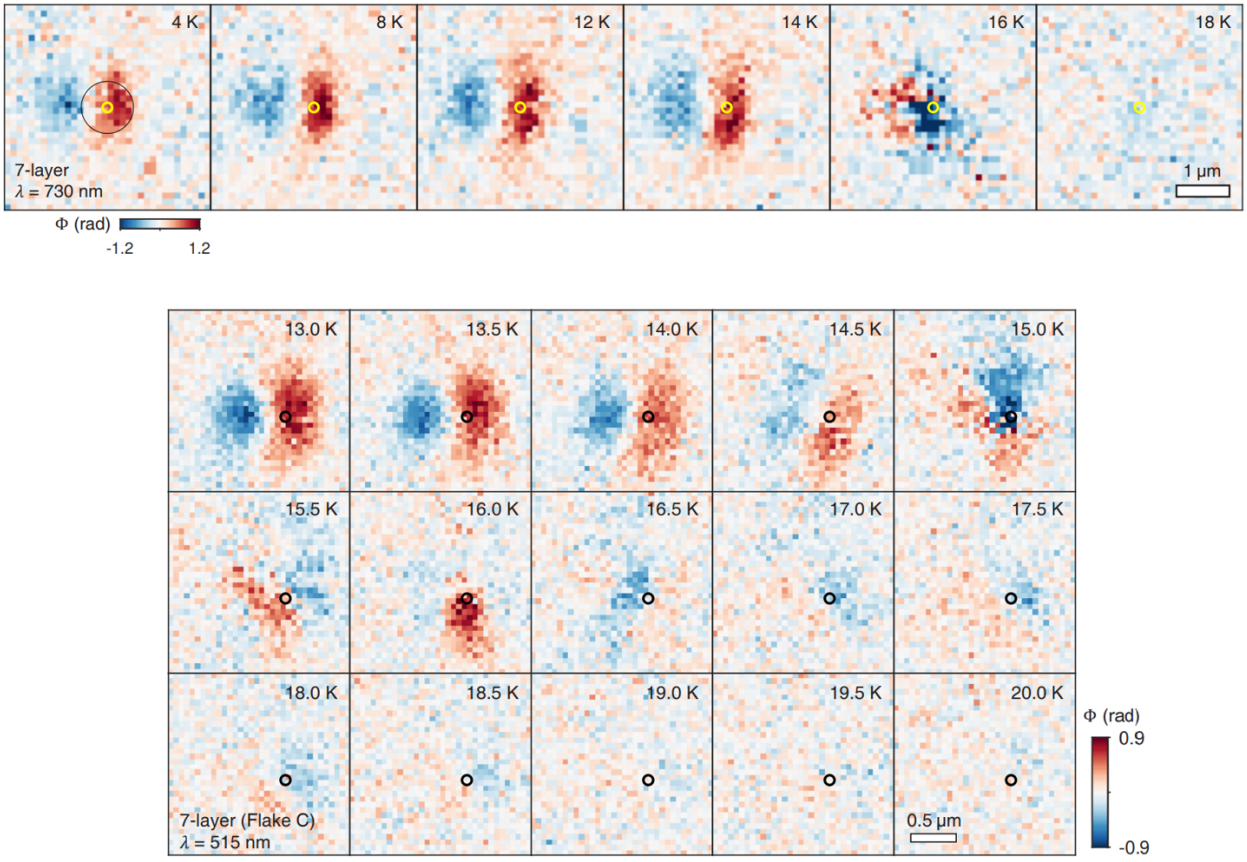

Figure 5.4.3: Φ mappings as a function of temperature on two different 7-layer flakes with different wavelength. Above 14.5 K, the pattern begins to change rapidly and display non-circular features, which may reflect enhanced disorder and laser-heating effects near the phase transition.

5.5 role of exciton

We vary the wavelength of the pump laser and the result is summarized in Fig 5.4.2. We attribute the two-peak feature to the two modes of bright excitons X_1 and X_2 inside the band gap of $CrCl_3$, corresponding to the d-d transitions ${}^4A_2 \rightarrow {}^4T_1$ and ${}^4A_2 \rightarrow {}^4T_2$ [64]. The absorption data from Ref [126] is plotted in the same graph for comparison. The e-h binding energy of $CrCl_3$ is enormous, compared with not only other types of 2D semiconductors such as MoS_2 or black phosphorous but also its sibling magnetic material CrI_3 [116]. This strongly long-lived characteristic of $CrCl_3$ exciton should promote other transition pathways if existent.

We also measure a flake half covered by hBN, and find that the uncovered part induces significantly larger transient field than the covered part as shown in Fig 5.3.2(b-d). Meanwhile the doubly uncompensated 8-layer doesn't have double amount of Φ. The transient field is of almost equal intensity on either doubly uncompensated even layers or singly uncompensated odd layers, as shown in Fig 5.3.2(a). These evidence indicate the intensity of the transient field is not proportional to the magnetization at equilibrium, but positively correlated to the surface defect density.

Considering all the information provided above, we infer that 1) the transient moment is prompted through a non-radiative pathway of the excitons, 2) the population of the excitons going through this non-radiative pathway is proportional to the defect density. In order to explore the relation between the transient moment and the exciton, we then characterize the lifetime of both the transient moment and the photoluminescence (PL) excited by excitons. The lifetime for the transient moment is extracted by a simultaneous fit of the Fig 5.5.1 (b) measurement with varying τ and t_d. We assume a gaussian decay of ΔM_x, then for each specific τ and t_d, Φ measures as:

$$\Phi(\vec{r},\tau,t_d) = \mathcal{D}(\vec{r})\left[\int_{t_d}^{t_d+\tau} M(t)dt - \int_{t_d+\tau}^{t_d+2\tau} M(t)dt\right] \quad \text{where } M(t) = M_0 e^{-\left(\frac{t}{\tau_m}\right)^{\alpha}} \tag{5.1}$$

Here we use $M(t)$ to represent the time-dependent amplitude of the transient moment, which has a 2D-gaussian spatial profile. *i.e.* $\Delta M_x(\vec{r'},t) = M(t)\cdot\exp\left(-|\vec{r'}/r_0|^2\right)$. $\mathcal{D}(\vec{r})$ is the transient field profile, representing the factor converting M to $\Phi(\vec{r})$, and $\vec{r}$ is where the green laser parks. The factor $\mathcal{D}$ is taken as invariant of time t, because the width of the gaussian $\Delta M_x(\vec{r'},t)$ is not shrinking as the amplitude decays. As shown in Fig 5.5.1 (a), the size of the two lobes remains as their amplitude becomes lower.

The accumulated phase with varying τ and t_d is plotted in Fig 5.5.1 (b). We choose $\vec{r}$ such that it provides the strongest Φ, and the location is indicated by the yellow cross in (a). All the data points are simultaneously fitted to Eq 5.1. M_0, τ_m and α are flexible, $\mathcal{D}(\vec{r})$ is known, τ and t_d are independent variables, Φ is the dependent variable. The fitted result is $\tau_m = 26 \pm 3$ μs, $\alpha = 0.5 \pm 0.1$ and $M_0 = 0.46 \pm 0.10$ μ_B/nm^2 as plotted in (c).

PL measured under the same wavelength and power is plotted in (d). By comparison we can tell the PL lifetime (38 ns) is almost three orders of magnitude smaller than the transient moment. PL measurement with varying layer number and power is summarized in (e-g). Firstly, flakes covered with hBN systematically display higher PL per layer and lifetime, and display lower transient moment, as shown in Fig 5.3.2 (d)). This indicates the mechanism inducing the transient moment is competing with the mechanism inducing PL. Secondly, flakes of higher layer number have higher PL per layer and higher PL lifetime. This phenomenon is also reported in the CrI_3, indicating that the *d-d* relaxation processes are affected by interlayer or flake-substrate interactions [59]. Thirdly, the PL lifetime is nearly independent of laser power. Given that laser power is normally taken as proportional to exciton density, it indicates that the mechanism inducing the transient moment is independent of exciton density. This is consistent with our previous observation from Φ mapping that the transient field intensity is only related to the surface defect density.

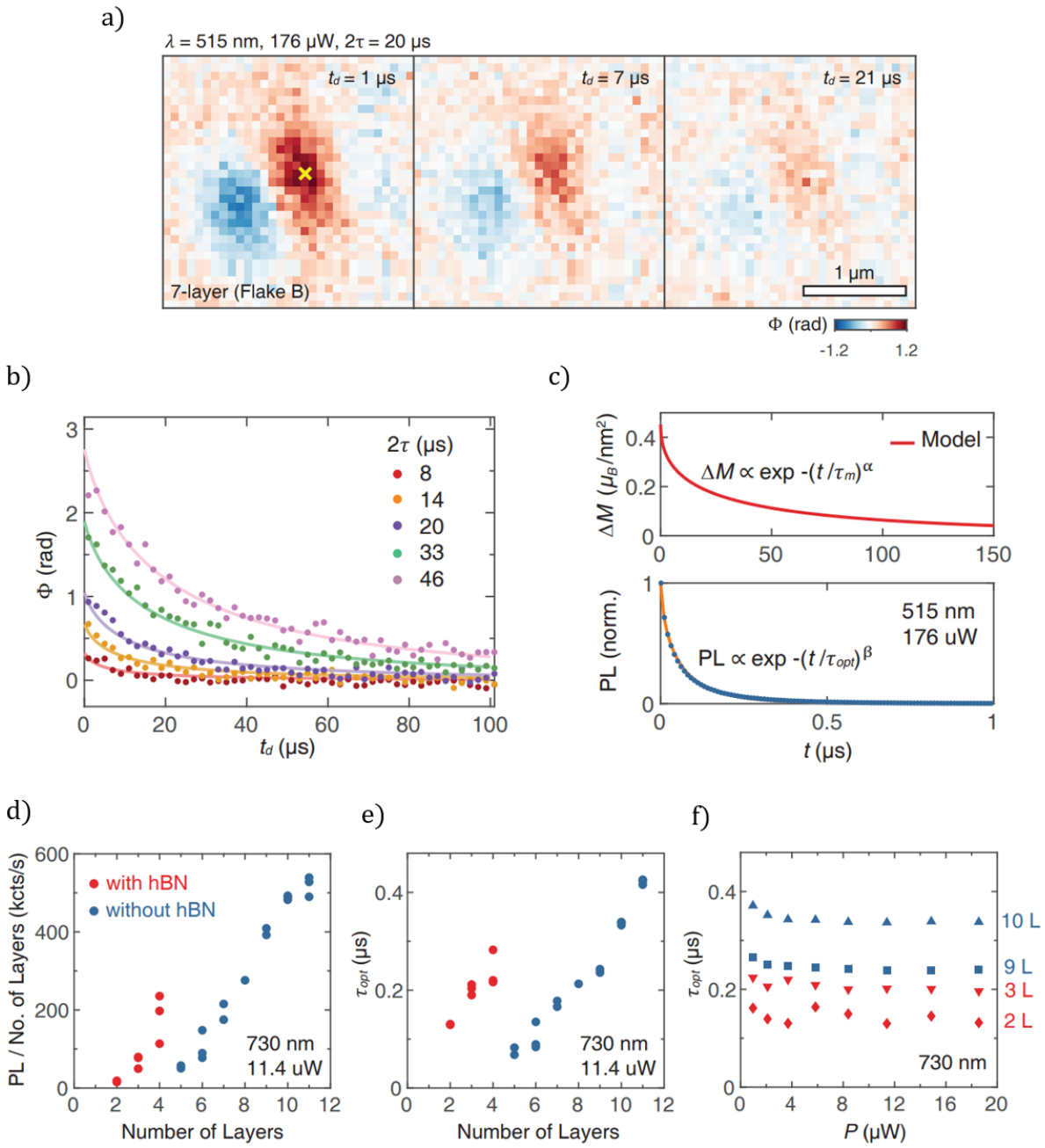

Figure 5.5.1: (a) Spatiotemporal Φ imaging with varying t_d. The rotation of the two-lobe pattern indicates a deviation of transient moment from the x-axis. This is possibly a sign of flake-dependent anisotropy competing with the applied bias field. (b) Φ intensity with varying t_d and t_p. It is pumped with $\lambda = 730$ nm, $P = 220$ μW. (c) The result of a simultaneous fit to all the data points in (b) to the model in Eq 5.1, yielding $\tau_m = 26$ μs and $\alpha = 0.5$. (d) Time resolved PL collection pumped with the same lumination as (b). The fitted decay yields $\tau_{\text{opt}} = 38$ ns and $\beta = 0.60$. (e) PL intensity per layer versus number of layers (f) Fitted PL lifetime versus number of layers. (g) Fitted PL lifetime versus lumination power. $\beta = 0.79$ is fixed for fitting lifetimes in (f-g). Red (blue) denotes $CrCl_3$ encapsulated (unencapsulated) with hBN.

5.6 defect assited Auger recombination

Putting all the evidence together, we arrive at the conclusion that the exciton causes the transient moment through an Auger recombination process assisted with a surface defect level. The transient moment has a much longer lifetime than PL, therefore we rule out the exciton itself being the direct cause of the transient moment. Rather, the excitons bring out some other transitions to levels of long lifetime. Furthermore, the independency with the laser power, i.e. exciton density, is a feature of Auger recombination with localized defect [118, 119]. It is distinctive from the traditional Auger recombination, where exciton-exciton interaction dominates the rate and the signal is inversely proportional to the exciton density [128].

As shown in Fig 5.6.1, upon exciton creation, there are two pathways the electron can be released. One is the radiative way where the system emits a photon. The other way is non-radiative, where the electron in the defect level combines with a nearby hole in the valence band, and the released energy kicks the exciton electron to the conduction band. The net effect of the non-radiative way is one electron hopping from the defect level to the conduction band. As a result the transient moment equals the magnetization difference between the conduction band and the defect level.

Although $CrCl_3$ is relatively stable under ambient conditions, surface oxidation, Cl defects and water adsorption have been identified with theoretical simulations and several experimental probes [129, 130]. Further experiments with contamination control and the density functional theory (DFT) calculation would reveal the specific defect with such a in-gap level of spin neutral or spin down. While in the pristine $CrCl_3$, the conduction and the valance band that are most proximate to the Fermi level are spin up. Thus when the electron is moved from the defect level to the conduction band, the net transient moment is double the spin up, enhancing the magnetization.

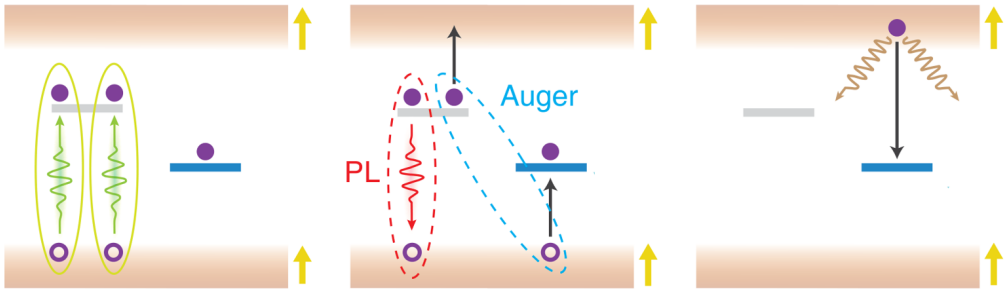

Figure 5.6.1: Left: an oppositely magnetized defect level resides in the $CrCl_3$ bandgap. Near-resonant photons stimulates the formation of excitons. Middle: An exciton has two pathways. One is to radiatively emit a photon. The other one is to trigger the Auger recombination, where the binding energy prompts the electron hopping from the defect level to the conduction band. Right: The excited state decays with multi-phonon emission. The ionized defect level recaptures the electron.

5.7 conclusion

In this work, we demonstrate the tuning of the optically induced transient magnetization with the pump-probe quantum sensing technique. Experimental data and theoretical calculations corroborate an exciton-induced Augur recombination process assisted with surface adsorbent. This mechanism could be generic in materials where excitons have high binding energy, such as $CrPS_4$ [131], $MnPX_3$ [132] and Fe-doped MoS_2 [133]. In addition, our pump-probe method provides an extensively applicable platform to sense photo-magnetism effect. Our findings provide new insights into ideas regarding optically-responsive magnet devices, which could be crucial in future design of spintronics devices.

References

[1] David D. Awschalom, Ronald Hanson, Jörg Wrachtrup, and Brian B. Zhou. Quantum technologies with optically interfaced solid-state spins. *Nature Photonics*, 12(9):516–527, Sep 2018.

[2] F. Jelezko and J. Wrachtrup. Single defect centres in diamond: A review. *physica status solidi (a)*, 203(13):3207–3225, 2006.

[3] Romana Schirhagl, Kevin Chang, Michael Loretz, and Christian L. Degen. Nitrogen-vacancy centers in diamond: Nanoscale sensors for physics and biology. *Annual Review of Physical Chemistry*, 65(Volume 65, 2014):83–105, 2014.

[4] P. J. Scheidegger, S. Diesch, M. L. Palm, and C. L. Degen. Scanning nitrogen-vacancy magnetometry down to 350 mK. *Applied Physics Letters*, 120(22):224001, 05 2022.

[5] Margarita Lesik, Thomas Plisson, Loïc Toraille, Justine Renaud, Florent Occelli, Martin Schmidt, Olivier Salord, Anne Delobbe, Thierry Debuisschert, Loïc Rondin, Paul Loubeyre, and Jean-François Roch. Magnetic measurements on micrometer-sized samples under high pressure using designed nv centers. *Science*, 366(6471):1359–1362, 2019.

[6] P. Maletinsky, S. Hong, M. S. Grinolds, B. Hausmann, M. D. Lukin, R. L. Walsworth, M. Loncar, and A. Yacoby. A robust scanning diamond sensor for nanoscale imaging with single nitrogen-vacancy centres. *Nature Nanotechnology*, 7(5):320–324, May 2012.

[7] Matthew E. Trusheim, Luozhou Li, Abdelghani Laraoui, Edward H. Chen, Hassaram Bakhru, Tim Schröder, Ophir Gaathon, Carlos A. Meriles, and Dirk Englund. Scalable fabrication of high purity diamond nanocrystals with long-spin-coherence nitrogen vacancy centers. *Nano Letters*, 14(1):32–36, 2014. PMID: 24199716.

[8] Xinghan Guo, Nazar Delegan, Jonathan C. Karsch, Zixi Li, Tianle Liu, Robert Shreiner, Amy Butcher, David D. Awschalom, F. Joseph Heremans, and Alexander A. High. Tunable and transferable diamond membranes for integrated quantum technologies. *Nano Letters*, 21(24):10392–10399, 2021. PMID: 34894697.

[9] M. V. Hauf, B. Grotz, B. Naydenov, M. Dankerl, S. Pezzagna, J. Meijer, F. Jelezko, J. Wrachtrup, M. Stutzmann, F. Reinhard, and J. A. Garrido. Chemical control of the charge state of nitrogen-vacancy centers in diamond. *Phys. Rev. B*, 83:081304, Feb 2011.

[10] F. Maier, M. Riedel, B. Mantel, J. Ristein, and L. Ley. Origin of surface conductivity in diamond. *Phys. Rev. Lett.*, 85:3472–3475, Oct 2000.

[11] P. Siyushev, H. Pinto, M. Vörös, A. Gali, F. Jelezko, and J. Wrachtrup. Optically controlled switching of the charge state of a single nitrogen-vacancy center in diamond at cryogenic temperatures. *Phys. Rev. Lett.*, 110:167402, Apr 2013.

[12] L Rondin, J-P Tetienne, T Hingant, J-F Roch, P Maletinsky, and V Jacques. Magnetometry with nitrogen-vacancy defects in diamond. *Reports on Progress in Physics*, 77(5):056503, may 2014.

[13] F. Dolde, H. Fedder, M. W. Doherty, T. Nöbauer, F. Rempp, G. Balasubramanian, T. Wolf, F. Reinhard, L. C. L. Hollenberg, F. Jelezko, and J. Wrachtrup. Electric-field sensing using single diamond spins. *Nature Physics*, 7(6):459–463, Jun 2011.

[14] Ph. Tamarat, T. Gaebel, J. R. Rabeau, M. Khan, A. D. Greentree, H. Wilson, L. C. L. Hollenberg, S. Prawer, P. Hemmer, F. Jelezko, and J. Wrachtrup. Stark shift control of single optical centers in diamond. *Phys. Rev. Lett.*, 97:083002, Aug 2006.

[15] N. Bar-Gill, L. M. Pham, A. Jarmola, D. Budker, and R. L. Walsworth. Solid-state electronic spin coherence time approaching one second. *Nature Communications*, 4(1):1743, Apr 2013.

[16] David A. Hopper, Henry J. Shulevitz, and Lee C. Bassett. Spin readout techniques of the nitrogen-vacancy center in diamond. *Micromachines*, 9(9), 2018.

[17] Paola Cappellaro. Course note of quantum theory of radiation interactions, 2012.

[18] Wikipedia. Rotating-wave approximation — Wikipedia, the free encyclopedia, 2023.

[19] Adam Gali, Maria Fyta, and Efthimios Kaxiras. Ab initio supercell calculations on nitrogen-vacancy center in diamond: Electronic structure and hyperfine tensors. *Phys. Rev. B*, 77:155206, Apr 2008.

[20] M. L. Goldman, M. W. Doherty, A. Sipahigil, N. Y. Yao, S. D. Bennett, N. B. Manson, A. Kubanek, and M. D. Lukin. State-selective intersystem crossing in nitrogen-vacancy centers. *Phys. Rev. B*, 91:165201, Apr 2015.

[21] Marcus W. Doherty, Neil B. Manson, Paul Delaney, Fedor Jelezko, Jörg Wrachtrup, and Lloyd C.L. Hollenberg. The nitrogen-vacancy colour centre in diamond. *Physics Reports*, 528(1):1–45, 2013. The nitrogen-vacancy colour centre in diamond.

[22] A. Jarmola, V. M. Acosta, K. Jensen, S. Chemerisov, and D. Budker. Temperature- and magnetic-field-dependent longitudinal spin relaxation in nitrogen-vacancy ensembles in diamond. *Phys. Rev. Lett.*, 108:197601, May 2012.

[23] Chunhui Du, Toeno van der Sar, Tony X. Zhou, Pramey Upadhyaya, Francesco Casola, Huiliang Zhang, Mehmet C. Onbasli, Caroline A. Ross, Ronald L. Walsworth, Yaroslav Tserkovnyak, and Amir Yacoby. Control and local measurement of the spin chemical potential in a magnetic insulator. *Science*, 357(6347):195–198, 2017.

[24] Toeno van der Sar, Francesco Casola, Ronald Walsworth, and Amir Yacoby. Nanometre-scale probing of spin waves using single electron spins. *Nature Communications*, 6(1):7886, Aug 2015.

[25] Sebastian Zaiser. *A single electron sensor assisted by a quantum coprocessor*. Dissertation, Universität Stuttgart, 08 Fakultät Mathematik und Physik, 2019.

[26] G. Waldherr, Y. Wang, S. Zaiser, M. Jamali, T. Schulte-Herbrüggen, H. Abe, T. Ohshima, J. Isoya, J. F. Du, P. Neumann, and J. Wrachtrup. Quantum error correction in a solid-state hybrid spin register. *Nature*, 506(7487):204–207, Feb 2014.

[27] C. E. Bradley, J. Randall, M. H. Abobeih, R. C. Berrevoets, M. J. Degen, M. A. Bakker, M. Markham, D. J. Twitchen, and T. H. Taminiau. A ten-qubit solid-state spin register with quantum memory up to one minute. *Phys. Rev. X*, 9:031045, Sep 2019.

[28] Gopalakrishnan Balasubramanian, Philipp Neumann, Daniel Twitchen, Matthew Markham, Roman Kolesov, Norikazu Mizuochi, Junichi Isoya, Jocelyn Achard, Johannes Beck, Julia Tissler, Vincent Jacques, Philip R. Hemmer, Fedor Jelezko, and Jörg Wrachtrup. Ultralong spin coherence time in isotopically engineered diamond. *Nature Materials*, 8(5):383–387, 2009.

[29] Toyofumi Ishikawa, Kai-Mei C. Fu, Charles Santori, Victor M. Acosta, Raymond G. Beausoleil, Hideyuki Watanabe, Shinichi Shikata, and Kohei M. Itoh. Optical and spin coherence properties of nitrogen-vacancy centers placed in a 100 nm thick isotopically purified diamond layer. *Nano Letters*, 12(4):2083–2087, Apr 2012.

[30] S. Felton, A. M. Edmonds, M. E. Newton, P. M. Martineau, D. Fisher, and D. J. Twitchen. Electron paramagnetic resonance studies of the neutral nitrogen vacancy in diamond. *Phys. Rev. B*, 77:081201, Feb 2008.

[31] Adam Gali. Hyperfine tensors of nitrogen-vacancy center in diamond from *ab initio* calculations, 2009.

[32] M. Steiner, P. Neumann, J. Beck, F. Jelezko, and J. Wrachtrup. Universal enhancement of the optical readout fidelity of single electron spins at nitrogen-vacancy centers in diamond. *Phys. Rev. B*, 81:035205, Jan 2010.

[33] N. Bar-Gill, L. M. Pham, C. Belthangady, D. Le Sage, P. Cappellaro, J. R. Maze, M. D. Lukin, A. Yacoby, and R. Walsworth. Suppression of spin-bath dynamics for improved coherence of multi-spin-qubit systems. *Nature Communications*, 3(1):858, May 2012.

[34] M. Loretz, S. Pezzagna, J. Meijer, and C. L. Degen. Nanoscale nuclear magnetic resonance with a 1.9-nm-deep nitrogen-vacancy sensor. *Applied Physics Letters*, 104(3):033102, 01 2014.

[35] Montana Instruments. User manual - cryostation s-series. https://assets-global.website-files.com/6118466f5c775b56d53d49e9/65d4d014165cf9daaa957269_4100-1-DOC001_3.7%20(User%20Manual%20-%20Cryostation%20s-series).pdf, oct 2023. Accessed: <access date>.

[36] S Kazim, M Alì, S Palleschi, G D'Olimpio, D Mastrippolito, A Politano, R Gunnella, A Di Cicco, M Renzelli, G Moccia, O A Cacioppo, R Alfonsetti, J Strychalska-Nowak, T Klimczuk, R J Cava, and L Ottaviano. Mechanical exfoliation and layer number identification of single crystal monoclinic crcl3. *Nanotechnology*, 31(39):395706, jul 2020.

[37] L. Thiel, Z. Wang, M. A. Tschudin, D. Rohner, I. Gutiérrez-Lezama, N. Ubrig, M. Gibertini, E. Giannini, A. F. Morpurgo, and P. Maletinsky. Probing magnetism in 2d materials at the nanoscale with single-spin microscopy. *Science*, 364(6444):973–976, 2019.

[38] Qi-Chao Sun, Tiancheng Song, Eric Anderson, Andreas Brunner, Johannes Förster, Tetyana Shalomayeva, Takashi Taniguchi, Kenji Watanabe, Joachim Gräfe, Rainer Stöhr, Xiaodong Xu, and Jörg Wrachtrup. Magnetic domains and domain wall pinning in atomically thin crbr3 revealed by nanoscale imaging. *Nature Communications*, 12(1):1989, Mar 2021.

[39] Tiancheng Song, Qi-Chao Sun, Eric Anderson, Chong Wang, Jimin Qian, Takashi Taniguchi, Kenji Watanabe, Michael A. McGuire, Rainer Stöhr, Di Xiao, Ting Cao, Jörg Wrachtrup, and Xiaodong Xu. Direct visualization of magnetic domains and moiré magnetism in twisted 2d magnets. *Science*, 374(6571):1140–1144, 2021.

[40] Y. Dovzhenko, F. Casola, S. Schlotter, T. X. Zhou, F. Büttner, R. L. Walsworth, G. S. D. Beach, and A. Yacoby. Magnetostatic twists in room-temperature skyrmions explored by nitrogen-vacancy center spin texture reconstruction. *Nature Communications*, 9(1):2712, 2018.

[41] T. Hingant, J.-P. Tetienne, L. J. Martínez, K. Garcia, D. Ravelosona, J.-F. Roch, and V. Jacques. Measuring the magnetic moment density in patterned ultrathin ferromagnets with submicrometer resolution. *Phys. Rev. Appl.*, 4:014003, Jul 2015.

[42] J.-P. Tetienne, T. Hingant, L. J. Martínez, S. Rohart, A. Thiaville, L. Herrera Diez, K. Garcia, J.-P. Adam, J.-V. Kim, J.-F. Roch, I. M. Miron, G. Gaudin, L. Vila, B. Ocker, D. Ravelosona, and V. Jacques. The nature of domain walls in ultrathin ferromagnets revealed by scanning nanomagnetometry. *Nature Communications*, 6(1):6733, Apr 2015.

[43] M. J. Harris, S. T. Bramwell, D. F. McMorrow, T. Zeiske, and K. W. Godfrey. Geometrical frustration in the ferromagnetic pyrochlore $ho_2ti_2O_7$. *Phys. Rev. Lett.*, 79:2554–2557, Sep 1997.

[44] D. W. Davidson and R. H. Cole. Dielectric Relaxation in Glycerol, Propylene Glycol, and n-Propanol. *The Journal of Chemical Physics*, 19(12):1484–1490, 12 1951.

[45] V. B. Geshkenbein, V. M. Vinokur, and R. Fehrenbacher. ac absorption in the high-t_c superconductors: Reinterpretation of the irreversibility line. *Phys. Rev. B*, 43:3748–3751, Feb 1991.

[46] C V Topping and S J Blundell. A.c. susceptibility as a probe of low-frequency magnetic dynamics. *Journal of Physics: Condensed Matter*, 31(48):483002, 2019.

[47] Dawid Pinkowicz, Robert Podgajny, Robert Pełka, Wojciech Nitek, Maria Bałanda, Magdalena Makarewicz, Mariusz Czapla, Jan Żukrowski, Czesław Kapusta, Dariusz Zając, and Barbara Sieklucka. Iron(ii)-octacyanoniobate(iv) ferromagnet with tc 43 k. *Dalton Transactions*, 37:7549–7553, 2009.

[48] K Matsuhira, Y Hinatsu, and T Sakakibara. Novel dynamical magnetic properties in the spin ice compound dy2ti2o7. *Journal of Physics: Condensed Matter*, 13(31):L737, jul 2001.

[49] J. Snyder, B. G. Ueland, J. S. Slusky, H. Karunadasa, R. J. Cava, and P. Schiffer. Low-temperature spin freezing in the $dy_2ti_2o_7$ spin ice. *Phys. Rev. B*, 69:064414, Feb 2004.

[50] C. L. Degen, F. Reinhard, and P. Cappellaro. Quantum sensing. *Rev. Mod. Phys.*, 89:035002, Jul 2017.

[51] I. Lovchinsky, J. D. Sanchez-Yamagishi, E. K. Urbach, S. Choi, S. Fang, T. I. Andersen, K. Watanabe, T. Taniguchi, A. Bylinskii, E. Kaxiras, P. Kim, H. Park, and M. D. Lukin. Magnetic resonance spectroscopy of an atomically thin material using a single-spin qubit. *Science*, 355(6324):503–507, 2017.

[52] Brian B. Zhou, Paul C. Jerger, Kan-Heng Lee, Masaya Fukami, Fauzia Mujid, Jiwoong Park, and David D. Awschalom. Spatiotemporal mapping of a photocurrent vortex in monolayer mos_2 using diamond quantum sensors. *Phys. Rev. X*, 10:011003, Jan 2020.

[53] M W Doherty, J Michl, F Dolde, I Jakobi, P Neumann, N B Manson, and J Wrachtrup. Measuring the defect structure orientation of a single NV^- centre in diamond. *New Journal of Physics*, 16(6):063067, jun 2014.

[54] O. Bostanjoglo and W. Vieweger. Magnetische bereiche in chromtrihalogeniden. *physica status solidi (b)*, 39(2):471–475, 1970.

[55] Nabeel Aslam, Matthias Pfender, Philipp Neumann, Rolf Reuter, Andrea Zappe, Felipe Fávaro de Oliveira, Andrej Denisenko, Hitoshi Sumiya, Shinobu Onoda, Junichi Isoya, and Jörg Wrachtrup. Nanoscale nuclear magnetic resonance with chemical resolution. *Science*, 357(6346):67–71, 2017.

[56] David R. Glenn, Dominik B. Bucher, Junghyun Lee, Mikhail D. Lukin, Hongkun Park, and Ronald L. Walsworth. High-resolution magnetic resonance spectroscopy using a solid-state spin sensor. *Nature*, 555(7696):351–354, March 2018.

[57] Fazhan Shi, Qi Zhang, Pengfei Wang, Hongbin Sun, Jiarong Wang, Xing Rong, Ming Chen, Chenyong Ju, Friedemann Reinhard, Hongwei Chen, Jörg Wrachtrup, Junfeng Wang, and Jiangfeng Du. Single-protein spin resonance spectroscopy under ambient conditions. *Science*, 347(6226):1135–1138, 2015.

[58] Yu-Xuan Wang, Xin-Yue Zhang, Chunhua Li, Xiaohan Yao, Ruihuan Duan, Thomas K. M. Graham, Zheng Liu, Fazel Tafti, David Broido, Ying Ran, and Brian B. Zhou. Visualization of bulk and edge photocurrent flow in anisotropic weyl semimetals. *Nature Physics*, 19(4):507–514, Apr 2023.

[59] Kyle L. Seyler, Ding Zhong, Bevin Huang, Xiayu Linpeng, Nathan P. Wilson, Takashi Taniguchi, Kenji Watanabe, Wang Yao, Di Xiao, Michael A. McGuire, Kai-Mei C. Fu, and Xiaodong Xu. Valley manipulation by optically tuning the magnetic proximity effect in wse2/cri3 heterostructures. *Nano Letters*, 18(6):3823–3828, 2018. PMID: 29756784.

[60] Kenneth S. Burch, David Mandrus, and Je-Geun Park. Magnetism in two-dimensional van der waals materials. *Nature*, 563(7729):47–52, 2018.

[61] Cheng Gong and Xiang Zhang. Two-dimensional magnetic crystals and emergent heterostructure devices. *Science*, 363(6428):eaav4450, 2019.

[62] Kin Fai Mak, Jie Shan, and Daniel C. Ralph. Probing and controlling magnetic states in 2d layered magnetic materials. *Nature Reviews Physics*, 1(11):646–661, 2019.

[63] M. Buchner, K. Höfler, B. Henne, V. Ney, and A. Ney. Tutorial: Basic principles, limits of detection, and pitfalls of highly sensitive SQUID magnetometry for nanomagnetism and spintronics. *Journal of Applied Physics*, 124(16):161101, 10 2018.

[64] Kyle L. Seyler, Ding Zhong, Dahlia R. Klein, Shiyuan Gao, Xiaoou Zhang, Bevin Huang, Efrén Navarro-Moratalla, Li Yang, David H. Cobden, Michael A. McGuire, Wang Yao, Di Xiao, Pablo Jarillo-Herrero, and Xiaodong Xu. Ligand-field helical luminescence in a 2d ferromagnetic insulator. *Nature Physics*, 14(3):277–281, Mar 2018.

[65] Zhaowei Zhang, Jingzhi Shang, Chongyun Jiang, Abdullah Rasmita, Weibo Gao, and Ting Yu. Direct photoluminescence probing of ferromagnetism in monolayer two-dimensional crbr3. *Nano Letters*, 19(5):3138–3142, May 2019.

[66] Bevin Huang, Genevieve Clark, Efrén Navarro-Moratalla, Dahlia R. Klein, Ran Cheng, Kyle L. Seyler, Ding Zhong, Emma Schmidgall, Michael A. McGuire, David H. Cobden, Wang Yao, Di Xiao, Pablo Jarillo-Herrero, and Xiaodong Xu. Layer-dependent ferromagnetism in a van der waals crystal down to the monolayer limit. *Nature*, 546(7657):270–273, Jun 2017.

[67] Cheng Gong, Lin Li, Zhenglu Li, Huiwen Ji, Alex Stern, Yang Xia, Ting Cao, Wei Bao, Chenzhe Wang, Yuan Wang, Z. Q. Qiu, R. J. Cava, Steven G. Louie, Jing Xia, and Xiang Zhang. Discovery of intrinsic ferromagnetism in two-dimensional van der waals crystals. *Nature*, 546(7657):265–269, Jun 2017.

[68] Chenhao Jin, Zui Tao, Kaifei Kang, Kenji Watanabe, Takashi Taniguchi, Kin Fai Mak, and Jie Shan. Imaging and control of critical fluctuations in two-dimensional magnets. *Nature Materials*, 19(12):1290–1294, 2020.

[69] Xiao-Xiao Zhang, Lizhong Li, Daniel Weber, Joshua Goldberger, Kin Fai Mak, and Jie Shan. Gate-tunable spin waves in antiferromagnetic atomic bilayers. *Nature Materials*, 19(8):838–842, 2020.

[70] D. Ghazaryan, M. T. Greenaway, Z. Wang, V. H. Guarochico-Moreira, I. J. Vera-Marun, J. Yin, Y. Liao, S. V. Morozov, O. Kristanovski, A. I. Lichtenstein, M. I. Katsnelson, F. Withers, A. Mishchenko, L. Eaves, A. K. Geim, K. S. Novoselov, and A. Misra. Magnon-assisted tunnelling in van der waals heterostructures based on crbr3. *Nature Electronics*, 1(6):344–349, 2018.

[71] D. R. Klein, D. MacNeill, J. L. Lado, D. Soriano, E. Navarro-Moratalla, K. Watanabe, T. Taniguchi, S. Manni, P. Canfield, J. Fernández-Rossier, and P. Jarillo-Herrero. Probing magnetism in 2d van der waals crystalline insulators via electron tunneling. *Science*, 360(6394):1218–1222, 2018.

[72] Zhe Wang, Marco Gibertini, Dumitru Dumcenco, Takashi Taniguchi, Kenji Watanabe, Enrico Giannini, and Alberto F. Morpurgo. Determining the phase diagram of atomically thin layered antiferromagnet crcl3. *Nature Nanotechnology*, 14(12):1116–1122, Dec 2019.

[73] Meng Wu, Zhenglu Li, Ting Cao, and Steven G. Louie. Physical origin of giant excitonic and magneto-optical responses in two-dimensional ferromagnetic insulators. *Nature Communications*, 10(1):2371, May 2019.

[74] Tula R. Paudel and Evgeny Y. Tsymbal. Spin filtering in cri3 tunnel junctions. *ACS Applied Materials & Interfaces*, 11(17):15781–15787, 2019.

[75] Alejandro Molina-Sánchez, Gonçalo Catarina, Davide Sangalli, and Joaquín Fernández-Rossier. Magneto-optical response of chromium trihalide monolayers: chemical trends. *J. Mater. Chem. C*, 8:8856–8863, 2020.

[76] David A. Broadway, Sam C. Scholten, Cheng Tan, Nikolai Dontschuk, Scott E. Lillie, Brett C. Johnson, Guolin Zheng, Zhenhai Wang, Artem R. Oganov, Shangjie Tian, Chenghe Li, Hechang Lei, Lan Wang, Lloyd C. L. Hollenberg, and Jean-Philippe Tetienne. Imaging domain reversal in an ultrathin van der waals ferromagnet. *Advanced Materials*, 32(39):2003314, 2020.

[77] F. Fabre, A. Finco, A. Purbawati, A. Hadj-Azzem, N. Rougemaille, J. Coraux, I. Philip, and V. Jacques. Characterization of room-temperature in-plane magnetization in thin flakes of $Crte_2$ with a single-spin magnetometer. *Phys. Rev. Mater.*, 5:034008, Mar 2021.

[78] Maria Bałanda. Ac susceptibility studies of phase transitions and magnetic relaxation: Conventional, molecular and low-dimensional magnets. *Acta Physica Polonica A*, 124:964–976, 2013.

[79] M. Gibertini, M. Koperski, A. F. Morpurgo, and K. S. Novoselov. Magnetic 2d materials and heterostructures. *Nature Nanotechnology*, 14(5):408–419, 2019.

[80] S. Chikazumi. *Physics of Ferromagnetism*. Oxford University Press, Oxford, 2nd ed. edition, 1997.

[81] Stuart Parkin and See-Hun Yang. Memory on the racetrack. *Nature Nanotechnology*, 10(3):195–198, 2015.

[82] Saúl Vélez, Jakob Schaab, Martin S. Wörnle, Marvin Müller, Elzbieta Gradauskaite, Pol Welter, Cameron Gutgsell, Corneliu Nistor, Christian L. Degen, Morgan Trassin, Manfred Fiebig, and Pietro Gambardella. High-speed domain wall racetracks in a magnetic insulator. *Nature Communications*, 10(1):4750, 2019.

[83] J. Grollier, D. Querlioz, K. Y. Camsari, K. Everschor-Sitte, S. Fukami, and M. D. Stiles. Neuromorphic spintronics. *Nature Electronics*, 3(7):360–370, 2020.

[84] Weijiong Chen, Zeyuan Sun, Zhongjie Wang, Lehua Gu, Xiaodong Xu, Shiwei Wu, and Chunlei Gao. Direct observation of van der waals stacking–dependent interlayer magnetism. *Science*, 366(6468):983–987, 2019.

[85] Mykola Abramchuk, Samantha Jaszewski, Kenneth R. Metz, Gavin B. Osterhoudt, Yiping Wang, Kenneth S. Burch, and Fazel Tafti. Controlling magnetic and optical properties of the van der waals crystal crcl3−xbrx via mixed halide chemistry. *Advanced Materials*, 30(25):1801325, 2018.

[86] Thomas A. Tartaglia, Joseph N. Tang, Jose L. Lado, Faranak Bahrami, Mykola Abramchuk, Gregory T. McCandless, Meaghan C. Doyle, Kenneth S. Burch, Ying Ran, Julia Y. Chan, and Fazel Tafti. Accessing new magnetic regimes by tuning the ligand spin-orbit coupling in van der waals magnets. *Science Advances*, 6(30):eabb9379, 2020.

[87] Hyun Ho Kim, Bowen Yang, Siwen Li, Shengwei Jiang, Chenhao Jin, Zui Tao, George Nichols, Francois Sfigakis, Shazhou Zhong, Chenghe Li, Shangjie Tian, David G. Cory, Guo-Xing Miao, Jie Shan, Kin Fai Mak, Hechang Lei, Kai Sun, Liuyan Zhao, and Adam W. Tsen. Evolution of interlayer and intralayer magnetism in three atomically thin chromium trihalides. *Proceedings of the National Academy of Sciences*, 116(23):11131–11136, 2019.

[88] Jun-Shan Si, Hongxing Li, Bin-Guang He, Zi-Peng Cheng, and Wei-Bing Zhang. Revealing the underlying mechanisms of the stacking order and interlayer magnetism of bilayer crbr3. *The Journal of Physical Chemistry C*, 125(13):7314–7320, 2021.

[89] Francisco H. Salas and Manuel Mirabal-Garca. Quenching of the hopkinson maximum under contamination in the system gd(0001)/w(110). *Phys. Rev. B*, 41:10859–10861, May 1990.

[90] Sabyasachi Tiwari, Maarten L. Van de Put, Bart Sorée, and William G. Vandenberghe. Critical behavior of the ferromagnets cri_3, $crbr_3$, and $crgete_3$ and the antiferromagnet $fecl_2$: A detailed first-principles study. *Phys. Rev. B*, 103:014432, Jan 2021.

[91] Dina Abdul Wahab, Mathias Augustin, Samuel Manas Valero, Wenjun Kuang, Sarah Jenkins, Eugenio Coronado, Irina V. Grigorieva, Ivan J. Vera-Marun, Efrén Navarro-Moratalla, Richard F. L. Evans, Kostya S. Novoselov, and Elton J. G. Santos. Quantum rescaling, domain metastability, and hybrid domain-walls in 2d cri3 magnets. *Advanced Materials*, 33(5):2004138, 2021.

[92] Yu Liu and C. Petrovic. Anisotropic magnetocaloric effect in single crystals of cri_3. *Phys. Rev. B*, 97:174418, May 2018.

[93] John T. Ho and J. D. Litster. Divergences of the Magnetic Properties of CrBr3 near the Critical Point. *Journal of Applied Physics*, 40(3):1270–1271, 03 1969.

[94] G. T. Rado, R. W. Wright, and W. H. Emerson. Ferromagnetism at very high frequencies. iii. two mechanisms of dispersion in a ferrite. *Phys. Rev.*, 80:273–280, Oct 1950.

[95] M. Guyot and V. Cagan. Temperature dependence of the domain wall mobility in yig, deduced from the frequency spectra of the initial susceptibility of polycrystals. *Journal of Magnetism and Magnetic Materials*, 27(2):202–208, 1982.

[96] E. Jedryka, R. J. Yeh, M. Ramesh, P. E. Wigen, and A. Pajaczkowska. Temperature dependence of domain wall resonance in CrBr3. *Journal of Applied Physics*, 53(11):8357–8359, 11 1982.

[97] G. Infante, R. Varga, G. A. Badini-Confalonieri, and M. Vázquez. Locally induced domain wall damping in a thin magnetic wire. *Applied Physics Letters*, 95(1):012503, 07 2009.

[98] Xiaoxiang Xi, Zefang Wang, Weiwei Zhao, Ju-Hyun Park, Kam Tuen Law, Helmuth Berger, László Forró, Jie Shan, and Kin Fai Mak. Ising pairing in superconducting nbse2 atomic layers. *Nature Physics*, 12(2):139–143, February 2016.

[99] Changsong Xu, Junsheng Feng, Mitsuaki Kawamura, Youhei Yamaji, Yousra Nahas, Sergei Prokhorenko, Yang Qi, Hongjun Xiang, and L. Bellaiche. Possible kitaev quantum spin liquid state in 2d materials with $s = 3/2$. *Phys. Rev. Lett.*, 124:087205, Feb 2020.

[100] Yilv Guo, Shijun Yuan, Bing Wang, Li Shi, and Jinlan Wang. Half-metallicity and enhanced ferromagnetism in li-adsorbed ultrathin chromium triiodide. *J. Mater. Chem. C*, 6:5716–5720, 2018.

[101] M. M. van de Loosdrecht, S. Draack, S. Waanders, J. G. L. Schlief, H. J. G. Krooshoop, T. Viereck, F. Ludwig, and B. ten Haken. A novel characterization technique for superparamagnetic iron oxide nanoparticles: The superparamagnetic quantifier, compared with magnetic particle spectroscopy. *Review of Scientific Instruments*, 90(2):024101, 02 2019.

[102] Xingzhi Wang, Jun Cao, Zhengguang Lu, Arielle Cohen, Hikari Kitadai, Tianshu Li, Qishuo Tan, Matthew Wilson, Chun Hung Lui, Dmitry Smirnov, Sahar Sharifzadeh, and Xi Ling. Spin-induced linear polarization of photoluminescence in antiferromagnetic van der waals crystals. *Nature Materials*, 20(7):964–970, Jul 2021.

[103] Nathan P. Wilson, Kihong Lee, John Cenker, Kaichen Xie, Avalon H. Dismukes, Evan J. Telford, Jordan Fonseca, Shivesh Sivakumar, Cory Dean, Ting Cao, Xavier Roy, Xiaodong Xu, and Xiaoyang Zhu. Interlayer electronic coupling on demand in a 2d magnetic semiconductor. *Nature Materials*, 20(12):1657–1662, Dec 2021.

[104] Kai Hao, Robert Shreiner, Andrew Kindseth, and Alexander A. High. Optically controllable magnetism in atomically thin semiconductors. *Science Advances*, 8(39):eabq7650, 2022.

[105] Junho Choi, Christopher Lane, Jian-Xin Zhu, and Scott A. Crooker. Asymmetric magnetic proximity interactions in mose2/crbr3 van der waals heterostructures. *Nature Materials*, 22(3):305–310, Mar 2023.

[106] Xi Wang, Chengxin Xiao, Heonjoon Park, Jiayi Zhu, Chong Wang, Takashi Taniguchi, Kenji Watanabe, Jiaqiang Yan, Di Xiao, Daniel R. Gamelin, Wang Yao, and Xiaodong Xu. Light-induced ferromagnetism in moiré superlattices. *Nature*, 604(7906):468–473, Apr 2022.

[107] Valery Ortiz Jimenez, Yen Thi Hai Pham, Mingzu Liu, Fu Zhang, Zhuohang Yu, Vijaysankar Kalappattil, Baleeswaraiah Muchharla, Tatiana Eggers, Dinh Loc Duong, Mauricio Terrones, and Manh-Huong Phan. Light-controlled room temperature ferromagnetism in vanadium-doped tungsten disulfide semiconducting monolayers. *Advanced Electronic Materials*, 7(8):2100030, 2021.

[108] Peiyao Zhang, Ting-Fung Chung, Quanwei Li, Siqi Wang, Qingjun Wang, Warren L. B. Huey, Sui Yang, Joshua E. Goldberger, Jie Yao, and Xiang Zhang. All-optical switching of magnetization in atomically thin cri3. *Nature Materials*, 21(12):1373–1378, Dec 2022.

[109] Naonobu Shimamoto, Shin-ichi Ohkoshi, Osamu Sato, and Kazuhito Hashimoto. Control of charge-transfer-induced spin transition temperature on cobalt−iron prussian blue analogues. *Inorganic Chemistry*, 41(4):678–684, Feb 2002.

[110] Valerio Pinchetti, Qiumei Di, Monica Lorenzon, Andrea Camellini, Mauro Fasoli, Margherita Zavelani-Rossi, Francesco Meinardi, Jiatao Zhang, Scott A. Crooker, and

Sergio Brovelli. Excitonic pathway to photoinduced magnetism in colloidal nanocrystals with nonmagnetic dopants. *Nature Nanotechnology*, 13(2):145–151, Feb 2018.

[111] R. V. Mikhaylovskiy, T. J. Huisman, V. A. Gavrichkov, S. I. Polukeev, S. G. Ovchinnikov, D. Afanasiev, R. V. Pisarev, Th. Rasing, and A. V. Kimel. Resonant pumping of $d-d$ crystal field electronic transitions as a mechanism of ultrafast optical control of the exchange interactions in iron oxides. *Phys. Rev. Lett.*, 125:157201, Oct 2020.

[112] A. Ron, S. Chaudhary, G. Zhang, H. Ning, E. Zoghlin, S. D. Wilson, R. D. Averitt, G. Refael, and D. Hsieh. Ultrafast enhancement of ferromagnetic spin exchange induced by ligand-to-metal charge transfer. *Phys. Rev. Lett.*, 125:197203, Nov 2020.

[113] Alexey Chernikov, Timothy C. Berkelbach, Heather M. Hill, Albert Rigosi, Yilei Li, Burak Aslan, David R. Reichman, Mark S. Hybertsen, and Tony F. Heinz. Exciton binding energy and nonhydrogenic rydberg series in monolayer ws_2. *Phys. Rev. Lett.*, 113:076802, Aug 2014.

[114] Gang Wang, Alexey Chernikov, Mikhail M. Glazov, Tony F. Heinz, Xavier Marie, Thierry Amand, and Bernhard Urbaszek. Colloquium: Excitons in atomically thin transition metal dichalcogenides. *Rev. Mod. Phys.*, 90:021001, Apr 2018.

[115] Meng Wu, Zhenglu Li, and Steven G. Louie. Optical and magneto-optical properties of ferromagnetic monolayer $crbr_3$: A first-principles *gw* and *gw* plus bethe-salpeter equation study. *Phys. Rev. Mater.*, 6:014008, Jan 2022.

[116] Linghan Zhu and Li Yang. Quasiparticle energies and excitonic effects of chromium trichloride: From two dimensions to bulk. *Phys. Rev. B*, 101:245401, Jun 2020.

[117] Swagata Acharya, Dimitar Pashov, Alexander N. Rudenko, Malte Rösner, Mark van Schilfgaarde, and Mikhail I. Katsnelson. Real- and momentum-space description of the excitons in bulk and monolayer chromium tri-halides. *npj 2D Materials and Applications*, 6(1):33, May 2022.

[118] Chia-Hsin Chen and Hsin-Fei Meng. Defect auger exciton dissociation and impact ionization in conjugated polymers. *Phys. Rev. B*, 64:125202, Sep 2001.

[119] Haining Wang, Jared H. Strait, Changjian Zhang, Weimin Chan, Christina Manolatou, Sandip Tiwari, and Farhan Rana. Fast exciton annihilation by capture of electrons or holes by defects via auger scattering in monolayer metal dichalcogenides. *Phys. Rev. B*, 91:165411, Apr 2015.

[120] Yinghe Zhao, Lingfang Lin, Qionghua Zhou, Yunhai Li, Shijun Yuan, Qian Chen, Shuai Dong, and Jinlan Wang. Surface vacancy-induced switchable electric polarization and enhanced ferromagnetism in monolayer metal trihalides. *Nano Letters*, 18(5):2943–2949, May 2018.

[121] M. Luo, Y.D. Li, K.J. Wang, and Y.H. Shen. Adsorption induced magnetic anisotropy in the two-dimensional magnet crcl3. *Solid State Communications*, 321:114048, 2020.

[122] Michael A. McGuire, Genevieve Clark, Santosh KC, W. Michael Chance, Gerald E. Jellison, Valentino R. Cooper, Xiaodong Xu, and Brian C. Sales. Magnetic behavior and spin-lattice coupling in cleavable van der waals layered crcl$_3$ crystals. *Phys. Rev. Mater.*, 1:014001, Jun 2017.

[123] Dahlia R. Klein, David MacNeill, Qian Song, Daniel T. Larson, Shiang Fang, Mingyu Xu, R. A. Ribeiro, P. C. Canfield, Efthimios Kaxiras, Riccardo Comin, and Pablo Jarillo-Herrero. Enhancement of interlayer exchange in an ultrathin two-dimensional magnet. *Nature Physics*, 15(12):1255–1260, Dec 2019.

[124] Xinghan Cai, Tiancheng Song, Nathan P. Wilson, Genevieve Clark, Minhao He, Xiaoou Zhang, Takashi Taniguchi, Kenji Watanabe, Wang Yao, Di Xiao, Michael A. McGuire, David H. Cobden, and Xiaodong Xu. Atomically thin crcl3: An in-plane layered antiferromagnetic insulator. *Nano Letters*, 19(6):3993–3998, 2019. PMID: 31083954.

[125] Amilcar Bedoya-Pinto, Jing-Rong Ji, Avanindra K. Pandeya, Pierluigi Gargiani, Manuel Valvidares, Paolo Sessi, James M. Taylor, Florin Radu, Kai Chang, and Stuart S. P. Parkin. Intrinsic 2d-xy ferromagnetism in a van der waals monolayer. *Science*, 374(6567):616–620, 2021.

[126] Victor M. Bermudez and Donald S. McClure. Spectroscopic studies of the two-dimensional magnetic insulators chromium trichloride and chromium tribromide-I. *Journal of Physics and Chemistry of Solids*, 40(2):129–147, 1979.

[127] Brian B. Zhou, Paul C. Jerger, Kan-Heng Lee, Masaya Fukami, Fauzia Mujid, Jiwoong Park, and David D. Awschalom. Spatiotemporal mapping of a photocurrent vortex in monolayer mos$_2$ using diamond quantum sensors. *Phys. Rev. X*, 10:011003, Jan 2020.

[128] Andrew McAllister, Dylan Bayerl, and Emmanouil Kioupakis. Radiative and Auger recombination processes in indium nitride. *Applied Physics Letters*, 112(25):251108, 06 2018.

[129] Dario Mastrippolito, Luca Ottaviano, Jing Wang, Jinjin Yang, Faming Gao, Mushtaq Ali, Gianluca D'Olimpio, Antonio Politano, Stefano Palleschi, Shafaq Kazim, Roberto Gunnella, Andrea Di Cicco, Anna Sgarlata, Judyta Strychalska-Nowak, Tomasz Klimczuk, Robert Joseph Cava, Luca Lozzi, and Gianni Profeta. Emerging oxidized and defective phases in low-dimensional crcl3. *Nanoscale Adv.*, 3:4756–4766, 2021.

[130] Dario Mastrippolito, Jing Wang, Gianni Profeta, and Luca Ottaviano. Unconventional ferrimagnetism and enhanced magnetic ordering temperature in monolayer $CrCl_3$ by introducing O impurities and Cl vacancies. *Journal of Physics: Materials*, 5(1):014004, 2022.

[131] Suhyeon Kim, Sangho Yoon, Hyobin Ahn, Gangtae Jin, Hyesun Kim, Moon-Ho Jo, Changgu Lee, Jonghwan Kim, and Sunmin Ryu. Photoluminescence path bifurcations by spin flip in two-dimensional crps4. *ACS Nano*, 16(10):16385–16393, Oct 2022.

[132] Magdalena Birowska, Paulo E. Faria Junior, Jaroslav Fabian, and Jens Kunstmann. Large exciton binding energies in $mnps_3$ as a case study of a van der waals layered magnet. *Phys. Rev. B*, 103:L121108, Mar 2021.

[133] Shichen Fu, Kyungnam Kang, Kamran Shayan, Anthony Yoshimura, Siamak Dadras, Xiaotian Wang, Lihua Zhang, Siwei Chen, Na Liu, Apoorv Jindal, Xiangzhi Li, Abhay N. Pasupathy, A. Nick Vamivakas, Vincent Meunier, Stefan Strauf, and Eui-Hyeok Yang. Enabling room temperature ferromagnetism in monolayer mos2 via in situ iron-doping. *Nature Communications*, 11(1):2034, Apr 2020.

[134] S Kazim, M Alì, S Palleschi, G D'Olimpio, D Mastrippolito, A Politano, R Gunnella, A Di Cicco, M Renzelli, G Moccia, O A Cacioppo, R Alfonsetti, J Strychalska-Nowak, T Klimczuk, R J Cava, and L Ottaviano. Mechanical exfoliation and layer number identification of single crystal monoclinic CrCl 3. *Nanotechnology*, 31(39):395706, sep 2020.

[135] D. A. Broadway, S. E. Lillie, S. C. Scholten, D. Rohner, N. Dontschuk, P. Maletinsky, J. P. Tetienne, and L. C.L. Hollenberg. Improved current density and magnetization reconstruction through vector magnetic field measurements. *Physical Review Applied*, 14(2):024076, 2020.

[136] Nicolas Morell, Slaven Tepsic, Antoine Reserbat-Plantey, Andrea Cepellotti, Marco Manca, Itai Epstein, Andreas Isacsson, Xavier Marie, Francesco Mauri, and Adrian Bachtold. Optomechanical Measurement of Thermal Transport in Two-Dimensional MoSe 2 Lattices. *Nano Letters*, 19(5):3143–3150, may 2019.

[137] Robin J. Dolleman, Samer Houri, Dejan Davidovikj, Santiago J. Cartamil-Bueno, Yaroslav M. Blanter, Herre S. J. van der Zant, and Peter G. Steeneken. Optomechanics for thermal characterization of suspended graphene. *Physical Review B*, 96(16):165421, oct 2017.

[138] Wilford N. Hansen and Maurice Griffel. Heat Capacities of CrF3 and CrCl3 from 15 to 300°K. *The Journal of Chemical Physics*, 28(5):902–907, may 1958.

[139] A. S. Dworkin, D. J. Sasmor, and E. R. Van Artsdalen. The Thermodynamics of Boron Nitride; Low-Temperature Heat Capacity and Entropy; Heats of Combustion and Formation. *The Journal of Chemical Physics*, 22(5):837–842, may 1954.

[140] Christopher A. Pocs, Ian A. Leahy, Hao Zheng, Gang Cao, Eun-Sang Choi, S.-H. Do, Kwang-Yong Choi, B. Normand, and Minhyea Lee. Giant thermal magnetoconductivity in CrCl3 and a general model for spin-phonon scattering. *Physical Review Research*, 2(1):013059, jan 2020.

[141] Insun Jo, Michael Thompson Pettes, Jaehyun Kim, Kenji Watanabe, Takashi Taniguchi, Zhen Yao, and Li Shi. Thermal Conductivity and Phonon Transport in Suspended Few-Layer Hexagonal Boron Nitride. *Nano Letters*, 13(2):550–554, feb 2013.

[142] Zhun-Yong Ong, Yongqing Cai, and Gang Zhang. Theory of substrate-directed heat dissipation for single-layer graphene and other two-dimensional crystals. *Physical Review B*, 94(16):165427, oct 2016.

[143] A. Zunger, A. Katzir, and A. Halperin. Optical properties of hexagonal boron nitride. *Physical Review B*, 13(12):5560–5573, jun 1976.

[144] John P. Perdew, Kieron Burke, and Matthias Ernzerhof. Generalized gradient approximation made simple. *Phys. Rev. Lett.*, 77:3865–3868, Oct 1996.

[145] Stefan Grimme, Jens Antony, Stephan Ehrlich, and Helge Krieg. A consistent and accurate ab initio parametrization of density functional dispersion correction (DFT-D) for the 94 elements H-Pu. *The Journal of Chemical Physics*, 132(15):154104, 04 2010.

[146] G. Kresse and D. Joubert. From ultrasoft pseudopotentials to the projector augmented-wave method. *Physical Review B*, 59(3):1758–1775, jan 1999.

[147] Y. Yekta, H. Hadipour, E. Şaşıoğlu, C. Friedrich, S. A. Jafari, S. Blügel, and I. Mertig. Strength of effective Coulomb interaction in two-dimensional transition-metal halides MX2 and MX3 (M = Ti, V, Cr, Mn, Fe, Co, Ni; X = Cl, Br, I). *Physical Review Materials*, 5(3):034001, mar 2021.

[148] S. L. Dudarev, G. A. Botton, S. Y. Savrasov, C. J. Humphreys, and A. P. Sutton. Electron-energy-loss spectra and the structural stability of nickel oxide: An LSDA+U study. *Physical Review B*, 57(3):1505–1509, jan 1998.

[149] Xin-Yue Zhang, Yu-Xuan Wang, Thomas A. Tartaglia, Thomas Ding, Mason J. Gray, Kenneth S. Burch, Fazel Tafti, and Brian B. Zhou. ac susceptometry of 2d van der waals magnets enabled by the coherent control of quantum sensors. *PRX Quantum*, 2:030352, Sep 2021.